SURFACE FUNCTIONALIZATION OF 1-D AND 2-D CARBON-BASED NANOMATERIALS AND THEIR APPLICATIONS

A Dissertation

by

HAIQING YAO

Submitted to the Office of Graduate and Professional Studies of
Texas A&M University
in partial fulfillment of the requirements for the degree of

DOCTOR OF PHILOSOPHY

Chair of Committee,	Hung-Jue Sue
Committee Members,	Janet Bluemel
	James Batteas
	Terry Creasy
Head of Department,	Ibrahim Karaman

May 2015

Major Subject: Materials Science and Engineering

ABSTRACT

Carbon nanotubes (CNTs) and graphene are dominant and emerging carbon-based materials that have attracted extensive attention for potential applications in advanced nanotechnology. The attractiveness of these materials originates from their excellent mechanical, thermal, and electrical properties. However, their insolubility and difficult processability in solvents have significantly limited their use. To solve these problems, surface functionalization is used to increase their solubility, enhance their processability in solvents, and integrate these materials into nanodevices. Conventional methods are being challenged due to their ineffective and insufficient control of the functionalization of CNTs or graphene, which is critical to realize tailored structures with unprecedented optical, electrical and catalytic properties. Further development in this field requires a fundamental understanding of the steps involved in surface functionalization, namely the reaction mechanism(s) and controlled kinetics, to yield tailored structures.

The overall objective of my dissertation is to develop new approaches to functionalizing CNTs and graphene, study the functionalization mechanism and kinetics, and fabricate tailored structures with unprecedented properties. The study begins with developing new covalent functionalization methods for CNTs and graphene based on the defect chemistry method. This method is less destructive and more reactive compared to the conjugate structure method. Amination of MWCNTs with octadecylamine on the mutual position of pyracyclene units in the closed caps and pentagons on the MWCNT

sidewalls is developed. The functionalized MWCNTs possess controllable surface wettability. For covalent functionalization of GO, dual-function silane agents were reacted with GO through oxygen containing groups. The exposed amine groups of the functionalized GO could effectively template the assembly of Au nanoparticles on the graphene surface with high density and good dispersity. The GO-Au composites exhibit improved surface-enhanced Raman scattering and enhanced efficiency in catalytic applications. For the noncovalent method, ZnO-CNT and ZnO-GO composites were prepared. Due to the electronegative nature of CNTs and GO, ZnO nanoparticles with positive charges can anchor on their surfaces through electrostatic attraction. The creative combination of CNTs or graphene and ZnO leads to higher efficiency and stability for photocatalytic applications than the corresponding components, which makes them a new class of functional materials to advance nanotechnology.

DEDICATION

To my husband and parents

ACKNOWLEDGEMENTS

I would never have been able to finish my dissertation without the guidance of my committee members, help from friends, and support from my family.

I would like to express my deepest gratitude to my advisor, Dr. Hung-Jue Sue, for his excellent guidance, caring, patience, and providing me with an excellent atmosphere for doing research. Special thanks go to my committee members, Dr. Bluemel, Dr. Batteas, and Dr. Creasy for their guidance and support throughout the course of this research.

I truly appreciate my current and previous colleagues, Dr. Chien-Chia Chu, Dr. Lin Jin, Dr. Xi Zhang, Spencer Hawkins and other workers for the precious discussion and the friendship. MCF and MIC staff also provided generous assistance in my research.

I would also like to thank my parents, my brother and sister in-law. They were always supporting me and encouraging me with their best wishes. I would like to thank my husband, Liangfa Hu. He was always there cheering me up and stood by me through the good and bad times. I really appreciate his help on my research and my personal life.

Finally, I also want to extend my gratitude to the financial support from Kaneka. My research would not have been possible without its support.

TABLE OF CONTENTS

Page

LIST OF FIGURES

Page

LIST OF TABLES

Page

CHAPTER I

INTRODUCTION

1.1 Overview

Carbon-based nanomaterials have attracted broad interest in the materials science community for decades.[1] Carbon is an extremely light and versatile material and has hugely varying properties depending on the local bonding of the constituting carbon atoms. Well-known examples of carbon allotropes are diamond, amorphous carbon, fullerenes, carbon nanotubes (CNTs), and graphene. Among them, CNTs and graphene, as one dimensional (1D) and two dimensional (2D) nanomaterials (**Figure 1**), possess excellent mechanical strength, electrical and thermal conductivity, and optical properties.[2, 3] Lots of research efforts have been focused on utilizing these advantageous properties for various applications, such as high-strength composite materials and electronics.[4, 5]

As 1D nanomaterial, the structure of CNTs can be conceptualized by wrapping a one-atom-thick layer of graphene into a seamless cylinder. Topologically, carbon nanotubes (CNTs) can be constructed by rolling up a single layer of graphene along a certain direction into a tiny cylinder with a possible diameter from subnanometer to a few nanometers (**Figure 1**). Due to their special structure, CNTs possess a combination of unprecedented properties: a) high electrical conductivity, b) chemical and thermal stability, c) extremely high tensile strength and elasticity, and d) the potential of surface functionalization with various compounds. Because of these extraordinary properties,

CNTs can be considered as attractive candidates in diverse nanotechnological applications, such as fillers in polymer matrixes, batteries, chemical sensors, and many others nanodevices.

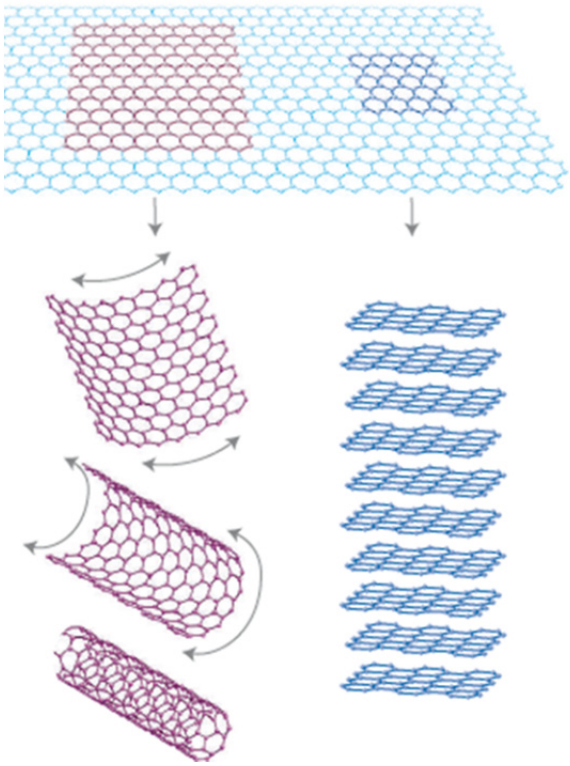

Figure 1. Schematic illustration of carbon nanotube and graphite formation from graphene.[6]

Graphene is the name given to a flat monolayer of carbon atoms tightly packed into a 2D honeycomb lattice and is also predicted to have a range of unusual properties.[6] It is the newest nanomaterial to burst onto the scene. Graphene possesses similar electrical, thermal, and mechanical properties as CNTs, but the 2-D atomic sheet of graphene enables more diverse electronic characteristics; the existence of massless Dirac fermions and quantum Hall effect help explain the low-energy charge excitation at room

temperature and the optical transparency in infrared and visible range of the spectrum.[6] In addition, graphene is structurally robust yet highly flexible, which makes it attractive for engineering flexible thin films.[7]

Although CNTs and graphene are two promising materials for various applications, they both have limitations during processing. The difficulties in manipulation and lack of solubility in solvents decrease the overall yield of usable material and interfere with most of the desired properties of the CNTs or graphene. For CNTs, procedures for the synthesis of nanotubes invariably deliver bundles and entanglements, which are composed of up to hundreds of single nanotubes. Another challenge about CNT application is their insolubility in all solvents due to their inert surface properties.[8] Like carbon nanotubes, the difficulties in manipulation and the lack of solubility in solvents also have been a major obstacle to exploiting graphene in most proposed applications. Graphene sheets with a high specific surface area, unless well separated from each other, tend to restack to form graphite through van der Waals interactions. The lack of an efficient approach to producing processable single graphene sheets in large quantities limits their further applications.

To overcome these challenges and make CNTs and graphene more processable for proposed applications, the solution-based route involving their surface functionalization becomes attractive. Addition of chemical groups to the CNT or graphene surface disrupts their agglomerates, and it also becomes easier to disperse them in solvents.[8, 9] Moreover, CNT or graphene can interact with different classes of compounds. The formation of composites allows a better processing of CNT or graphene

toward the fabrication of innovative nanodevices. Many recent research efforts have been geared toward incorporating CNTs or graphene into various materials to utilize their multifunctional nature (i.e., electrical and thermal conductivity and optical properties) rather than focusing solely on pure components. The surface functionalization of CNTs and graphene can be approached via two methods: (a) covalent attachment of various groups through chemical reactions, and (b) noncovalent functionalization of various functional molecules on the surface of these materials.

Conventional methods have been challenged to control the functionalization of CNTs or graphene, which is critical to realize composites with tailored structures and unprecedented optical, electrical and catalytic properties. Further development in this field requires fundamental understanding of the steps involved in the surface functionalization, namely 1) reaction mechanism, and 2) controlled kinetics to yield tailored structures. The overall objective of my dissertation is to develop new approaches to functionalize CNTs and graphene, study the functionalization mechanism and kinetics, and realize tailored structures and unprecedented properties in composites. This dissertation covers the synergistic character of the nanotube (graphene)–molecule interactions, as molecules that affect nanotube properties are also altered in the presence of the nanotube (graphene). The diversity of reaction mechanisms, the range of experimental techniques employed for their characterization, and the applications for functionalized CNTs or graphene are all discussed in this dissertation.

1.2 Organization of the dissertation

A comprehensive literature review on the recent progress of surface functionalization of CNTs and graphene will be given as Chapter II. Detailed information regarding two main methods, covalent and noncovalent functionalization, is described in this chapter. It also provides a brief review of the potential applications of functionalized CNTs and graphene.

Based on Chapter II, Chapters III–V develop new covalent functionalization methods on CNTs and graphene, based on the defect chemistry method. The defect chemistry method is less destructive and more reactive, compared with the conjugate structure method. Defects are therefore a promising starting point for the development of the covalent chemistry. Chapter III develops the site specificity of reaction on the mutual position of pyracyclene units in the closed caps and pentagons on the MWCNT sidewalls. The functionalized MWCNTs possess controllable surface wettability and high electrical conductivity. A facile way to fabricate functionalized and reduced graphene oxide (RGO) is covered by Chapter IV and V. Various silane molecules react with the hydroxyl groups of GO and subsequently cross-link on the graphene surface. These different functional groups enable controlling the grafting density of Au NPs. Their applications on surface-enhanced Raman Scattering and catalytic applications are also described in this chapter.

Chapters VI and VII select the noncovalent functionalization method for CNTs and GO. For the noncovalent method, the second component is physically absorbed on CNTs or graphene surface via van der Waals forces, π-π interactions, or electrostatic

interaction. Due to the electronegative nature of CNTs and GO, ZnO nanoparticles with positive charges are selected to anchor on the surface of these two materials through electrostatic interaction. This method overcomes the traditional challenge to prepare well-integrated ZnO-carbon composites.

Lastly, the concluding remarks to summarize the findings of this dissertation and the future research plans are drawn in Chapter VIII.

CHAPTER II

LITERATURE REVIEW

CNTs were firstly discovered by Sumio Iijima during the synthesis of fullerene in 1991.[10] CNTs with a diameter from 4 to 30 nm and a length of 1μm were grown on the negative end of the carbon electrode used in the D.C. arc-discharge evaporation of carbon. Until now, various methods have been developed to synthesize CNTs, like laser ablation, high-pressure carbon monoxide disproportionation, and chemical vapor deposition (CVD).[11] Single-walled carbon nanotubes (SWCNTs) can be constructed by rolling up a single layer of graphene along a certain direction into a tiny cylinder. The rolling-up direction and the chirality of SWCNTs determine their fundamental properties. The way the graphene sheet is wrapped is represented by a pair of indices (n, m).[10, 12] The integers n and m denote the number of unit vectors along two directions in the honeycomb crystal lattice of graphene. If m = 0, the nanotubes are called zigzag nanotubes, and if n = m, the nanotubes are called armchair nanotubes. Otherwise, they are called chiral. Depending on (n, m), their electrical conductivity can show metallic or semiconducting behavior.

Multi-walled carbon nanotubes (MWCNTs) consist of multiple rolled layers (concentric tubes) of graphene. The interlayer distance in multi-walled nanotubes is close to the distance between graphene layers in graphite, approximately 3.4 Å.[11] Its individual shells can be described as single walled-carbon nanotubes, which can be metallic or semiconducting. Because of statistical probability and restrictions on the

relative diameters of the individual tubes, the whole MWCNT is usually a zero-gap metal.[1, 10] The cylindrical carbon structure renders CNTs a wide range of electrical and optical properties stemming not only from their extended sp^2 carbon but also from their tunable physical properties (e.g., diameter, length, surface functionalization, and chirality).[13]

Due to their diverse array of useful properties, CNTs have become the most widely used carbon-based nanomaterials. For all the applications of CNTs, it is advantageous to have individually dispersed nanotubes instead of bundles to achieve their function.[14] However, procedures for the synthesis of nanotubes invariably deliver bundles and entanglements, which are composed of up to hundreds of single nanotubes. It is van der Waals attraction between tubes that tightly holds tubes together, leads them into bundles, and makes them difficult to manipulate for further applications. Another challenge about CNT application is their insolubility in all solvents due to their inert surface properties.[8] The difficulties in manipulation and lack of solubility in solvents decrease the overall yield of usable material and interfere with most of the desired properties of the CNTs. For example, CNTs have been utilized as reinforcing nanofillers for polymer nanocomposites due to their superb mechanical properties. However, the possibility of CNT incorporated polymer nanocomposites has not met with satisfactory results, mostly due to their limited dispersion in the polymer and poor interaction with the surrounding matrices. These factors lead to inefficient load transfer from the matrices to the CNTs.[15]

Graphene is a new nanomaterial that bursts into the scene since the year of 2004 through the ground-breaking work by Geim and Novoselov to extract graphene from graphite via mechanical cleavage of graphite.[6, 16] As one-atom-thick and two-dimensional layers of sp^2-bonded carbon, graphene sheets are predicted to have a range of unusual properties. Their thermal conductivity and mechanical stiffness are comparable with CNTs; and recent studies have shown that individual graphene sheets have extraordinary electronic transport properties.[17] One possible route to harnessing these properties for applications would be to incorporate graphene sheets in a composite material.[18] The manufacturing of such composites requires the prevention of aggregation for graphene sheets because most of their unique properties are only associated with individual sheets.

Graphite, consisting of a stack of flat graphene sheets, is the most readily available and least expensive source for the production of a large quantity of graphene sheets. Mechanical cleavage of graphite originally led to the discovery of graphene sheets[16] and is the process currently used in most experimental studies of graphene. However, the low productivity of this method makes it unsuitable for large-scale use. Nevertheless, chemical exfoliation of graphite, as a wet chemistry method, is not only scalable to offer large-scale and direct exfoliation of graphene, but also versatile and easy to obtain various derivatives of graphene.[19] This approach usually involves oxidation of graphite powder into graphene oxide (GO) in the presence of strong oxidants and acids. Various methods have been developed to prepare GO.[20] Among them, Hummers' method is one of the most popular ones, which uses a combination of

potassium permanganate and sulfuric acid.[21] These reaction methods achieve similar levels of oxidation (carbon-to-oxygen atomic ratios of approximately 2:1), which disrupts the delocalized electronic structure of graphite and introduces a variety of oxygen-based chemical functionalities on the graphene surface. Because of the complex graphite structure and the unclear reaction mechanisms, the precise chemical structure of GO has been the subject of considerable debate over the years, and even to this day no unambiguous model exists.[20]

The most well-known model is reported by Lerf and Klinowski (**Figure 2**).[22] The detailed structure is: the "oxidized" benzene rings contain epoxide and hydroxide groups, and these groups are very close to one another. These functional groups in every oxidized aromatic ring are distributed randomly. The GO sheets terminate with hydroxide and carboxylic groups. The as-produced GO has been a promising alternative for graphene. However, one drawback of GO is that the sp^2 bonding networks of graphene have been severely damaged during the oxidation process. After the oxidation process, GO has become electrically insulating, and its thermal and mechanical properties are also compromised. Because electrical conductivity can be recovered by restoring the π-π network, one of the most important reactions of GO is its reduction. Unfortunately, previous work has shown that reduced GO precipitates as irreversible agglomerates and becomes insoluble in water owing to their hydrophobic nature, making further processing difficult.

To overcome these challenges and make CNTs and graphene more processable for proposed applications, many approaches have been developed to functionalize their

surface. Many of these aims are to introduce new functional groups, change their surface properties, increase their solubility in solvent and achieve potential applications. In the following sections, a comprehensive review of the surface functionalization methods will be discussed. Two different functionalization methods will be covered in this chapter: (a) covalent functionalization and (b) noncovalent functionalization.

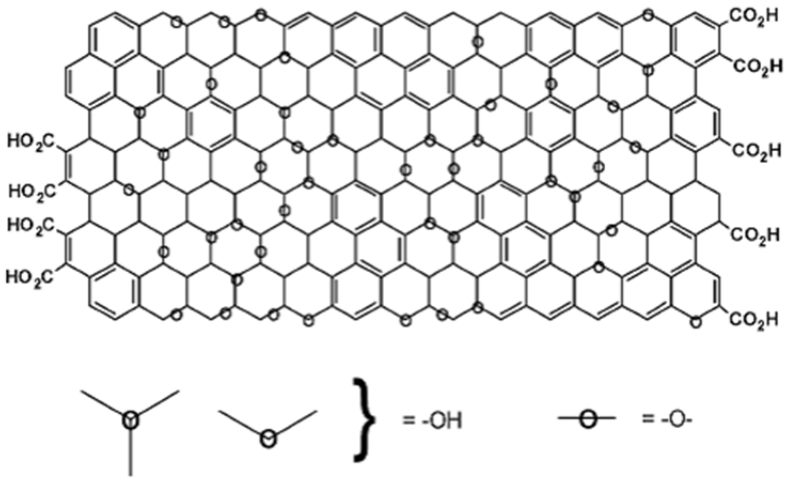

Figure 2. Chemical structure of GO.[22]

2.1 Covalent functionalization

The covalent functionalization of CNTs or graphene allows for functional groups being chemically attached to their surface. There are two distinct regions with differing reactivity towards covalent chemical modifications: graphitic structure chemistry and defect site chemistry.[14] For CNTs, the presence of five-membered rings at the caps (**Figure 3**) leads to a relatively high reactivity. By comparison, functionalization of the sidewall comprising of the regular π-π conjugate structure is more difficult to

accomplish. A similar situation happens for GO. GO sheets have chemically reactive oxygen functionalities, such as carboxylic acid groups, epoxide and hydroxyl groups (**Figure 2**).[23] Defects in this manner are therefore a promising starting point for the development of the covalent chemistry of GO. A distinct feature of adding chemical functionalities can be dramatic, permanent, and are not always controllable.

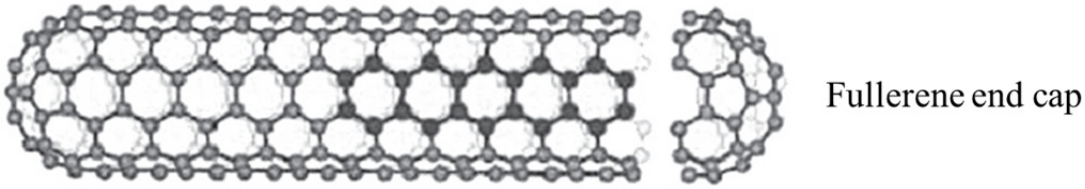

Figure 3. Chemical structure of carbon nanotube.[14]

2.1.1 Graphitic structure chemistry

From a chemical point of view, both CNTs and graphene are made of sp2 carbon atoms and crystallize in the hexagonal form of a honeycomb lattice. Their basic graphitic structure is made of carbon-carbon double bonds. Chemical reactions to the carbon–carbon double bonds cause the transformation of sp^2 into sp^3 hybridized carbon atoms, which is associated with a geometrical change of the carbon atom from trigon to tetrahedron. Chemical functionalization in this manner basically damages their pristine electronic and mechanical properties.

The direct functionalization with organic groups is possible through reactions with reactive species such as nitrenes, carbenes, and radicals.[24] One example of the reaction through radicals is the reaction of CNT or graphene with diazonium salts. During the reaction, aryl radicals were formed by the extrusion of N_2 and then reacted

with the graphitic structure. Various approaches have been developed to covalently functionalize CNTs or graphene via diazonium salts (**Figure 4** and **Figure 5**).[25] For example, aryldiazonium salts can react efficiently with SCWNTs in water to form aryl functionalized SWNTs. Remarkably, the resulting SCWNTs have up to 1 in 9 carbons along their backbones bearing an organic moiety and they can be dispersed in organic solvents, even with these relatively small functional moieties.[26] Similarly, surfactant-wrapped graphene sheets obtained from reduction of GO with hydrazine were successfully functionalized by aryldiazonium salts. The resulting functionalized nanosheets have good dispersion in polar aprotic solvents, allowing alternative avenues for preparing polymer nanocomposites.[27]

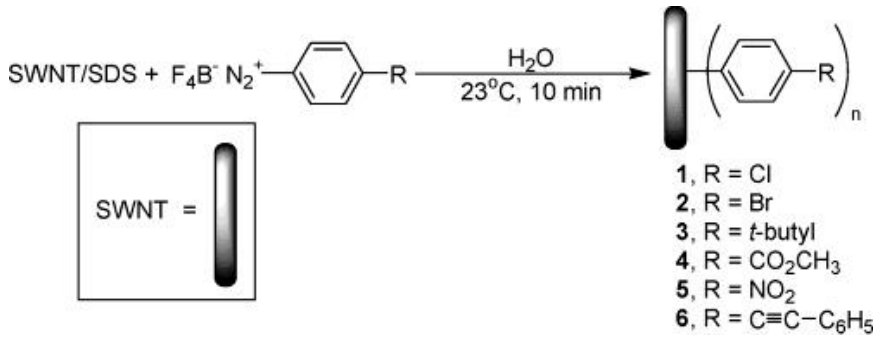

Figure 4. Covalent functionalization of SWCNTs with aryldiazonium salts.[25]

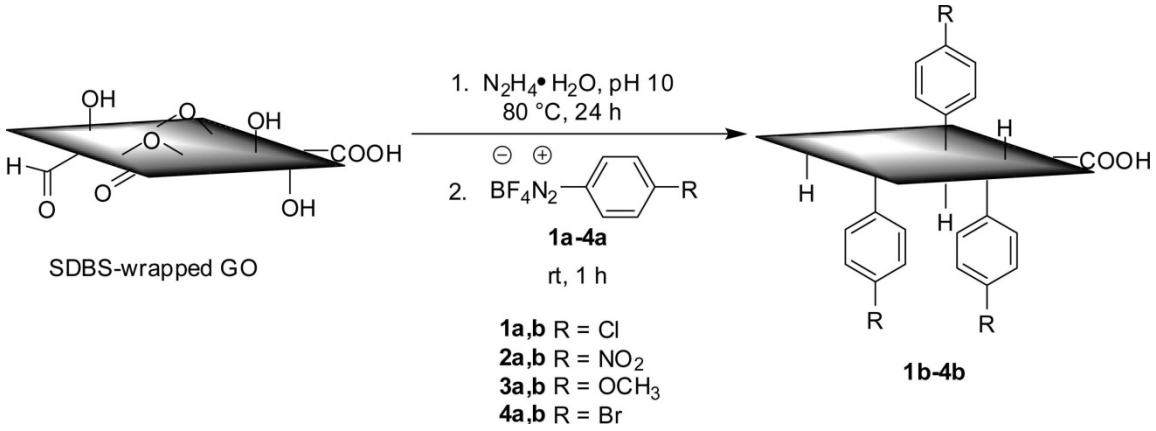

Figure 5. Covalent functionalization of GO with aryldiazonium salts.[25]

2.1.2 Defect site chemistry

The defect site chemistry is to take advantage of the defective sites on CNTs or graphene sheets to minimize the damage to their structure for the purpose of functionalization. The as-produced CNTs are not as perfect as they were once thought to be. The possible defective structures can be classified into four main groups: topological defects (ring sizes other than hexagons), rehybridization (ability of the carbon atom to hybridize between sp^2 and sp^3), incomplete bonding defects (vacancies and dislocations), and doping with other elements than carbon.[28] The topological defects at the caps of the nanotube, such as five- or seven-membered rings, have a similar structure to fullerene. These defect sites have a relatively higher reactivity, comparable to the reactivity of the graphitic structure. Defects in this manner are therefore a promising starting point for the development of the covalent chemistry of CNTs. However, up to date only limited work has been reported to employ these defective sites of CNTs.

Within the rich fullerene chemistry there is a very suitable reaction employing simple and common reagents: organic amines. It was discovered that primary and

secondary amines can react with fullerene at room temperature. Basiuk *et al.* reported a successful, direct solvent-free amination of MWCNTs with octadecylamine (ODA) at reduced pressure (10^{-2} Torr) and high temperature (160–190 ^{o}C). [29] The site specificity of reaction was found to depend on the mutual position of pyracyclene units in the closed caps and pentagons on the MWCNT sidewalls. However, the major drawback to this approach is its relatively high temperature and vacuum reaction condition, thereby making it impractical for commercial application.[30]

Another type of defects for CNTs is oxygenated functionalities, introduced by the purification process. All known production methods of CNT generate impurities, like amorphous carbon and catalyst nanoparticles. The techniques applied for the purification of the raw material is acid oxidation,[31, 32] which induces the opening of the tube caps as well as the formation of holes in the sidewalls. The final products are nanotube fragments with ends and sidewalls decorated by oxygenated functionalities, mainly carbonyl and carboxylic groups. The chemical nature of these moieties has been well studied and employed for further functionalization. One of the most popular functionalization methods is amidation reaction with amine groups (**Figure 6**). For example, Chen et al. treated oxidized nanotubes with long chain alkylamines via acylation and made for the first time that the functionalized material is soluble in organic solvents.[33] In conclusion, the inherent defects (five- or seven-membered rings) and oxygen-containing groups on CNTs are the two main types of defects used for further functionalization. Defects in this manner are therefore a promising starting point for the

development of the covalent chemistry of CNTs, at the same time without causing further damage to the structure of CNTs.

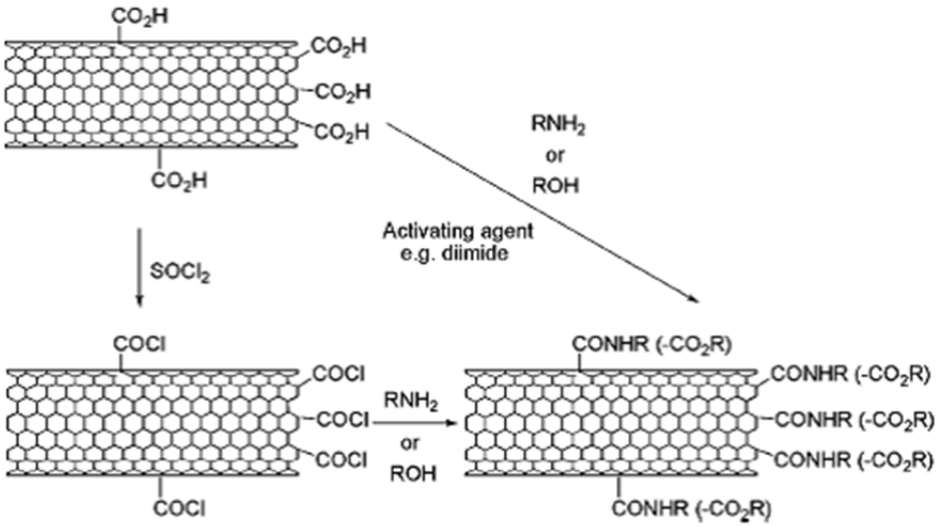

Figure 6. Chemical reactions of acid-cut nanotubes through the defect sites of the graphitic surface.[33]

The defect sites for GO are more complex than CNTs. As stated in the above section, GO sheets have chemically reactive oxygen functionalities, such as carboxylic acid groups, epoxide and hydroxyl groups, according to the widely accepted Lerf–Klinowski model.[22] These reactive sites behave like defect sites on GO. An ideal approach to the chemical modification of GO would employ reactions of these groups to selectively functionalize one type of goup over another. The reactions utilizing carboxylic acid groups have been developed for CNTs, and many of these reactions can be and have been applied to GO.[23] In addition to the carboxylic groups, the epoxy groups are very reactive through ring-opening reactions under various conditions. Nevertheless, the demonstration of the selectivity of these chemical transformations remains

challenging. In some instances, reaction with multiple functionalities is possible, and it is impossible to separate the product due to the wide range of chemical compositions present in the GO.[20] Stankovich, et al. reported a functionalization method of GO with organic isocyanates (**Figure 7**). The isocyanate treatment resulted in the functionalization of the carboxyl and hydroxyl groups in GO via formation of amides and carbamate esters. These isocyanate-treated GO could form a stable dispersion in polar aprotic solvents.[34]

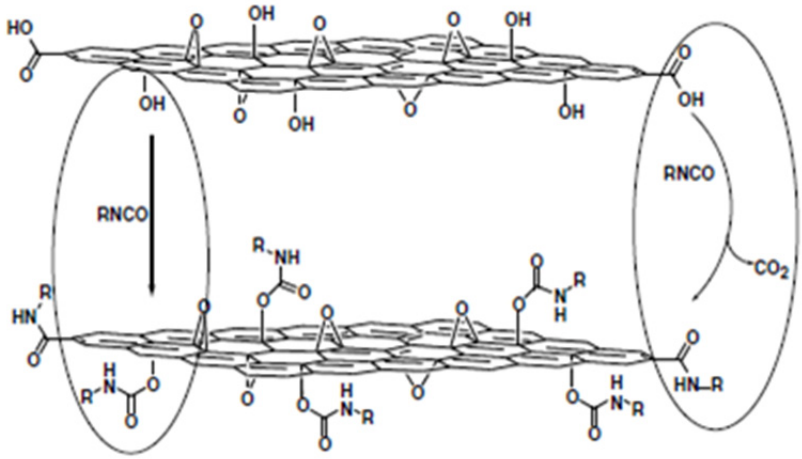

Figure 7. Reaction scheme of GO with isocyanates.[34]

2.2 Noncovalent functionalization

The second approach to functionalize CNTs or graphene is the noncovalent method. In this frame, these materials can be modified via van der Waals forces, electrostatic interaction, and π-π interactions, by adsorption of aromatic compounds, surfactants, polymers, or even nanoparticles. In contrast to covalent functionalization, the noncovalent method has advantages, including ease and reversibility of the

decoration process with minimized risk of permanently altering the intrinsic structures and properties of CNTs and graphene.

The formation of noncovalent interaction with surfactants or polymers has shown themselves to be suitable methods for the noncovalent functionalization of CNTs (**Figure 8**). It has been shown that nanotubes can be transferred to the aqueous solvents in the presence of traditional surfactants, such as sodium dodecylsulfate (SDS),[35] dodecyl-benzene sodium sulfonate (NaDDBS),[36] Triton X-100,[37] and cetyltrimethylammonium bromide (CTAB).[38] It is believed that the nanotubes are in the hydrophobic interiors of the corresponding micelles. Water-soluble polymers, polyvinyl pyrrolidone (PVP) and polystyrene sulfonate (PSS),[39] are also used to wrap CNTs, which is driven largely by a thermodynamic force to eliminate the hydrophobic interface between the tubes and their aqueous medium. Further changing the solvent system can unwrap CNTs with the separation of the polymer from CNTs.

GO can also exhibit non-covalent binding on the sp^2 networks via π–π interaction or engage in hydrogen bonding through the presence of carboxylic and hydroxide groups. Liu, et al. reported a protein-conjugated GO that bovine serum albumin (BSA) stably adsorbed on the basal planes of GO (**Figure 9**).[40] The adsorption is due to the hydrophobic and hydrophilic patches on the BSA's surface through hydrogen bonding, which also makes them well-known for the adhesiveness to solid surfaces. The authors further demonstrated that the incorporation of protein turned GO into general platforms toward the assembly of nanoparticles with varying sizes, shapes, compositions, and surface properties.

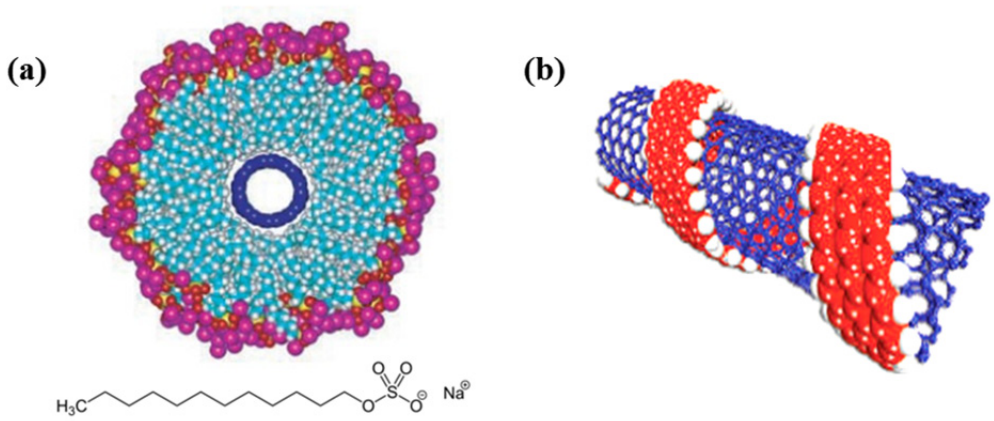

Figure 8. (a) Cross section model of an individual nanotube in a cylinder SDS micelle, and (b) wrapping arrangement of PVP on an individual tube.[35]

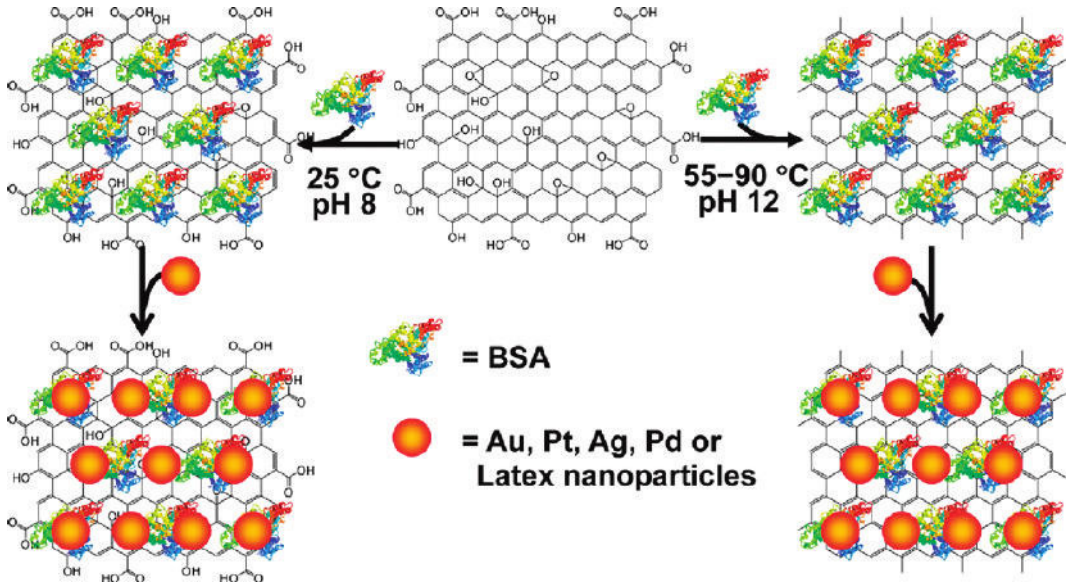

Figure 9. Protein-conjugated GO and its decoration with various nanoparticles.[40]

2.3 Applications of functionalized CNTs and graphene

As illustrated in the previous sections, many molecular species could form covalent or noncovalent interactions with CNT and graphene. The unique properties of CNTs or graphene can now be coupled with other classes of material. This combination

provides a basis for the further application of CNTs and graphene in the fields of nanotechnology. Among these applications, I will focus on electrically conductive thin films and catalysts in fuel cells.

Conductivity and high aspect ratio of CNTs and graphene provide them a platform for producing transparent and conductive thin films. These thin films are important components in many electronic devices, including touch screens, flat panel displays, photovoltaic cells, and organic light-emitting diodes.[17, 41-43] Especially, CNT thin films with good electrical conductivity and high flexibility have received much attention in recent years due to their potential for replacing indium tin oxides as transparent electrodes. Wu et al. prepared SWCNT thin films with a low electrical resistance of 30 ohm/square and an optical transmittance of >90% through a filtration method (**Figure 10**).[44] The preparation process includes three steps: (i) vacuum-filtering a dilute, surfactant-based (1 wt.% Triton X-100) suspension of nanotubes onto a filtration membrane; (ii) washing away the surfactant with water; and (iii) dissolving the filtration membrane in organic solvent. The authors claimed that three factors are corresponding to the excellent performance of CNT thin films: (i) low carrier density; (ii) high electronic mobility; and (iii) the suppression of light absorption and reflection for polarization components perpendicular to the nanotube axis, which reduces the optical density of the disordered SWNT films for unpolarized incident light. Such films are likely to find application as transparent conductors in the IR and flexible/foldable displays.

CNT and graphene not only serve as key components of nanocomposite materials; they also are ideal templates to control the structures and properties of other nanomaterials because of their good electronic and mechanical properties, high aspect ratio, and tunable surface chemistry. Nanoparticles (NPs), due to their unique electronic, optical, magnetic and catalytic properties, have emerged as a class of compounds that are particularly attractive for fabricating CNT/NP or graphene/NP composites.[45] In these nanocomposites, the CNT or graphene surface serves as a template where NPs are either nakedly absorbed on their surface or linked through organic fragments. The combination of the two classes of material (CNTs or graphene and NPs) may lead to a successful integration of the properties of the two components in the new hybrid materials that present important features for catalysis and nanotechnology.[46] Especially, transition metal nanoparticles, like Au, Pt, Pd, Ru, and Ag NPs, have been extensively studied in catalysis for petroleum processing, energy conversion, and pollutant removal.[47-51] The use of NPs results in large contact areas between the active material of the catalyst and the surrounding environment.[52] This ensures that the NPs are used effectively as a catalytic material. One of the challenges associated with the use of NPs as catalysts is that the high surface area reduces the colloidal stability, drives the aggregation of the NPs, and lowers the catalytic activity.[53] Another challenge is post-reaction separation and the reusability of the tiny particles.[54] To overcome these challenges, heterogeneous catalysts based on CNT- or graphene-supported NPs have emerged as a new class of nanocomposites to improve the colloidal stability and catalytic efficiency. Additionally, theoretical calculations have predicted that the high mobility of charge carriers on

graphene would enhance the catalytic activity through the charge transfer from the clusters to the substrates.[55]

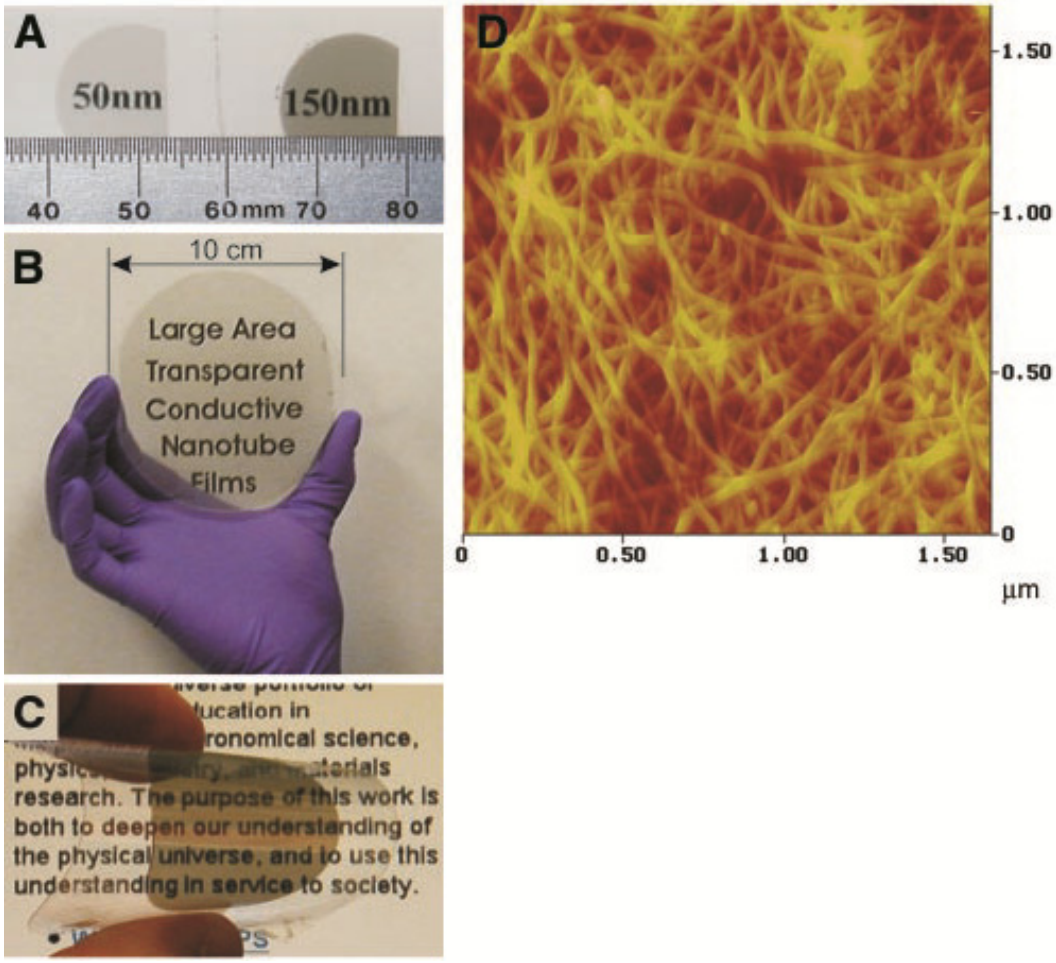

Figure 10. (a) Films of the indicated thickness on quartz substrates, (b) a large, 80-nm-thick film on a sapphire substrate 10 cm in diameter, (c) flexed film on a mylar sheet, and (d) AFM image of a 150-nm-thick SWCNT film surface.[44]

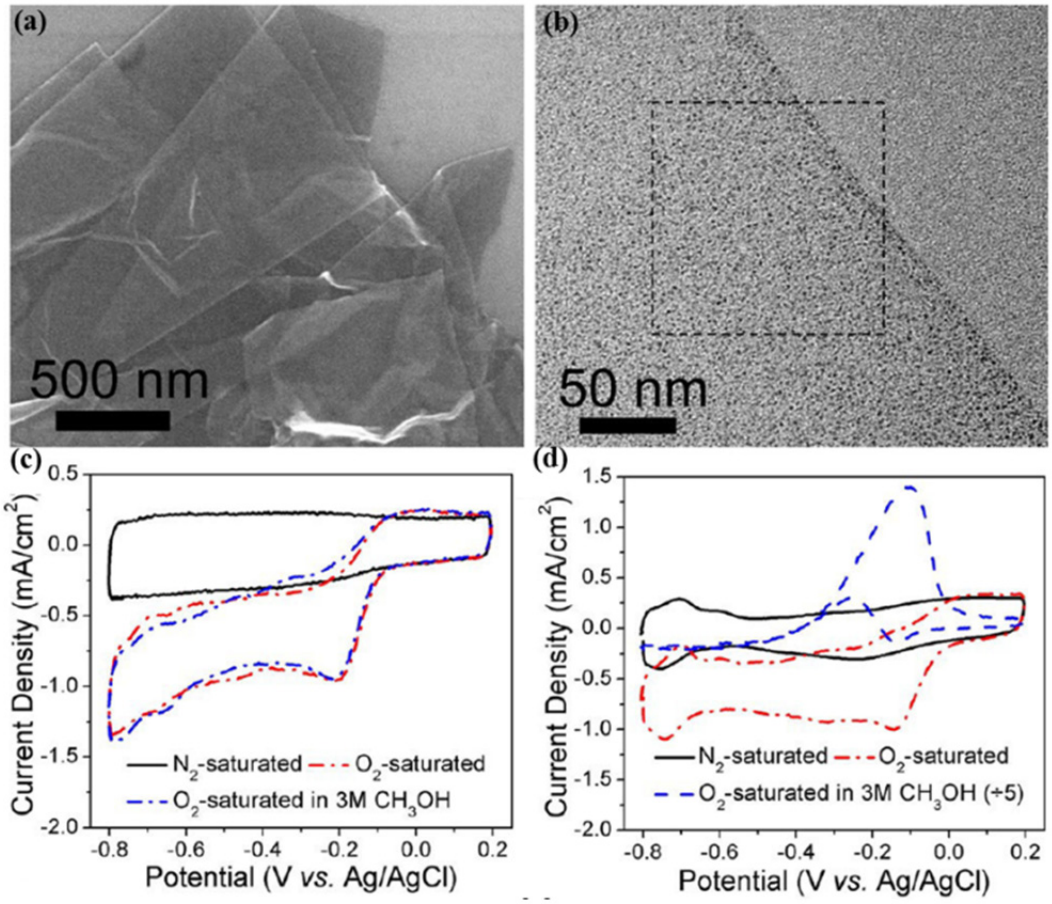

Figure 11. SEM (a) and TEM (b) images of Au/graphene hybrids, and CV curves of (c) Au/rGO hybrids and (d) commercial Pt/C (20 wt.%) on a glass carbon electrode.[54]

Yin et al. reported a novel and simple strategy to grow Au and other metal (Pt, Pd) clusters on the reduced graphene oxide (rGO) sheets.[56] The formation mechanism of Au/rGO hybrids was in two steps: 1) the highly negative-charged rGO sheets exhibit high absorption capacity toward positive-charged Au (III) ions via partial replacement of Cl ligands; 2) the heteroatoms on the rGO sheets, especially for N atoms, act as the initial nucleation site for Au clusters. The selective absorption and the restricted deposition of Au (III) ions on the rGO sheet are the prerequisite condition for generating the Au/rGO hybrids. Only the rGO sheets with the moderate number of the

heteronuclear sites, as well as the moderate reducing capability, give rise to the production of Au/rGO hybrids. On the basis of the above formation mechanism, other metals, like Pd and Pt, were successfully synthesized. The potential application for these metal/graphene hybrids are the oxygen reduction reaction (ORR) at the cathode of fuel cells. A major limitation for the practical application of fuel cells is the sluggish kinetics of the ORR, which gives rise to the larger overpotential and lower current density. Generally, Pt and Pt alloys are the most active catalysts for ORR; however, they still suffer from serious durability and reliability problems including the crossover and poisoning effects. The Au/rGO hybrids exhibit excellent electrocatalytic performance toward ORR, which has a comparable onset potential to commercial Pt/C catalyst, but superior methanol tolerance and enhanced electrocatalytic stability.

CHAPTER III

ELECTRICALLY CONDUCTIVE SUPERHYDROPHOBIC OCTADECYLAMINE-FUNCTIONALIZED MULTIWALL CARBON NANOTUBE FILMS*

3.1 Introduction

Recently, electrically conductive superhydrophobic carbon nanotube (CNT) films have received considerable attention for use in various applications such as solar cells,[57] flexible optical devices and electrical devices.[44, 58] To fabricate superhydrophobic films, the surface roughness and surface energy state of the material must be considered. Surface functionalization or control of CNT film texture can help manipulate their wettability and lead to superhydrophobicity. In early studies, Sun et al.[59] reported that aligned CNTs showed a high water contact angle (CA) of about 159^{o}. However, water droplets are not stable on the aligned CNT films and eventually penetrate into the gaps within the CNT forest. To overcome this problem, low surface energy polymers are often used to coat the aligned CNTs. Poly(tetrafluoroethylene) coated CNT forests exhibited a remarkable superhydrophonicity with a CA of 170^{o}.[60] A superhydrophobic surface was also prepared by coating fluoroalkylsilane, and the film showed a CA of about 171^{o}.[61] However, one drawback with polymer coating is the reduction of the film electrical conductivity. Furthermore, the potential application of aligned CNT superhydrophobic materials is limited due to the difficulty in their preparation.[60]

---

* Reprinted from Carbon, 53, H. Yao, C.-C. Chu, H.-J. Sue, R. Nishimura, Electrically conductive superhydrophobic octadecylamine functionalized multiwall carbon nanotube films, 366–373, Copyright (2013), with permission from Elsevier.

Randomly laid CNT films, as opposed to aligned CNT films, would provide a much easier and more economical method to prepare superhydrophobic films. There are two main approaches for producing superhydrophobic CNT films: (1) adsorption or wrapping by low surface energy polymers as a result of van der Waals forces and π-π interactions[62] and (2) covalent attachment of hydrophobic groups through reactions on the conjugated skeleton of CNTs.[63-65] The first approach is best demonstrated by Luo et al.[62] who took advantage of the good compatibility between Nafion and CNTs to fabricate Nafion/CNT nanocomposite films by the vacuum filtration process. The CNT composite film attained a CA of 165^o and a small sliding angle (SA) of 3.3^o with 9.8 wt% Nafion. Poly(dimethylsiloxane) coated randomly laid CNT film possessed a high water CA of 167^o and a small SA of less than 3^o.[66] The covalent functionalization of MWCNTs has been successfully demonstrated using a number of hydrophobic groups. Fluoropolymer grafted MWCNT films created a superhydrophobic surface with a CA of 160^o.[63] Poly(acrylic-acid)-block-polystyrene functionalized MWCNT films has a CA of 166^o, and the water droplet could easily roll off the surface with a SA of about 5^o at 20% grafting weight.[64] Although these functionalized MWCNT films all exhibit high water CA, the synthesis routes to achieve such functionalization of MWCNTs are quite complex. They involve either acid oxidization of MWCNTs, which decreases electrical conductivity, or multiple tedious synthesis steps to attain the desired functionalization. In this work, we report a one-step chemical functionalization method to functionalize MWCNTs. The MWCNT-ODA thin films prepared show a high CA of 165^o and a low SA of 3^o.

Recently, Basiuk et al reported successful direct solvent-free amination of MWCNTs with octadecylamine (ODA) at reduced pressure (10^{-2} Torr) and high temperature (160~190^{o}C).[29] The site specificity of reaction was found to depend on the mutual position of pyracyclene units in the closed caps and pentagons on the MWCNT sidewalls. The major drawback to this approach however is its relatively high temperature and vacuum reaction condition, thereby making it impractical for commercial application. The development of an approach to functionalize MWCNTs in a commercially viable environment would therefore be of great benefit.

In this paper, a new method is reported to carry out amination reactions to functionalize MWCNTs in a mild condition, i.e., 80^{o}C in air at atmospheric pressure. The MWCNTs were functionalized by ODA at various weight ratios to prepare thin films through a one-step vacuum filtration process. The effectiveness and usefulness of this approach may allow for industrial production and application of highly conductive, superhydrophobic MWCNT films.

3.2 Materials and methods

3.2.1 Materials

The MWCNTs were provided by SouthWest NanoTechnologies, Inc, and used as received. The MWCNT diameter distribution is 75% of tubes < 9 nm and 90% < 12.2 nm, with an average aspect ratio of ~ 1,000, and carbon content ≥ 98%. ODA and other solvents were purchased from Sigma-Aldrich and used as received.

3.2.2 Synthesis of MWCNT-ODA hybrids

MWCNTs (50 mg) were dispersed in 100mL of deionized-water by 1 h of ultrosonication to form a homogeneous solution. Then the mixture was continuously stirred at 80^{o}C. ODA (250 mg) was dissolved in 10 mL methanol and then added to the MWCNT suspension. The mixture was stirred at 80^{o}C for 1 hour. The product was filtered and washed thoroughly with methanol (30 mL), acetone (30 mL) and chloroform (30 mL) sequentially to remove the remaining ODA. The black powder was dried at 60^{o}C in a vacuum oven overnight.

3.2.3 Preparation of MWCNT-ODA films

The MWCNT-ODA solution was ultrasonically dispersed in methanol for half an hour to obtain a homogenous suspension. The MWCNT-ODA films were prepared by filtering the solution through filter paper and were easily peeled off without displaying any visible damage. The collected films were then dried in a vacuum oven overnight at 60^{o}C.

3.2.4 Characterization

Characterization and analysis of the MWCNT films was performed using a variety of methods and equipment. Both Raman and Fourier-transform infrared attenuated total reflectance (FTIR-ATR) characterization were performed using the pristine and functionalized MWCNT films directly. Raman spectra were acquired on a confocal Raman spectroscope (Horiba Jobin-Yvon Lab RAM HR system) with 632 nm laser excitation under ambient conditions. FTIR-ATR spectra were acquired using Nicolet 380 (Thermo Fisher Scientific) in conjunction with ATR accessory (AVATAR

OMNI Sampler, Germanium crystal) under ambient conditions. Thermal gravimetric analysis (TGA) of both pristine and functionalized MWCNTs was performed with 2~3 mg of solid powder. The test (Q500, TA Instruments) was run from 30°C to 900 °C with a ramp rate of 20°C/min in air. The pristine and functionalized MWCNT films were directly analyzed using X-ray photoelectron spectroscopy (XPS). XPS data were obtained with a Kratos Axis Ultra using a nonmonochromatic MgKa photon source (1486 eV). Data were fit using XPSPEAK 4.1 by applying a Linear-type background correction. The surface morphology of the pristine and MWCNT-ODA films was examined using field emission scanning electron microscopy (SEM) (JSM-7500F, JEOL). A Keyence VK9700 violet laser scanning confocal microscope (VLSCM) was used for quantitative surface roughness determination. The microscope is equipped with a 408 nm wavelength violet laser and has an x–y-axis resolution of ~250 nm and a height resolution of ~1 nm. The VK-Analyzer software provided with the microscope was used to obtain surface roughness values. A total of five measurements were taken for each film from five different locations with a sampling area of 1 mm x 1 mm. Measurement was averaged for each film to determine the sample surface roughness. Contact angle (CA) was measured with an optical contact angle and surface tension meter apparatus (CAM 200, KSV, Finland) at ambient temperature. The volume of the individual water droplets was controlled at 5 μL. The average CA values were obtained by measuring at five different locations for each sample. The liquid-air-solid interfaces were directly observed with an OLYMPUS BX60 microscope in reflectance mode under ambient temperature. The volume of the individual water droplets was controlled at 5 μL. The

focus was adjusted to observe the interface between the film surface and the water droplet. Four-point probe measurements were also done with an Agilent Digital Multimeter (Agilent Technology, US) with the tip spacing set at 1.6 mm. The average electrical conductivity values were obtained by measuring five different locations on the same film sample.

3.3 Results and discussion

The covalent functionalization of CNTs allows functional groups to be preferentially attached to the tube caps and/or defective sidewalls. These caps have a semi-fullerene-like structure, which is critical for the functionalization reaction to take place. The chemical reactivity of the CNTs is also strongly influenced by the presence of defects on the sidewalls. The presence of defects, such as vacancies or pentagons, results in a localized increase in the chemical reactivity of the graphitic nanostructures. Attachment of amines, such as n-propylamine and n-dodecylamine to fullerene (C_{60}), were reported decades ago,[67] and are among the earliest reactions observed in the fullerene family. The reaction sites for amine addition are the six independent pyracyclene units existing in C_{60}. Recently, it was reported that amine addition could also take place on the MWCNT surface, especially on pyracyclene units in the closed caps and side walls of pentagons.[29] A solvent-free functionalization procedure was introduced at reduced pressure (10^{-2} Torr) and high temperature (160~190^{o}C). Under these conditions, ODA was vaporized to react with MWCNTs. However, this reaction condition is relatively harsh and complex.

In this research, a simpler route using a co-solvent of water and methanol was used to facilitate the ODA reaction with MWCNTs at a mild temperature of 80°C. The addition of methanol is to facilitate ODA dissolution in the solution. After reacting for 1h at 80°C, the mixture of MWCNTs and ODA was filtrated and the unreacted ODA was washed away. The synthesis route is illustrated in **Figure 12**. The MWCNTs employed for the present study contain a high level of surface defects as indicated by the I_D/I_G intensity ratio obtained from the Raman spectra. The I_D/I_G intensity ratio for pristine MWCNTs is 2.1, which means amination is likely to take place more readily.[68] Various quantities of ODA were used to react with MWCNTs to study how amination of MWCNTs influences the electrical conductivity and superhydrophobicity of the films.

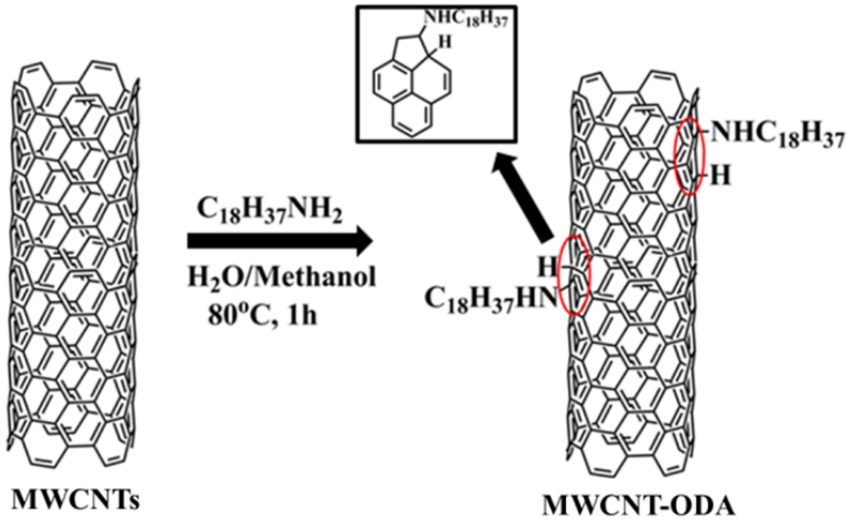

Figure 12. Chemical attachment of ODA to MWCNTs (circular areas show the specific sites of reaction).

TGA was used to confirm amination of ODA on the MWCNT surfaces. **Figure 13** shows the TGA spectra of pristine MWCNTs, pure ODA, and MWCNT-ODA. As

shown, ODA exhibits a rapid weight loss starting at a temperature as low as 120^{o}C, and has nearly 90 wt. % weight loss between 120^{o}C and 230^{o}C. This finding is not unexpected and is in agreement with literature results.[69] On the other hand, pristine MWCNTs have good thermal stability below 230^{o}C, and begin to degrade at around 500^{o}C. For the MWCNT-ODA, the weight loss due to organic species decomposition was observed in a temperature range of 300^{o}C to 500^{o}C. It has been reported that physisorbed ODA molecules should degrade at temperatures between 150^{o}C to 300^{o}C.[65] The onset of the decomposition temperature for ODA in MWCNT-ODA is observed to increase from 150^{o}C to 300^{o}C, which suggests that ODA has been chemically grafted onto the surfaces of the MWCNTs by direct amination.[29] The weight loss attributed to ODA is estimated from the TGA results in the 300 to 500^{o}C temperature range. Additionally, the highest mass percentage of the grafted alkyl chains in MWCNT-ODA was determined to be 14 wt. % even after extending the reaction time to 24 hrs.

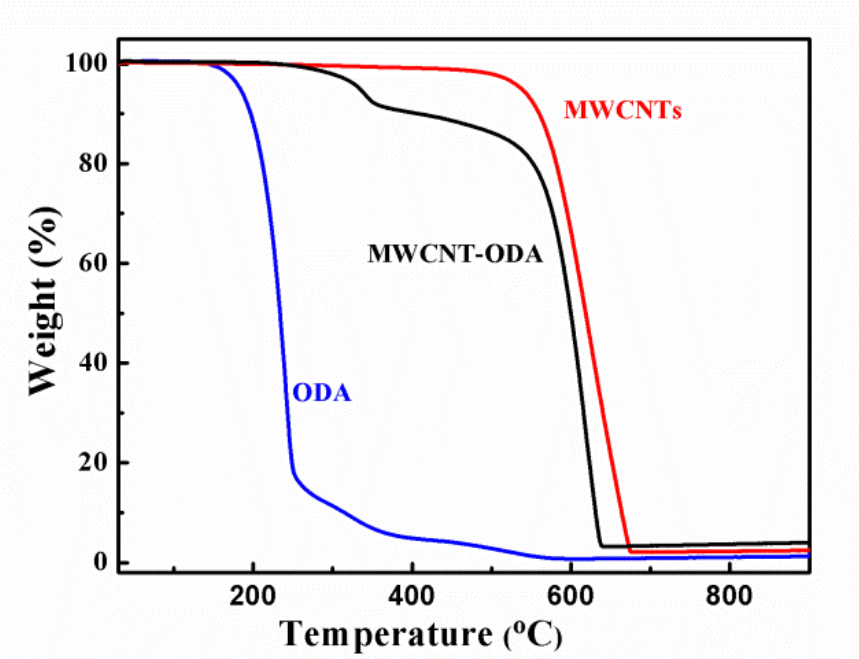

Figure 13. TGA curves of ODA, pristine MWCNTs, and MWCNT-ODA.

FTIR was also used to characterize the derivatized materials as shown in **Figure 14**. The MWCNT-ODA spectrum shows that functional organic moieties manifest themselves mostly in two wavelength regions, at 2800-3000 and 1500-1000 cm^{-1}. The absorption peaks at 1640 and 1574 cm^{-1}, shown both in MWCNTs and MWCNT-ODA spectra, originate from the C=C stretching modes of MWCNTs.[65] The peaks at 2918 cm^{-1} and 2856 cm^{-1} correspond to C-H symmetric and asymmetric stretching vibrations of the aliphatic hydrocarbon groups.[68] The peaks at 1450 cm^{-1} and 1260 cm^{-1} are attributed to the C-H bending and C-N stretching, respectively.[70] All these characteristic absorption peaks were attributed to the presence of the ODA amino group, which gave a strong indication of the attachment of ODA to the side walls in the nanotube.

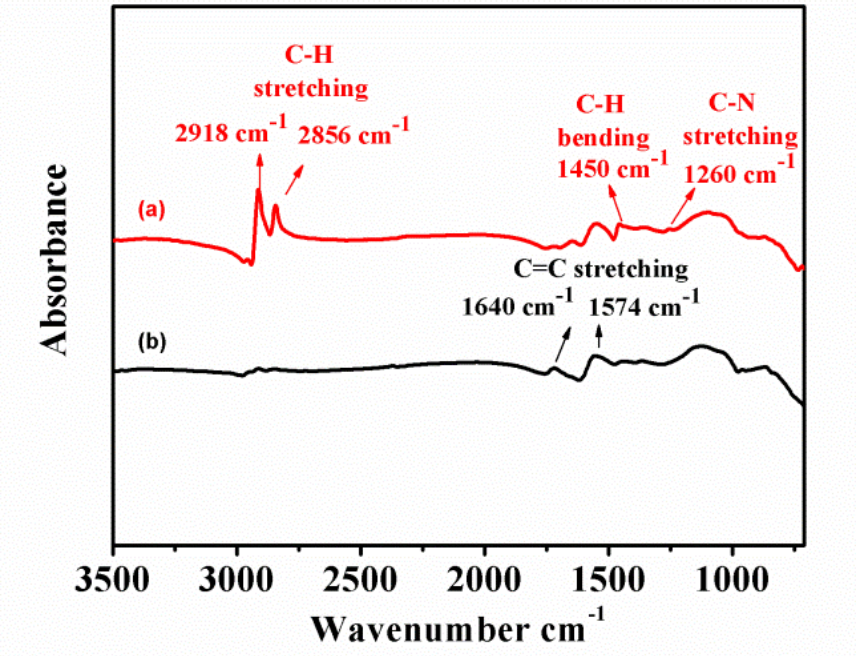

Figure 14. Infrared spectra of (a) MWCNT-ODA and (b) pristine MWCNTs.

Furthermore, XPS was carried out to investigate the chemically grafted ODA on the MWCNT surfaces. **Figure 15** displays XPS spectra in the C 1s region of functionalized MWCNTs. After the chemical attachment of long alkane groups, the C 1s peak consists of two main components: the peak centered at about 285.5 eV corresponding to C-H in ODA[71] and the peak at 284.5 eV, which is assigned to the sp2 hybridized C atoms of the MWCNTs. Additionally, the N 1s spectrum of MWCNT-ODA shows one peak centered at about 400.0 eV. This peak is assigned to be from amino groups and confirms the presence of ODA amino groups on the MWCNT surfaces.[72] Elemental analysis based on the XPS data shows an approximate 0.9 % atomic concentration of N compared with C. This is in agreement with the TGA results, which shows a theoretical 0.6% atomic concentration of N.

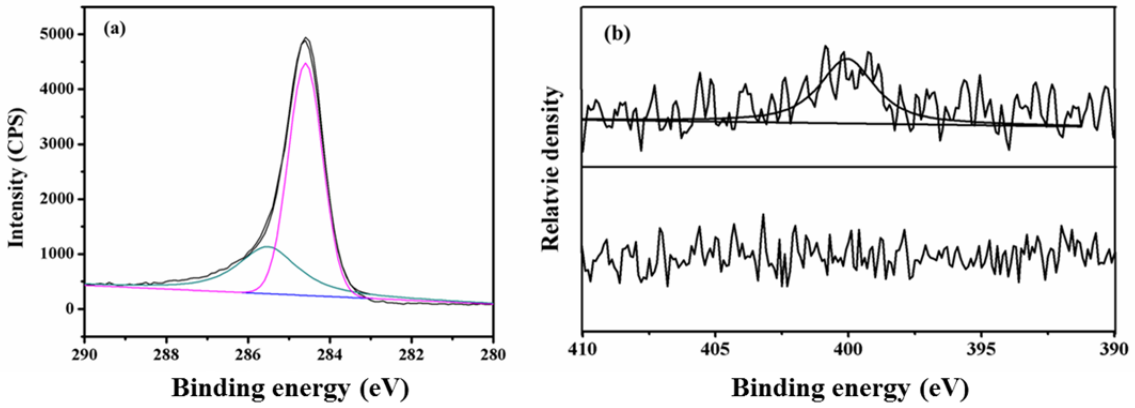

Figure 15. XPS spectra of (a) MWCNT-ODA in the C 1s region and (b) MWCNT-ODA (top) and MWCNTs (bottom) in N 1s region.

CNT films are typically prepared by chemical vapor deposition (CVD),[59] spray coating,[73] vacuum filtration,[62] or solution casting.[65] In this work, a facile and low-cost vacuum filtration process was selected. The process readily allows both pristine MWCNTs and functionalized MWCNT-ODA to intimately form nominally homogeneous films, which can be peeled off from the filtration paper. The free standing circular MWCNT-ODA film with a diameter of 55 mm is shown in **Figure 16**. The film is of good quality, without visible pinholes or cracks. **Figure 16**b shows SEM images of the cross-section of this film, which consists of tightly packed MWCNTs. This demonstrates that vacuum filtration is an effective method to prepare high quality MWCNT thin films.

One potential application of MWCNT-ODA is to fabricate electrically conductive superhydrophobic films to serve as self-cleaning, conductive components. **Figure 17** shows the CAs for MWCNT films with different degrees of ODA grafting. The pristine MWCNT film exhibits a relatively high water-absorbing property with a

CA of 31±1°. Functionalization of the MWCNTs with ODA as little as 6 wt. % dramatically converts a hydrophilic surface into a hydrophobic one, with a CA of 135±1°. As the ODA functionalization is increased to 14 wt. %, the surface becomes superhydrophobic and attains an even higher CA of 165±2°.

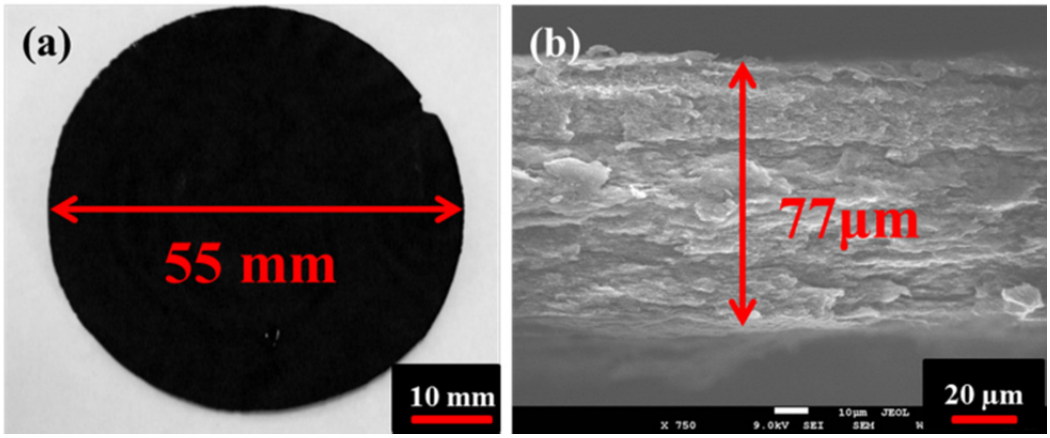

Figure 16. (a) Visual image of a free-standing MWCNT-ODA film peeled from a filtration membrane, and (b) SEM images of the cross section of a MWCNT-ODA film.

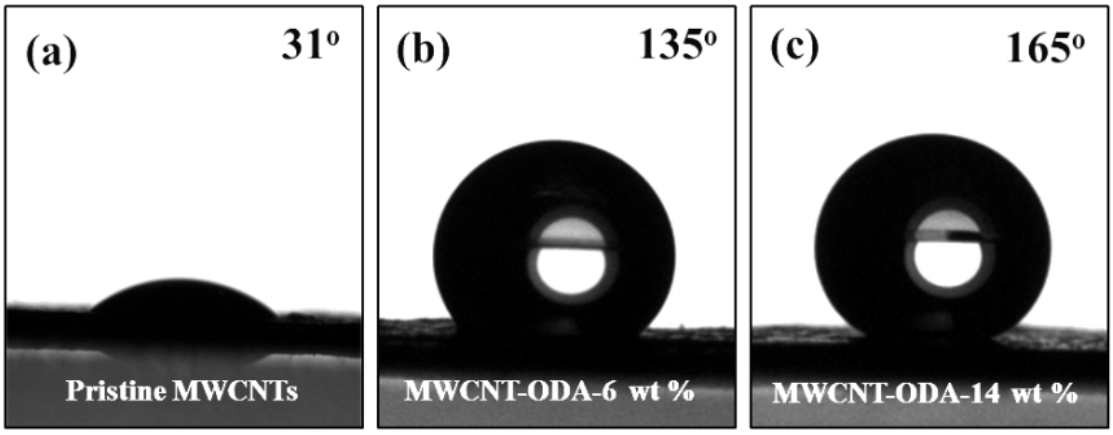

Figure 17. Profile of a water droplet on pristine MWCNT and MWCNT-ODA films.

According to Wenzel's and Cassie's states,[74, 75] hierarchical structures and low surface free energy should be considered to produce a superhydrophobic surface. **Figure 18** depicts SEM images of pristine MWCNTs and MWCNT-ODA films at low and high magnifications, respectively. The film surface exhibits a surface roughness on both micro- and nano-scales. Numerous randomly formed micro-islands are present on the surface (**Figure 18**a, c, and e). **Figure 18**(b, d, and f) displays a hierarchical nano-textured morphology formed by the entanglement of MWCNTs on the nano-scale. The formation of these structures can be assumed to result from the vacuum filtration process.[62] The reasoning is that the MWCNTs or MWCNT-ODA could not be dissolved in the methanol and water co-solvent to form a uniform solution. As the tubes are accumulated under low-pressure filtration, the entangled MWCNTs or MWCNT-ODA are randomly laid down on the filtration paper. In regions containing a higher concentration of tubes, the corresponding local section of the films form protruded structures, creating the rough and porous surfaces. The surface structures found in these films more efficiently trap air under the water droplet, thus better separating the liquid-solid phases.

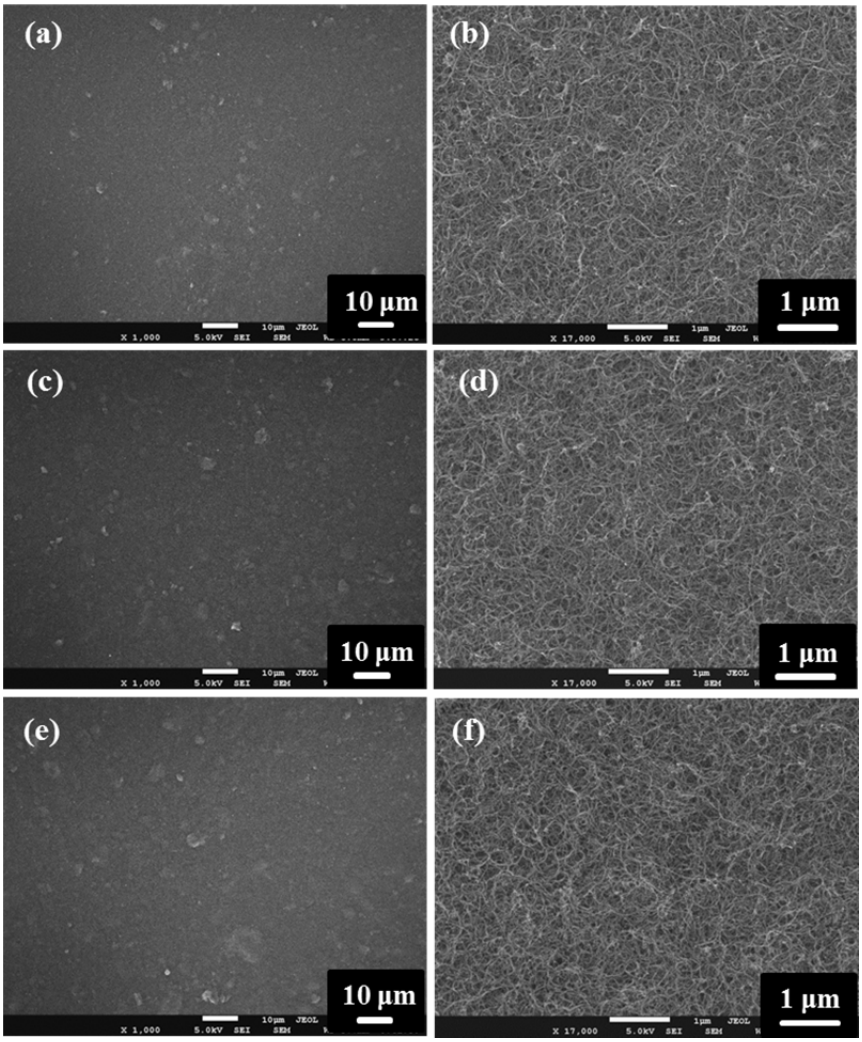

Figure 18. SEM images of (a) pristine MWCNTs film, (b) high magnification of (a), (c) MWCNT-ODA-6 wt. %) film, (d) high magnification of (c), (e) MWCNT-ODA-14 wt. % film, and (f) high magnification of (e).

To determine the average surface roughness of the MWCNT films, the surface roughness values were measured by laser confocal microscopy. All these films show a root mean-square-average surface roughness, R_q, in the range of 8 to 9 µm, which indicates these films exhibit similar surface roughness characteristics (**Table 1**). The difference in surface roughness between MWCNTs and MWCNT-ODA hybrid films is not sufficient to explain the observed discrepancy in wettability between the films. It is

likely that the surface free energy is the most significant factor in the observed change in wettability. It has been reported[69] that the surface energy is 29.98 mJ/m^2 for octadecane and 54.8 mJ/m^2 for graphite. When MWCNTs are functionalized with ODA, the octadecyl groups are exposed instead of the high surface free energy of MWCNTs. This functionalization transforms the film to a state of lower surface energy. With an increasing degree of functionalization with ODA, more and more octadecyl groups are attached to the surface of MWCNTs. Therefore, the MWCNT-ODA film surface wettability changes from being hydrophilic to superhydrophobic as a result of the lowered surface energy.

Table 1. The roughness values of different films.

Films	Average Roughness Value (μm)	Standard deviation (μm)
MWCNTs	8.955	0.794
MWCNT-ODA_6 wt. %	8.997	1.656
MWCNT-ODA_14 wt.%	8.552	1.244

An ideal self-cleaning surface should exhibit not only a high CA but also a low sliding angle (SA $<5^o$).[76] This means that the water droplet adopts a non-wet-contact mode on the film surface and can easily roll off as a result of a low adhesive force. The SAs were measured on all the above films using 10 μL water droplets. The MWCNT-ODA-14 wt.% film with the highest CA of 165 ± 2^o also exhibited the lowest SA of 3^o. Water droplets were observed to easily roll off this surface. By comparison, the pristine MWCNT film shows a high SA with values exceeding 90^o and was found to absorb a 10

μL water droplet after only several seconds. The high adhesive force between the film and the water droplet is believed to result from the high surface energy of pristine

As observed by other researchers,[63] the air trapped under the water droplet can minimize the contact area. The trapped air is thought to be an important factor for superhydrophobicity, because of the intrinsic high contact angle of air with water, which is known to be around 180°. Therefore, increasing the amount of air trapped at the surface should increase the CAs. The liquid-air-solid three-phase interface is easily observed under an optical microscope.[62] An optical objective lens was set directly above the water droplet. The focus was adjusted to observe the interface between the film surface and the water droplet. It can be clearly seen in **Figure 19** that a dark region occupies the majority of the circular area. The dark region seen in **Figure 19**a is due to the light reflection from the interface between the water droplet and the solid surface, suggesting that the water droplet has infiltrated into the pristine MWCNT film. In contrast, the dark region of the MWCNT-ODA-6 wt. % film (**Figure 19**b) is much more diminished .The bright region due to light reflection from the interface between water and air however, expands to form a few continuous bands within the water droplet contact area. In the case of MWCNT-ODA-14 wt. % (**Figure 19**c), the bright region nearly encompasses the entire water droplet contact area. This indicates that a large amount of air is directly trapped underneath the water droplet. Dark dots seen inside the bright region correspond to the protruded features on the MWCNT-ODA surface. When a water droplet sits on the surface, both the rough surface structure and low surface free energy of the film can trap air under the water droplet. The MWCNT-ODA-14 wt. %

film appears to have trapped the most amount of air underneath the water droplet and accounts for the observed superhydrophobicity.

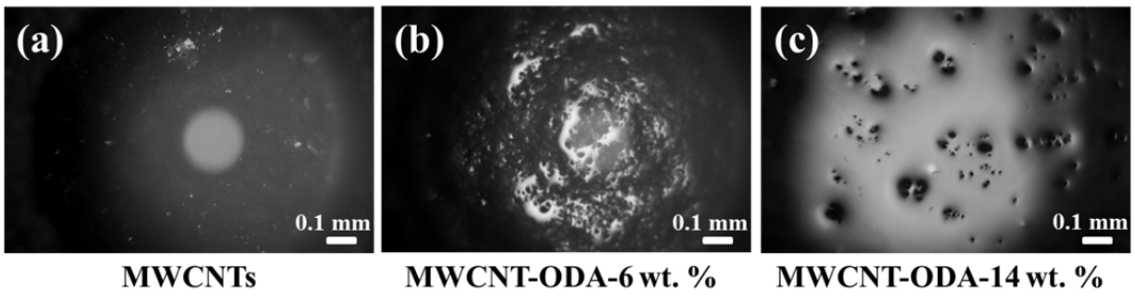

Figure 19. Optical microscopy of the liquid-air-solid interface of the water droplet (5 μL) on (a) pristine MWCNT film, (b) MWCNT-ODA-6 wt. % film, and (c) MWCNT-ODA-14 wt. % film. (The CA values for these films are 31±1°, 135±1°, and 165±2°, respectively.)

Figure 20 displays the dependence of electrical conductivity on ODA content and the results found in literature. The electrical conductivity of CNT thin films has a wide variation from 10^2 S/m to 10^4 S/m because of their differences in orientation, inherent defects in CNTs, and presence of surfactants.[77] A well-aligned CNT buckypaper shows a high electrical conductivity of 2.0 x10^4 S/m due to the well-controlled structure.[78] Hinds et al[79] reported that the axial conductivity of aligned CNTs is 3,520 S/m, while the in-plane conductivity is two orders of magnitude less than that, at 32 S/m. Lower in-plane conductivity is expected because of the loose contact among the neighboring CNTs. The electrical conductivity of randomly laid CNT films is usually lower than that of aligned CNTs, which is resulted from the contact resistance between inter-tube junctions. Under this condition, electron transport is *via* the hopping mechanism.[80] A pristine CNT film prepared from vacuum filtration has a conductivity of

1700 S/m. The corresponding CNT-Nafion composite films have a slightly lower conductivity of 1580 S/m with Nafion content up to 33 wt.%.[62] Chemical functionalization of CNTs can also lead to a decrease on conductivity, which is due to disruption of the extended π-π network of the pure sp2-hybridized CNT by introducing sp3-hybridized carbon atoms.[81] This change in electronic structure has a negative effect on the electrical conductivity of derivatized nanotubes, perturbing electron transportation between π-π type bands. Fluoropolymer functionalized MWCNT film showed a conductivity of 132 S/m.[63] The conductivity of the MWCNT-ODA films exhibits a nominal decrease from pristine MWCNT film to 14 wt. % ODA content in MWCNT. For pristine MWCNT films, the conductivity was measured to be 1130 S/m. However, an introduction of 14 wt. % ODA causes a 19% drop in conductivity to 910 S/m. The main reason for the conductivity reduction is the presence of defects on MWCNTs resulted from chemical functionalization and the barrier effect of the chemically grafted ODA.

In this work, it is demonstrated that MWCNTs can be directly functionalized with ODA to prepare highly conductive, superhydrophobic thin films. Additionally, the amination procedure used does not require the use of aggressive chemicals. This is in stark contrast to traditional routes for activation of MWCNTs, such as oxidative treatment with strong mineral acids that could disrupt the π-π structure and decrease electrical conductivity of MWCNTs. The vacuum filtration method used is also found to be a straightforward way to prepare MWCNT thin films. In this process, the MWCNTs become randomly distributed on the filter paper with micro- and nano-scale surface

roughness characteristics. The long alkane chain in ODA reduces the surface energy of MWCNTs. This approach resulted in MWCNT thin films with a controlled surface roughness along with an effective mild amination functionalization. The combination of controlled surface roughness of MWCNT thin films and effective, mild amination functionalization with hydrophobic groups of ODA lead to the formation of conductive and superhydrophobic properties of MWCNT thin films. The combined superhydrophobicity and high electrical conductivity of MWCNT-ODA thin films may give rise to many potential electrical component applications, such as electrodes for fuel cells and solar panels.[82, 83]

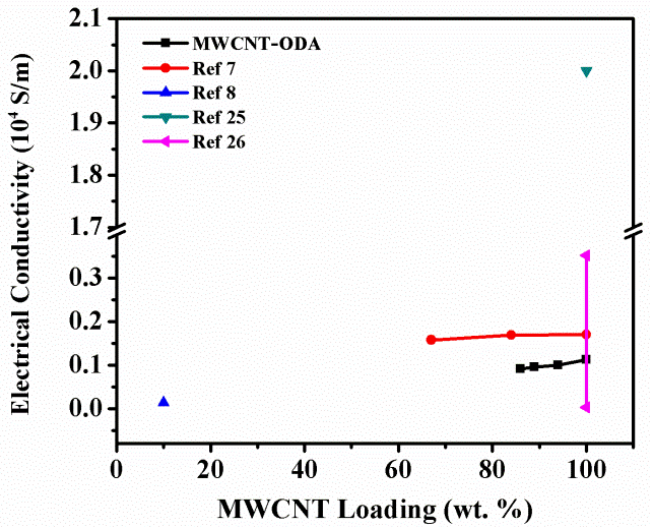

Figure 20. Comparison of electrical conductivity of MWCNT thin films.

3.4 Conclusions

A new method to functionalize MWCNTs directly with ODA in solution has been successfully developed. The long alkane chain of ODA was bonded to the MWCNTs through reaction at the defect sites on the MWCNT surfaces. The MWCNT-

ODA can form thin films exhibiting superhydrophobicity and high electrical conductivity properties by vacuum filtration. The surface wettability of the MWCNT-ODA films can also be controlled by the amount of ODA functionalized. The CAs increases from 31^{o} for the pristine MWCNT film to 165^{o} for the MWCNT-ODA-14 wt.% film. The electrical conductivity measurements confirm that the functionalization reaction is mild and relatively nondestructive to the electronic structure of MWCNT surfaces. The combination of superhydrophobicity and high electrical conductivity measured in the MWCNT-ODA films is highly desirable. The results of this work may contribute to the development of a wide range of applications, including display technologies, solar cells, new electrode material and flexible electronic devices.

CHAPTER IV

FACILE DECORATION OF AU NANOPARTICLES ON REDUCED GRAPHENE OXIDE SURFACES VIA A ONE-STEP CHEMICAL FUNCTIONALIZATION APPROACH*

4.1 Introduction

Surface-enhanced Raman spectroscopy (SERS) has been developed since the 1970s to enable the detection of single-molecules and to provide special chemical fingerprint information.[84-86] Million-fold enhancement in Raman scattering could be obtained for molecules that are adsorbed on rough metal surfaces or colloidal metal nanostructures.[87] These metal regions possess greatly enhanced local electromagnetic fields due to the localized surface plasmon resonance effect. The localized electromagnetic field develops a dominant contribution of SERS enhancement, which is referred to as electromagnetic enhancement (EM).[88] Current efforts towards fabrication of SERS substrate are mainly based on nano-assembly or nano-tailoring of metal nanostructures.[87,89] The wide size range and effective Raman scattering enhancement make colloidal Au nanoparticles (AuNPs) an excellent building block for SERS-active substrates. However, the main challenge for building a SERS-active substrate is the difficulty of assembling AuNPs onto macroscopic surfaces with well-defined and uniform nanoscale architecture.[87, 88, 90]

* Reproduced from Ref. 51 with permission from the Royal Society of Chemistry.

Recent progress in the area of graphene/metal nanohybrid materials has enabled the usage of graphene as a substrate to manipulate the structure and property of colloidal AuNPs.[6, 18] Additionally, it has been reported that graphene-based SERS have advantages over normal SERS, such as sharper vibrational signals, free from various metal-molecule interaction induced noises, and comparable enhancement factors,[5] which make graphene attractive for SERS applications.[91] Currently, different methods have been developed for fabricating graphene/colloidal AuNPs composites. Examples include *in-situ* growth on graphene oxide (GO) surface,[92] photochemical photo-assisted synthesis,[93] and direct mixing method.[94] However, in order to immobilize AuNPs on the graphene surface with well-defined architecture, advanced chemical treatment is necessary because the pristine lattice structure of graphene has no suitable chemical functionality to assemble and anchor AuNPs.

The purpose of this work is to achieve well-defined AuNPs on organosilane-functionalized graphene through self-assembly. Controlled macroscopic surfaces with uniform roughness can be prepared by self-assembly.[90] Our protocol for the preparation of graphene/Au nanomposites involves two steps: 1) chemical functionalization of GO by silane coupling agent and 2) anchoring of AuNPs with amine functional groups. The first step involves the utilization of silane coupling agent, N^1-(3-trimethoxysilylpropyl) diethylenetriamine (TSPD), forming covalent bonding on the GO surface *via* hydrolysis. At the interface between graphene and silane groups, only one of the silane groups will form chemical bonding with –OH on GO surface. The other two remaining silanol groups in each TSPD are present in condensed or free form.[95] As a result, TSPD can

readily form a monomolecular layer on the graphene surface. In the meantime, the presence of amine groups in TSPD can further reduce GO and re-disperse RGO in organic solvents after the reaction.[96] In the second step, TSPD functionalized and reduced GO (RGO-TSPD) can be mixed with colloidal AuNPs to allow for self-assembly of AuNPs on graphene substrate through the covalent Au-N bonding.[97] Implication of the RGO-TSPD/AuNPs composites in SERS is discussed.

4.2 Materials and methods

4.2.1 Materials

Graphite (SP-1, average particle sizes of 30 μm) was obtained from Bay Carbon Inc, USA. N^1-(3-trimethoxysilylpropyl) diethylenetriamine (TSPD), hydrazine, Rhodamine 6G and all solvents utilized were purchased from Sigma-Aldrich and used as received.

4.2.2 Synthesis of RGO-TSPD

GO was synthesized by the Hummers method.[21] Graphite powder (0.5 g) was first treated with a solution containing concentrated H_2SO_4 (50 mL) and $NaNO_3$ (0.5 g) below 5^oC. $KMnO_4$ (3 g) was added gradually, and the mixture was stirred continuously for 2h. Then, the mixture temperature was increased to 35^oC and stirred for another 2 h. Afterwards, the mixture was diluted with DI water (23 mL) and stirred for 15 min. Additional DI water (71 mL) and 30% H_2O_2 (10 mL) were added to the mixture, which changed the mixture color into brilliant yellow. Finally, the mixture was washed with water several times and HCl once to remove metallic ions. GO (100 mg) was dispersed in ethanol, followed by dropwise addition of TSPD (1.4 mL, 5.4 mM). The mixture was

stirred at 90^{o}C for 24 h. The resulting suspension was washed thoroughly with ethanol and acetone to remove unreacted silylating agents. The final samples were dried at 60^{o}C in a vacuum oven for 24 h.

4.2.3 Synthesis of graphene/Au nanocomposites

The synthesis of AuNPs was carried out following a similar procedure reported in the literature.[98] In short, 100 mL of 1 mM $HAuCl_4$ was refluxed and vigorously stirred. Rapid addition of 10 mL of 38.8 mM sodium citrate to the boiling solution resulted in a color change from pale yellow to wine red. The mixture was stirred for 10 min, and then the heat source was removed. Stirring was continued for an additional 15 min until the solution reached room temperature. Then, 10 mL of AuNPs solution was mixed with 0.5 mL RGO-TSPD solution at room temperature, and then the mixture was incubated at 35^{o}C for 20 h. The final RGO-TSPD/AuNPs products were collected by centrifugation and washed with DI water twice.

4.2.4 Characterization

Fourier transform infrared spectroscopy-attenuated total reflectance (FTIR-ATR) spectra of the samples were acquired using Nicolet 380 (Thermo Fisher Scientific) in conjunction with ATR accessory (AVATAR OMNI Sampler, Germanium crystal) under ambient condition. X-ray photoelectron spectroscopy (XPS) data were obtained with a Kratos Axis Ultra using a non-monochromatic MgKa photon source (1486 eV) for measurements. Data were fitted using XPSPEAK 4.1 by applying a Linear-type background correction. For thermal gravitational analysis (TGA), 2~3 mg solid samples were used. The tests were performed using a TGA (Q500, TA Instruments) by ramping

the sample temperature from 30 °C to 900 °C at a ramping rate of 20 °C/min in air. The section height of RGO-TSPD was identified by an atomic force microscope (AFM, Digital Instruments Nanoscope AFM/STM). TEM was performed using a JEOL 2010 high-resolution transmission electron microscope operated at 200 kV. Raman spectra were obtained using a Horiba Jobin-Yvon LabRam IR system with a 632.8 nm He-Ne laser line. All spectra were acquired under the same conditions.

4.3 Results and discussion

4.3.1 Characterization of RGO-TSPD

The preparation of RGO-TSPD is shown schematically in **Figure 21**. TSPD has one organic substituent and three hydrolyzable substituents ($-OCH_3$). Hydroxyl groups on the GO surface provide active sites for the attachment of TSPD. Normally, the reaction between organosilane and GO includes three steps:[95] 1) hydrolysis of the three labile groups, 2) condensation to oligomers, and 3) reaction between the oligomers and the OH groups on GO. Although the above three steps were described sequentially, they can take place simultaneously after the initial hydrolysis. At the interface between GO and silane groups, only one silanol group from each organosilane molecule bonds to GO surface. The two remaining silanol groups exist in either condensed or free form. It is interesting to note that π-π conjugation network of GO was partially restored due to the amine functionality of TSPD during the reaction. The brown-colored dispersion turned black immediately after the addition of TSPD, similar to the hydrazine reduced GO (HRGO).[96] After the reaction, RGO-TSPD sheets can be easily re-dispersed in various organic solvents with the assistance of sonication.

The silylation reaction mechanism and reduction process between GO and TSPD can be determined by analyzing the core-level Binding Energy (BE) obtained from XPS (**Figure 22**). It has been reported that GO can be reduced in aqueous solution at 95 ^{o}C.[99] To exclude the possible thermal effect, a control sample heated at 90 ^{o}C for 24 h without TSPD was also prepared. The C 1s XPS spectrum of the control sample (**Figure 22**a) still shows a considerable degree of oxidation with three main components that are attributed to different oxidation states of carbon atoms: the non-oxygenated C (284.8 eV), the C in C-O bonds (286.2 eV) and the C in carbonyl groups (287.8 eV).[96] The decomposition of the XPS spectrum obtained from the control sample shows a low C/O ratio (2.3), which is similar to that of GO (1.9). This suggests that the reduction of GO due to the 90°C thermal treatment alone is insignificant. However, the C/O ratio in the RGO-TSPD (**Figure 22**c) increases significantly after the silylating reaction, and most of the epoxide and carboxyl groups have been successfully removed. The disappearance of 1728 cm^{-1} band (C=O asymmetric stretching) in the FTIR spectrum of RGO-TSPD also implied the partial graphene reduction after the silane reaction. Compared with HRGO (**Figure 22**b), RGO-TSPD has a higher content of C-O groups because of the presence of covalent Si-O-C bonds between TSPD and graphene sheets. Furthermore, significant amounts of N 1s and Si 2p from RGO-TSPD were detected, which implies that TSPD has been successfully functionalized on graphene surface.

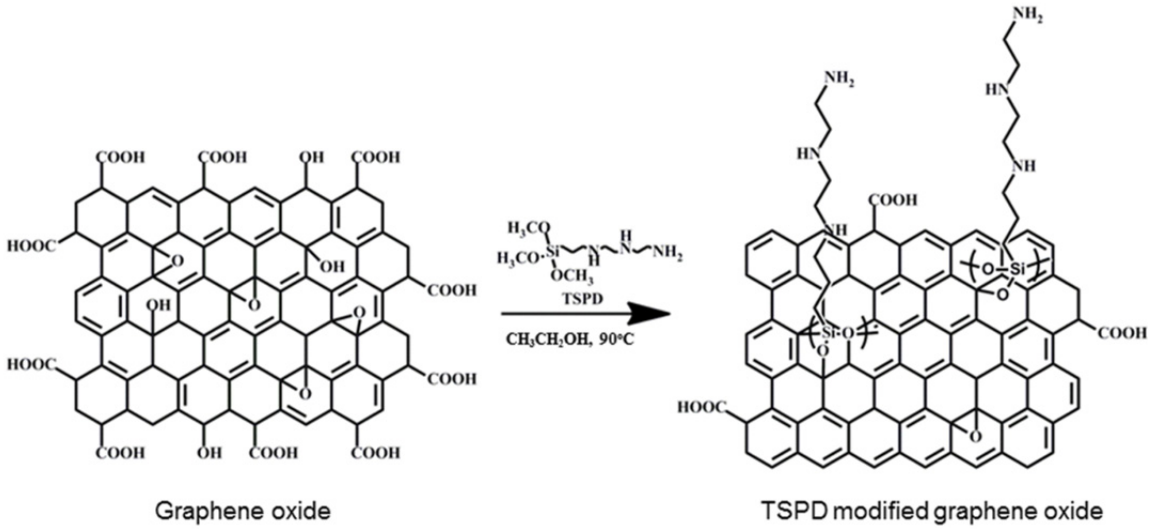

Figure 21. Schematic illustration for the preparation of RGO-TSPD.

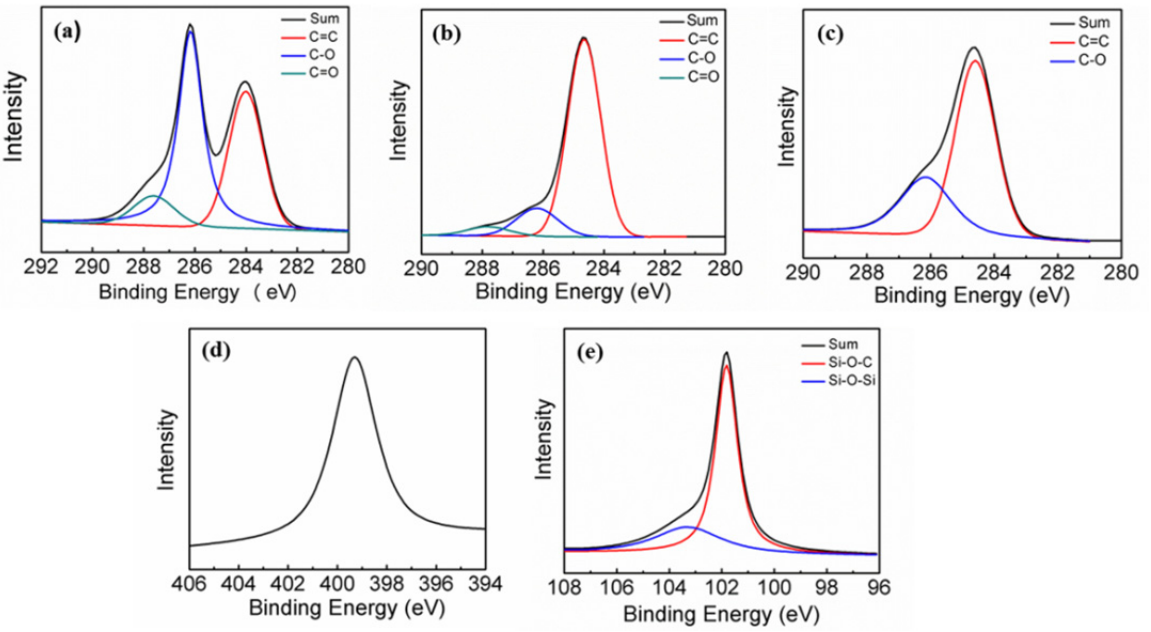

Figure 22. XPS spectra of (a) C 1s of GO under heat treatment, (b) C 1s of HRGO, (c) C 1s of RGO-TSPD, and (d) N 1s of RGO-TSPD, (e) Si 2p of RGO-TSPD.

Since TSPD contains bifunctional groups, grafting to the GO sheets might occur through either (a) amination between the amine groups of the silane and the carbonyl or

carboxyl functionalities from GO or (b) silylation between trialkoxy groups and hydroxyl groups. The first possibility seems less likely because the low reactivity of amination reaction diminishes the chances for the C=O and COOH groups to react.[100] Indeed, the XPS N 1s and Si 2p spectra of RGO-TSPD support the claim. The XPS N 1s spectrum shows one single peak at 399.9 eV (**Figure 22**d), which is assigned to aliphatic amine (-NH_2 or –NH).[101] The band of Si 2p spectrum of RGO-TSPD (**Figure 22**e) was fitted into two peaks at 101.8 eV and 103.3 eV. The lower BE peak was assigned to the bond of silicon with oxygen groups originating from RGO sheets (Si-O-C). The higher BE peak is attributed to the siloxane (Si-O-Si) resulting from the partial hydrolysis of the TSPD molecules.[102-104] Based on the XPS data of RGO-TSPD, the atomic percentage of Si is estimated to be 5.64%, and that of N is 14.35%. The degree of functionalization is then estimated to be ~1 functional group per 29 carbons.

The significant structural changes observed during silylating treatment are also reflected in the UV-Vis absorption spectra. The absorption peak of GO at 227 nm corresponds to π-π^* transitions of aromatic C=C bonds.[105] After GO reduction, the absorption peak red-shifts to a higher wavenumber because of the restoration of the π conjugation network. As shown in **Figure 23**, the absorption peaks of HRGO and RGO-TSPD have shifted to 267 nm and 262 nm, respectively. The insets show that the GO solution color changed from yellowish brown to black after silylation treatment, which provides visual evidence of the partial restoration of the conjugation network in the RGO-TSPD sheets. Unlike HRGO, the RGO-TSPD can be readily dispersed in organic solvents, such as acetone, ethanol, and dimethylformamide (DMF). Results from both

XPS and UV-Vis spectrum indicate that the reduction process has significantly restored the π-π graphene network. Although the detailed mechanism responsible for the above process is still unclear, it is well known that GO undergoes deoxygenation in alkaline solution.[99] Furthermore, the deoxygenation reaction of GO is pH dependent, i.e., a higher pH leads to a faster reaction. For each TSPD molecule, it contains one primary amine and two secondary amines, with Kb values of ~4.7×10^{-4} M and 5.4×10^{-4} M, respectively. Thus, the reaction between GO and TSPD is under alkaline condition. For reducing agents like hydrazine, it is an alkali with a Kb value of 1.3×10^{-6} M. It has been reported that hydrazine causes ring opening of epoxide groups to form hydrazine alcohol,[96] followed by the formation of an aminoaziridine group through the removal of one water molecule. Finally, the double bond on the graphene plane was restored with thermal elimination of diimide. In our work, a similar reduction process as hydrazine reduction is expected to occur between TSPD and GO. The exact reduction mechanism, however, still awaits further investigation.

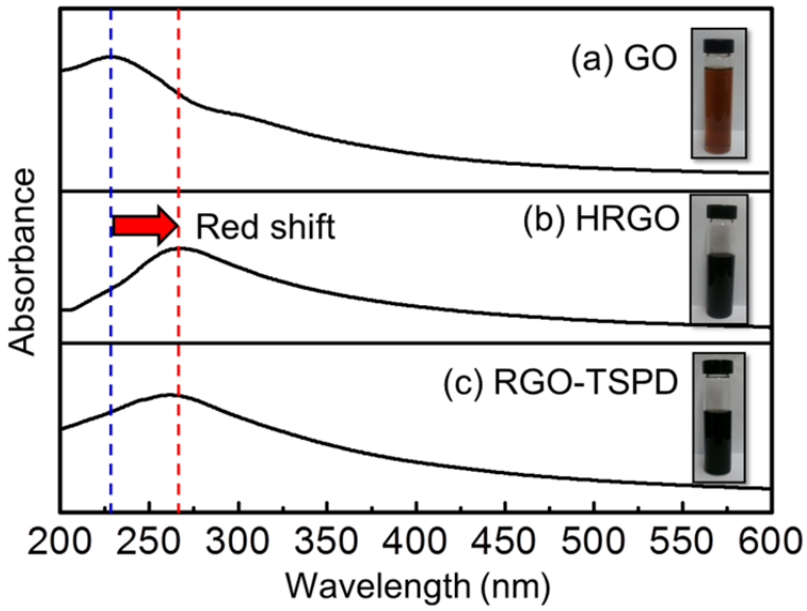

Figure 23. UV-Vis absorption spectra of (a) GO, (b) HRGO, and (c) RGO-TSPD (the absorption of TSPD has been subtracted in (c)).

To obtain SERS-active substrate, immobilized AuNPs are required to locate solely on the surface of RGO-TSPD, and not embedded within the organosliane layer. In this fashion, a monomolecular layer of TSPD on the graphene surface is necessary. Direct evidence concerning the molecular morphology of RGO-TSPD sheets comes from AFM studies. Two representative images with different magnifications are shown in Error! Reference source not found.. RGO-TSPD sheets exhibit folded and wrinkled morphology with an average lateral dimension of 1 μm. The thicknesses range from 2.4 nm to 2.8 nm. According to literature,[106] the TSPD monolayer has a thickness of 2.1~3.0 nm from AFM measurement, and an idealistic graphene sheet has a thickness of 0.34 nm.[6] Thus, the theoretical thickness of RGO-TSPD should be 2.4~3.3 nm, which is consistent with the AFM findings. This leads to the conclusion that TSPD form a

monomolecular layer on the graphene surface with reasonably uniform coverage, which serves as a facile way to obtain a two-dimensional monolayer of AuNPs.

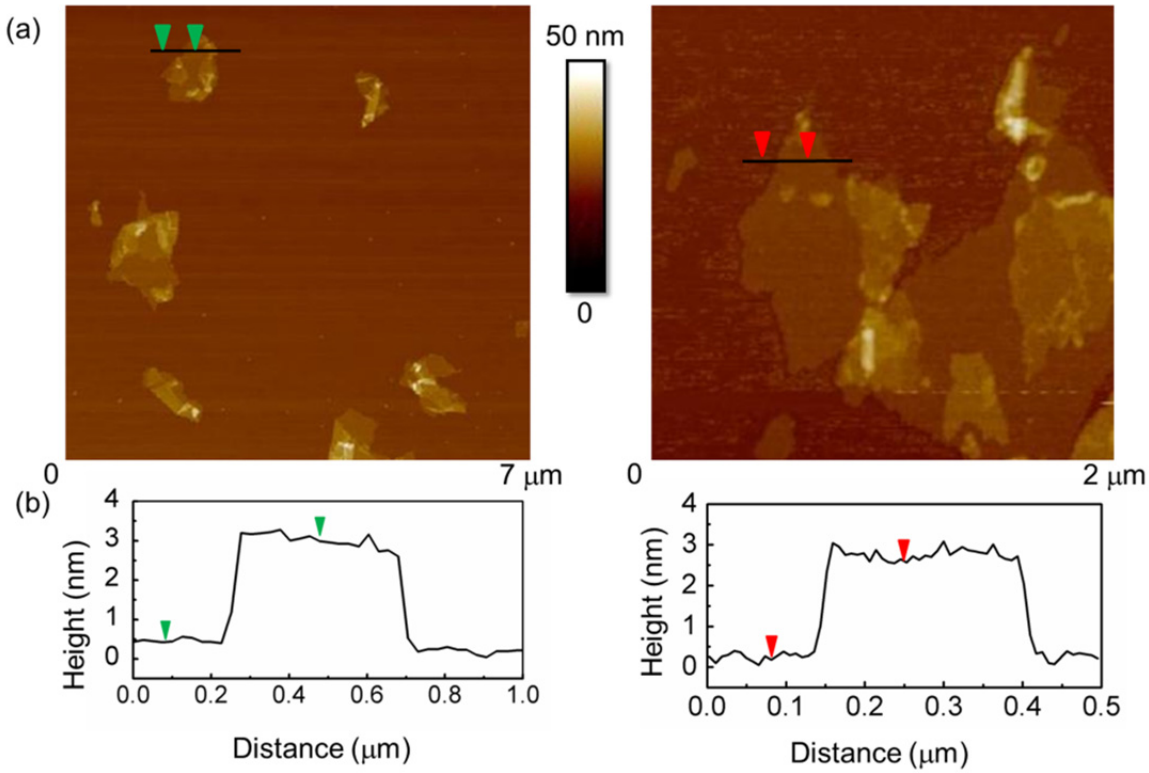

Figure 24. (a) AFM image of RGO-TSPD coated onto a freshly cleaved mica surface showing single or double layers RGO-TSPD sheets, and (b) height profiles of RGO-TSPD.

4.3.2 Characterization of graphene/Au nanocomposites

The schematic presented in **Figure 25** illustrates how the AuNPs self-assemble on RGO-TSPD surface to form a 2-D monolayer. As discussed above, silane molecules form a stable self-assembled monolayer on the substrate through covalent bonding between the GO surface and silane molecules. Terminated amine groups point outwards away from the RGO-TSPD surface and serve as anchoring sites for AuNPs. The

advantage of the colloidal self-assembly approach is that covalent bonding between nanoparticles with the substrate reduces the surface mobility of the nanoparticles and prevents spontaneous coalescence of nanoparticles on the surface. Thus, the original nanoparticle size is maintained, and the surface has uniform and nanoscale roughness, which is particularly important in SERS.[90]

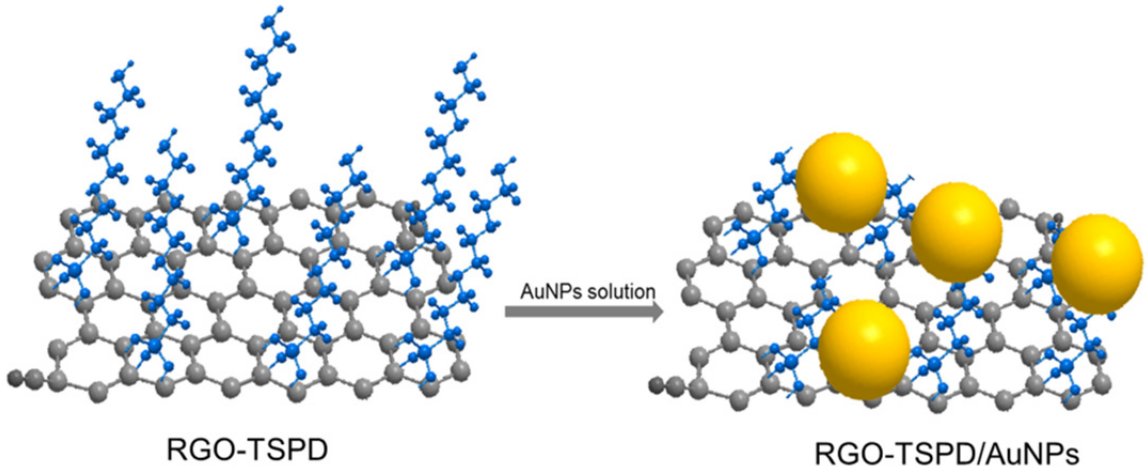

Figure 25. Schematic description of AuNPs anchoring on graphene sheet through silane molecules (not drawn to scale): graphene sheet (grey), TSPD molecule (blue), AuNP (golden).

Immersion time after mixing is an important factor in determining the nanoparticle coverage on RGO-TSPD surfaces. It has been reported that the kinetics of AuNPs binding to organosilane-coated substrates contains two main steps: 1) in an early stage, the particle coverage is $t^{1/2}$ dependence and AuNPs coverage increases with time and 2) at a later stage, AuNPs coverage on the substrate saturate because of the repulsive interaction between them.[107] To obtain the maximum coverage of AuNPs on RGO-TSPD surface without aggregate formation, the AuNPs were allowed to interact with the

RGO-TSPD nanosheets for 20 h of incubation at 35^{o}C. A control experiment was also carried out by incubating AuNPs with GO without TSPD functionalization. The morphologies of the resulting AuNPs on GO, HRGO, and RGO-TSPD were characterized by TEM, as shown in **Figure 26**. For AuNPs on GO, only a few aggregated AuNPs were attached on GO nanosheets due to the weak electrostatic interaction between AuNPs and the oxygen groups on GO sheets.[92] For HRGO, most of the oxygen groups were removed after reduction, and they formed aggregates during the preparation procedure.[96] Thus, it is unlikely for AuNPs to be uniformly attached on the graphene sheets in the HRGO agglomerate by direct mixing. Indeed, as shown in **Figure 26**b, only aggregated graphite and AuNPs are observed. On the other hand, as shown in **Figure 26**c and d, it is evident that RGO-TSPD surfaces are uniformly covered with AuNPs. Close examination of these images confirms several advantages of the self-assembly of colloidal AuNPs approach: 1) covalent interaction between the substrate is necessary to obtain uniform particle distribution, 2) AuNPs form a 2D monolayer on RGO-TSPD, and 3) AuNPs are closely packed on RGO-TSPD surface without aggregation, having an average inter-particle distance of 15 nm.

To further characterize the AuNPs monolayer, the particle number density on the RGO-TSPD sheets was determined. Depending on the location on the RGO-TSPD sheet, the particle number densities vary from 1,250 to 5,000 particles/μm^2. The average particle number density is about 3,000 particles/μm^2 with AuNPs coverage of about 24%. Since AuNPs monolayer coverage is limited by inter-particle repulsion, most of the AuNPs appear to be close-packed in 2D having an inter-particle distance of 15 nm,

without forming 3D clusters. It is noted that AuNPs have a saturation coverage of ~30% on GO surface derivatized with (3-mercaptopropyl)-trimethoxysilane.[107] The thiol linkage apparently provides a unique pathway toward imparting stable organic functionality to AuNPs with strong covalent interaction.[108] In contrast, the interaction between AuNPs and amine in TSPD is through weak covalent Au-N bonding,[97, 108] which is the main reason for the lower coverage of AuNPs in RGO-TSPD than the case with thiol functionality. As discussed above, there are two stages for AuNPs binding to organosilane-coated substrates: 1) initial AuNPs deposition, which increases with time; and 2) late saturated AuNPs coverage due to repulsive interaction among AuNPs. During the initial stage, the binding interaction between particles and substrate determines the binding rate. And, in late step, the inter-particle repulsive forces are the dominant factor in controlling the inter-particle spacing of AuNPs during self-assembly process.

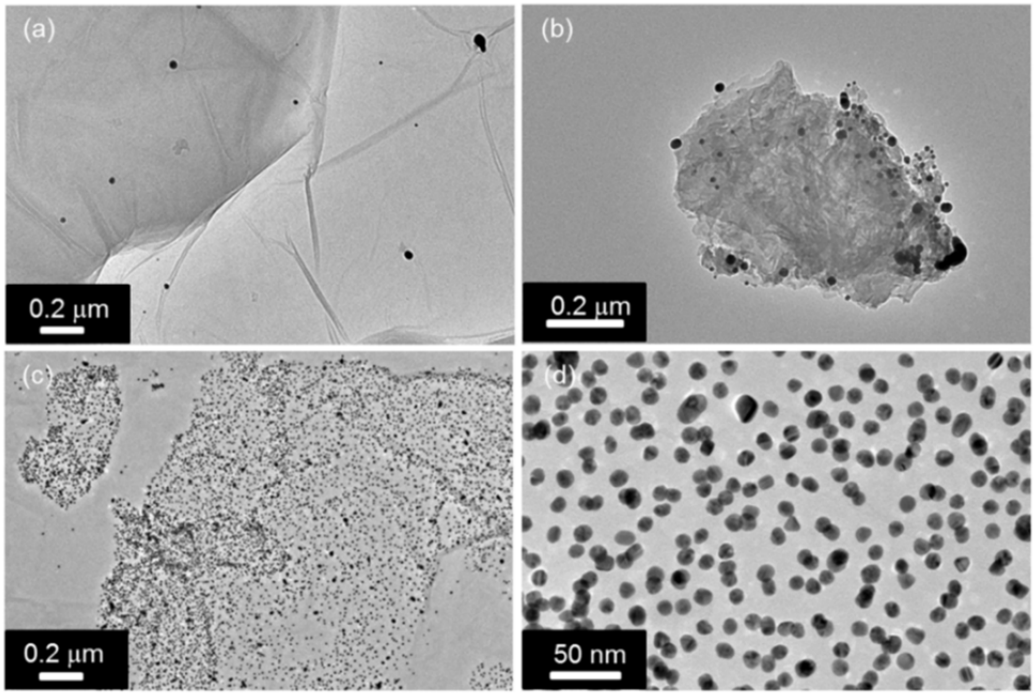

Figure 26. TEM images of (a) GO/AuNPs, (b) HRGO/AuNPs, and RGO-TSPD/AuNPs in (c) low magnification and (d) high magnification.

Figure 27 shows UV-Vis absorbance spectra of isolated AuNPs solution and RGO-TSPD/AuNPs composite. The pre-synthesized AuNPs with a diameter of ~10 nm have a surface plasmon resonance peak at around 520 nm in the visible spectrum.[90] AuNPs are well known for their strong interactions with visible light through the resonant excitations of the collective oscillations of the conduction electrons within the particles.[109] The surface plasma resonance energy of AuNPs depends on their size, shape, and surrounding environment.[110] When clusters of AuNPs are placed in close proximity to one another, the coupling effect between particles becomes dominant, and the surface plasma resonance wavelength of two coupled particles shift to a higher wavelength.[111, 112] The intensity and maximum wavelength, λ_{max}, of the absorbance peak

scale with the extent of aggregation, with large aggregates exhibiting increased extinction and red-shifted peaks.[90] In the presence of RGO-TSPD, the surface plasmon resonance peak of AuNPs becomes much broader and redshifts to 532 nm due to the coupling effect.[111, 112] The coupling effect between surface plasmon of neighboring AuNPs leads to energy shift and energy confinement between particles, which is responsible for the pronounced SERS activity of collections of colloidal AuNPs.

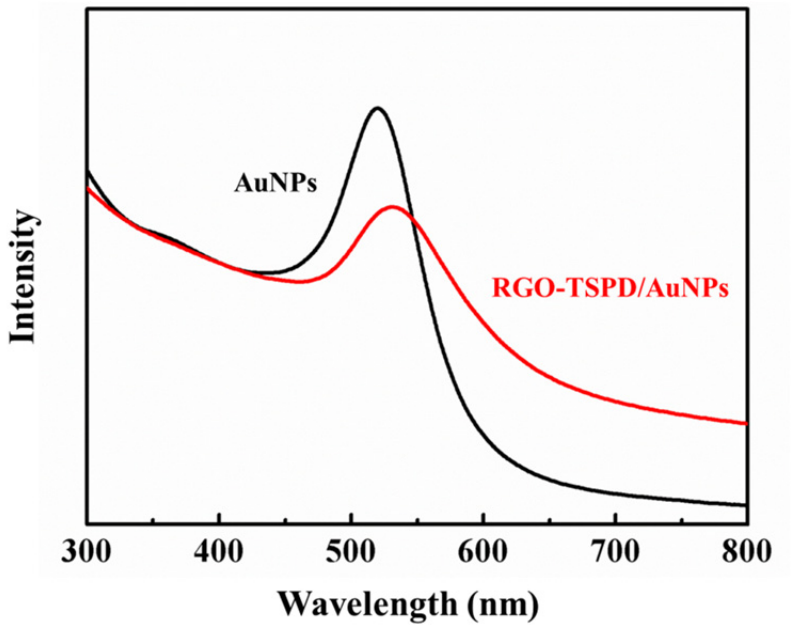

Figure 27. UV-Vis absorption spectra of Au nanoparticles and RGO-TSPD/AuNPs.

The SERS effect is based on two main mechanisms: electromagnetic and chemical mechanisms. The first one involves the excitation of surface plasmons on the metal structure, which is the dominant contribution to SERS enhancement with an enhancement of 10^8 or more.[113] The chemical enhancement involves the formation of a charge-transfer complex between the substrate and molecule with a minor enhancement

factor of 10 to 10^2.[114] AuNPs are one of the most popular electromagnetic enhancers. The electron transfer between the graphene and single molecule leads to a chemical-based enhancement. Furthermore, two-dimensional graphene could offer an atomically smooth surface for controllable molecular arrangements as well as well-defined molecular interactions. Thus, the combination of graphene with AuNPs monolayer is anticipated to be one of the most powerful microanalytical techniques with single-molecule capabilities and chemical specificity.

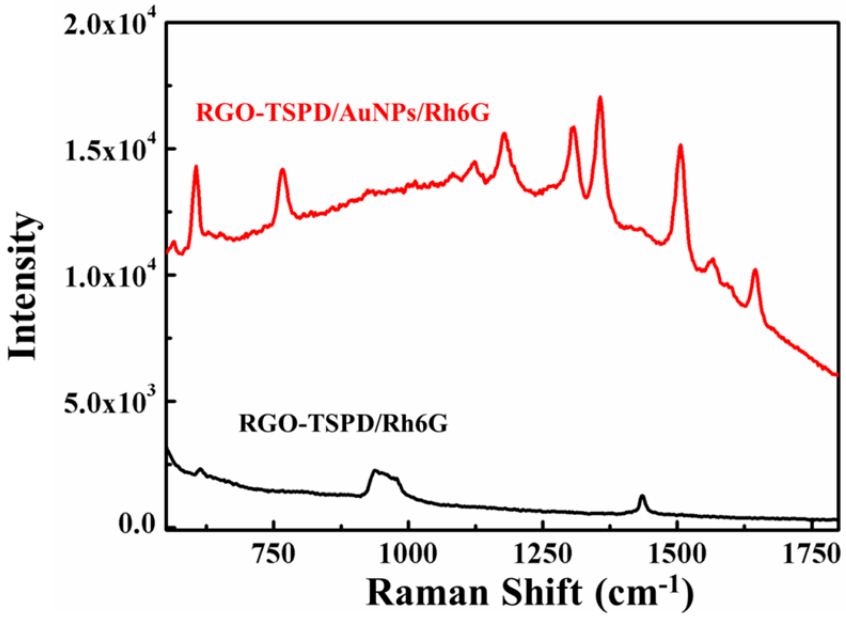

Figure 28. Raman spectra of RGO-TSPD/Au and RGO-TSPD/Au at excitation wavelength of 632.8 nm (*marks the Raman signal of SiO_2/Si substrate).

Figure 28 shows the Raman spectra of Rhodamine 6G (Rh6G) on the surface of RGO-TSPD and RGO-TSPD/AuNPs. These samples were prepared by immersing the substrates into Rh6G methanol solution with a concentration of 2×10^{-5} M. It can be seen that the RGO-TSPD/AuNPs substrate present significantly sharper and stronger signals.

The main Raman peaks of Rh6G are observed at 564, 605, 766, 1123, 1179, 1306, 1357, 1506, 1573, 1599, 1645 cm^{-1} (±1 cm^{-1}) (**Table 2**). The peak around 1567 cm^{-1} is attributed to the G band of graphene.[88] Compared with the spectra of Rh6G in solution, the observed spectra features of Rh6G on RGO-TSPD/AuNPs substrate show some shift, most likely from the interaction between Rh6G and the RGO-TSPD/AuNPs substrate.[115] Taking the intensity of 1357cm^{-1} at RGO-TSPD/Rh6G spectra as a reference, the RGO-TSPD/AuNPs/Rh6G spectrum was enhanced by a factor of 29. This indicates that the solution-based assembly protocol presented in this study results in well-defined nanoscale AuNPs monolayer on RGO-TSPD surface.

Table 2. Band positions and their assignments from literature and RGO-TSPD/Au spectra of Rh6G.

Rh6G in solution	RGO-TSPD/AuNPs	Tentative assignments
614	605	Xanthene ring deformation
776	766	Xanthene ring deformation
1187	1179	C-H deformation
1312	1306	
1365	1357	Xanthene ring stretching
1509	1506	Xanthene ring stretching
-	1567	G band of graphene
1575	1573	Xanthene ring stretching
1600	1599	Xanthene ring stretching

4.4 Conclusions

We have demonstrated in this work that GO can be easily reduced and functionalized by TSPD. The present findings offer an efficient approach to reduce and modify GO in one step, without causing aggregation or restacking of graphene sheets. The resulting RGO-TSPD sheets serve as an ideal template for AuNPs self-assembly into a monolayer with controlled macroscopic, microscopic and nanoscopic surface characteristics. The coupling effect between surface plasmon of neighboring AuNPs leads to energy shift and energy confinement between AuNPs, which provide potential applications in SERS. The RGO-TSPD/AuNPs-based substrate has many attractive attributes over the previously reported graphene/Au materials, such as uniform particle size and well-defined AuNPs monolayer architecture. Additionally, the benefit of graphene sheets, such as its 2D structure, biocompatibility, and excellent electrical properties, suggests potential applications of these materials in the fields of catalysis, optics, solar cells, and nanobiotechnology.

CHAPTER V

SELF-ASSEMBLY OF AU NANOPARTICLES ON GRAPHENE SHEETS WITH CONTROLLED GRAFT DENSITIES AND HIGH REUSABILITY AS CATALYSTS*

5.1 Introduction

Gold nanoparticles (Au NPs) have been extensively studied in catalyst for petroleum processing, energy conversion, and pollutant removal.[48-50] The use of NPs results in large contact areas between the active material of the catalyst and the surrounding environment.[52] This ensures that the Au NPs are used effectively as a catalytic material. One of the challenges associated with the use of Au NPs as catalysts is that the high surface area reduces the colloidal stability, drives the aggregation of the NPs, and lowers the catalytic activity.[53] Another challenge is post-reaction separation and the reusability of the tiny particles.[54] To overcome these challenges, heterogeneous catalysts based on supported Au NPs have been developed to improve the colloidal stability. Various materials have been reported to support Au NPs for the heterogeneous catalysis. These materials include polymers, carbon materials, silica, and metal oxides.[54, 116-123] Although these methods have realized engineered local environments to stabilize Au NPs, they lack the control over the grafting density of Au NPs.[124] Controlling the particle density is crucial to understand reaction kinetics and to control reaction rate, which is one of the scientific challenges related to the catalytic application of Au NPs.

* Reproduced from Ref. 47 with permission from the Royal Society of Chemistry.

Graphene, a two-dimensional sheet consisting of sp^2 hybridized carbon atoms, has emerged as one of the most promising support materials for Au NPs due to its high surface area and chemical stability.[6, 17, 20, 125, 126] One of the methods to prepare graphene sheets is the chemical exfoliation of graphite in aqueous medium, which produces oxygen functionalized graphene sheets -graphene oxide (GO). The hybridization of GO with the Au NPs synergistically enhances their functionalities and expands their catalytic applications.[127, 128] Efforts have been made to synthesize GO/Au nanocomposites by mixing and *in-situ* approaches.[40, 92, 129-131] Goncalves *et al.*[92] reported a method to prepare GO/Au composites by directly mixing Au(III) ions with GO in water, and the oxygen groups present at GO surface serve as nucleation sites for Au NPs. However, the resulting GO/Au composites showed a low density of Au NPs on the graphene sheet, *i.e.* approximately 8%. In order to improve the grafting density, organic spacers, *e.g.* octadecylamine,[132] protein,[40] and 1-pyrene butyric acid,[124] were used to anchor Au NPs on graphene sheets. An additional spacer was reported in our previous work,[51] where we used a silylating agent (N^1-(3-trimethoxysilylpropyl) diethylenetriamine) to anchor Au NPs on GO surface. The silylating agent forms covalent bonding with GO, and simultaneously serves as a reductant to reduce GO. This method provides effective anchoring sites for Au NPs, leading to a density of 24%.

To fully exploit the use of GO sheets as a support for Au NPs, it is desirable to decorate the GO surface with appropriate functional groups that generate anchoring sites for Au NPs with controlled density. The present work intends to extend the self-assembly approach in our previous work to develop GO/Au composites with tunable

particle densities.[51] One of the consequences of using the self-assembly method is large areas of densely packed particles on a support. This becomes prominent in expanding the GO-Au composite family and exploring additional applications of the composites. In the present work, GO is chemically functionalized by three different silane coupling agents, which vary at their end groups, *i.e.* mono-, bi- and tri-amine. These different functional groups enable manipulating the grafting density of Au NPs and tailoring their catalytic applications. Various spectroscopies and microscopies are used to characterize the resulting composites and study the catalytic activities in the reduction reaction of 4-nitrophenol (4-NPh) to 4-aminophenol (4-APh).

5.2 Materials and methods

5.2.1 Materials

Graphite (SP-1 graphite, average particle sizes of 45 μm) was obtained from Bay Carbon Inc, USA. The following reagents were purchased from Sigma-Aldrich and were used as received: (3-Aminopropyl) trimethoxysilane (1N), N-[3-(Trimethoxysilyl) propyl] ethylenediamine (2N), N1-(3-Trimethoxysilylpropyl) diethylene triamine (3N), hydrazine, $NaNO_3$, $KMnO_4$, H_2SO_4, and H_2O_2.

5.2.2 Synthesis of GO and organosilane-functionalized GO

GO was synthesized by the Hummers method.[21] Graphite powder (0.5 g) was firstly treated with a solution containing concentrated H_2SO_4 (50 mL) and $NaNO_3$ (0.5 g) below 5 ^oC. $KMnO_4$ (3 g) was added gradually, and the mixture was stirred continuously for 2 h. The mixture temperature was increased to 35 °C and stirred for another 2 h. The mixture was diluted with deionized (DI) water (23 mL) and stirred for 15 min.

Additional DI water (71 mL) and 30% H_2O_2 (10 mL) were added to the mixture, which changed the mixture color to brilliant yellow. Finally, the mixture was washed with water several times and HCl once to remove metallic ions.

GO (100 mg) was dispersed in ethanol, followed by addition of organosilane (5.4 mM). The mixture was stirred at 90 °C for 24 h. The resulting suspension was washed thoroughly with ethanol and acetone to remove unreacted silylating agents. The final samples were dried at 60 °C in a vacuum oven for 24 h.

5.2.3 Preparation of GO/Au nanocomposites

The synthesis of Au NPs was carried out following a similar procedure reported in the literature.[133] $HAuCl_4$ aqueous solution (1mM, 100 mL) was refluxed and vigorously stirred. Rapid addition of sodium citrate aqueous solution (38.8 mM, 10 mL) to the boiling solution resulted in a color change from pale yellow to wine red. After stirring for 10 min, the heat source was removed. Stirring was continued for an additional 15 min till the solution reached room temperature. The synthesized Au NPs have an average particle size of 10 nm according to the measurements in TEM image. To prepare GO/Au nanocomposites, Au NP solution (20 mL) was mixed with organosilane-functionalized GO (1 mg) at room temperature and the mixture was incubated at 35 °C for 20 h. The final GO/Au composites were collected by centrifugation and washed with DI water twice.

5.2.4 Characterization

Fourier transform infrared spectroscopy-attenuated total reflectance (FTIR-ATR) spectra of the samples were acquired using Nicolet 380 (Thermo Fisher Scientific) in

conjunction with ATR accessory (AVATAR OMNI Sampler, Germanium crystal) under ambient condition. X-ray photoelectron spectroscopy (XPS) data were obtained with a Kratos Axis Ultra using a non-monochromatic MgKa photon source (1486 eV). Data were fitted using XPSPEAK 4.1 by applying a linear-type background correction. The section height of organosilane-functionalized GO was identified by an atomic force microscope (AFM, Bruker Dimension Icon AFM). Transmission electron microscopy (TEM) was performed using a JEOL 2010 high-resolution TEM operated at 200 kV. UV-Vis absorption spectra were acquired with a UV-Vis-NIR spectrophotometer (Shimadzu, UV-3600).

5.3 Results and discussion

5.3.1 Preparation of organosilane-functionalized GO

Figure 29 illustrates a one-step chemical functionalization of GO through silane agents and the self-assembly of Au NPs on the functionalized GO. Three silylating reagents with different amine groups were used to react with GO to form GO-*x*N (*x*=1, 2, and 3): (3-aminopropyl) trimethoxysilane (GO-1N), N-[3-(trimethoxysilyl) propyl] ethylenediamine (GO-2N), and N^1-(3-trimethoxysilylpropyl) diethylene triamine (GO-3N). In general, all silane coupling agents have one organic substituent and three hydrolyzable groups ($–OCH_3$). The alkoxysilane groups react with hydroxyl groups on the GO surface, followed by the formation of a monomolecular layer on the GO surface.[95] Note that the brown colored dispersion of GO turned into black immediately after the addition of silane agents, which is similar to the phenomenon of the hydrazine

reduced GO. It suggests that the π-π conjugation network of GO was partially restored due to the amine functionality of silane agents during the reaction.

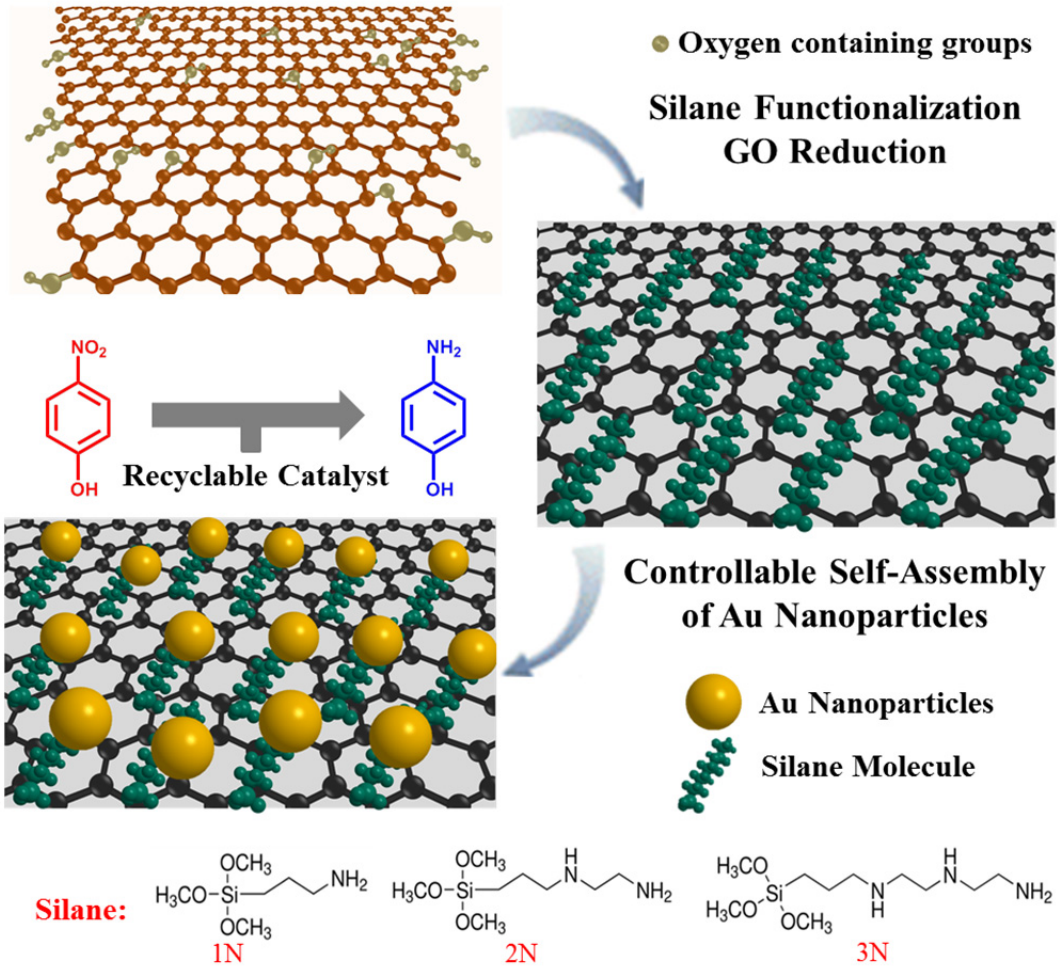

Figure 29. Schematic illustration of the preparation of effective catalysts based on Au nanoparticles and chemically functionalized GO.

The reaction between GO and silane can be confirmed by analyzing the core-level Binding Energy (BE) obtained from XPS (**Figure 30**). The XPS spectrum of C 1s on GO (**Figure 30**a) shows three main components, which correspond to different

oxidation states of the C atoms. These states include the non-oxygenated C (284.8 eV), the C in C-O bonds (286.2 eV), and the C in C=O bonds (287.8 eV).[96] As compared to GO, the peak intensities of C-O and C=O in GO-1N (Figure 2b) significantly decreased. GO-2N and GO-3N show similar phenomenon (not shown). The carbon-to-oxygen (C/O) atomic ratio was calculated by the decomposition of C 1s showing in the XPS spectrum. As shown in Table 1, GO has a C/O ratio of 1.9. In contrast, the C/O ratio of GO-1N increases to 2.7, and GO-2N and GO-3N have even higher C/O ratios of 4.0 and 4.5, respectively. This suggests that GO reduction has occurred and some of the oxygen-containing groups have been removed during the silylating reaction. In particular, the silane agent with triamine end groups reduces GO most effectively. Additionally, significant amounts of N 1s and Si 2p from functionalized GO were detected (**Figure 30**c and d), indicating that the GO surface has also been successfully functionalized with silane molecules.

Table 3. C/O ratio and amine group concentration of GO and silane-functionalized GO.

Samples	C/O ratio	Residual weight after 900 ^{o}C (wt. %)	-NH group concentration (mmol/g)
GO	1.9	0	0
GO-1N	2.7	34	5.6
GO-2N	4.0	25.5	8.4
GO-3N	4.5	20.8	10.2

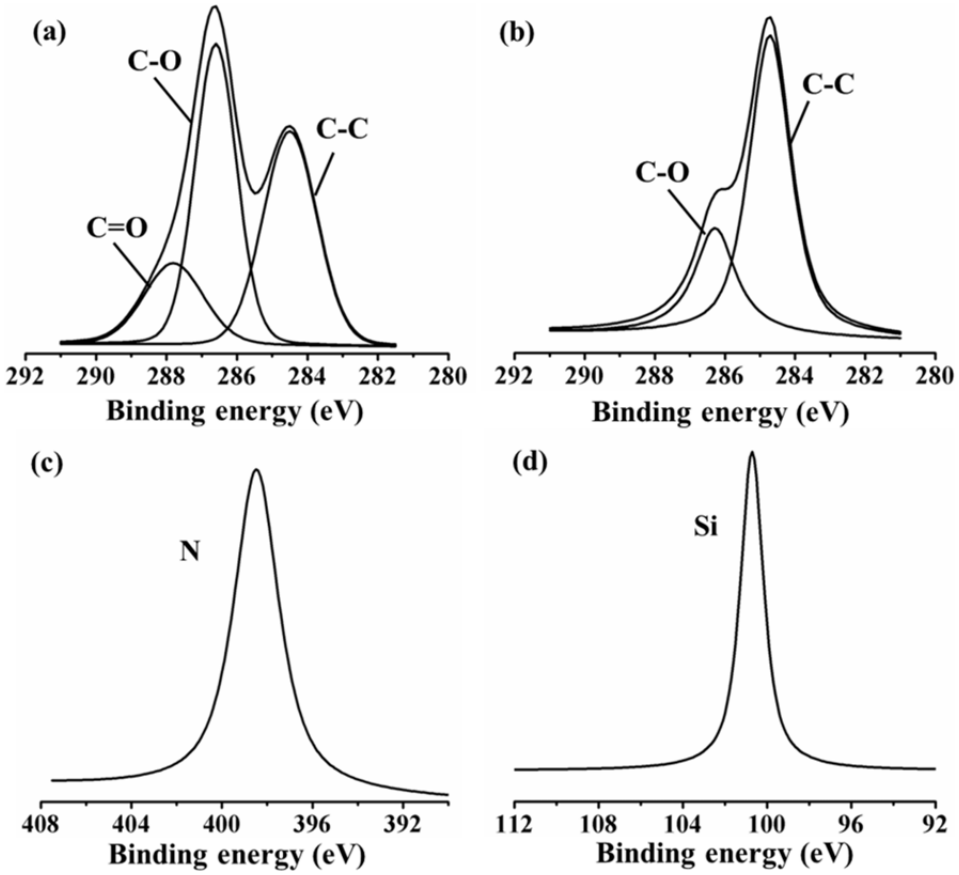

Figure 30. XPS spectra of (a) C 1s of GO, (b) C 1s of GO-1N, (C) N 1s of GO-1N, and (d) Si 2p of GO-1N.

To further confirm the presence of the functional groups on the GO surface, GO and organosilane-functionalized GO were characterized by FTIR (**Figure 31**). GO shows a broad and tense peak at 3500~3300 cm^{-1}, corresponding to the stretching vibrations of the O-H groups on graphene sheet. The C=O stretching at 1728 cm^{-1} and C-O stretching at 1200~1100 cm^{-1} indicate the presence of carboxylic and epoxide groups on GO sheets. Compared with GO, functionalized GO shows several new peaks in the ranges of 2700~3000 cm^{-1} and 1700~1000 cm^{-1}. The new peaks at 2925 and 2850 cm^{-1} are associated with the stretching vibration of $–CH_2–$ groups from silane molecules, and the

sharp peak at 1577 cm^{-1} is assigned to the bending vibration of -NH-.[103] The stretching vibration of Si-O-C at 1107 cm^{-1} strongly indicates that the silylation of GO has occurred. The 1728 cm^{-1} (C=O asymmetric stretching) peak of GO spectrum has disappeared after functionalization, implying the removal of –COOH from GO sheets after the reaction.

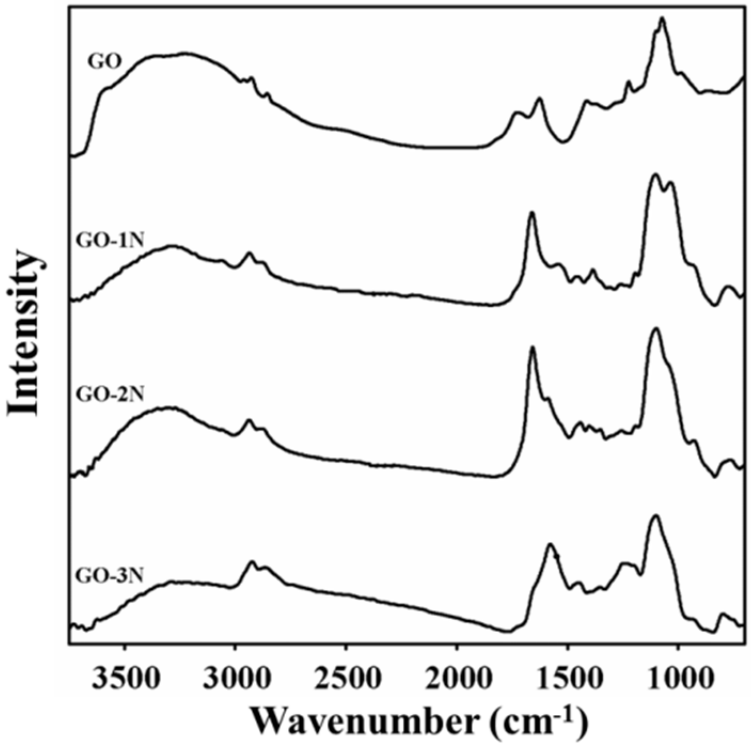

Figure 31. FTIR spectra of GO and organosilane-functionalized GO.

The compositions of organosilane-functionalized GO were measured by TGA. **Figure 32** shows the TGA curves of GO-1N, GO-2N, and GO-3N, as well as the pristine GO. GO in air exhibits two weight losses at 200 °C and 500 °C, respectively, attributing to the decomposition of oxygen-containing groups and carbon combustion. The organic

components in silylating agents decompose at a temperature range from 200~400 °C.[103] Assuming that all the residual weight after 900 °C for GO-*x*N was SiO_2, the compositions of GO-*x*N, especially the concentration of amine groups, were calculated and summarized in **Table 3**. GO-1N (5.6 mmol/g) has the lowest amine group concentration. GO-2N (8.4 mmol/g) and GO-3N (10.4 mmol/g) have much larger concentrations, which are 1.5 times and 1.8 times larger than that of GO-1N. The ability to control the concentration of amine groups cannot be overestimated, because the amine group is the key for further tailoring the grafting density of Au NPs.

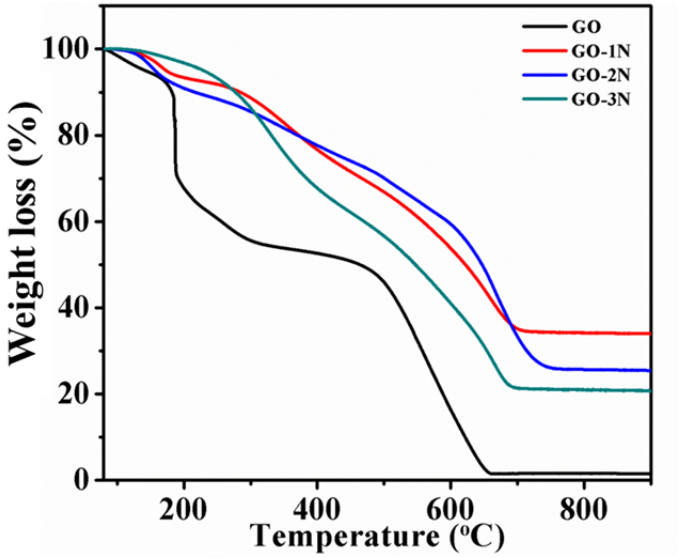

Figure 32. TGA curves of GO and organosilane-functionalized GO.

Introducing surface functionalization for Au NPs can improve their colloidal stability, but the strong binding of the surface capping ligands often results in "poisoning" - deactivation of the nanocatalysts. To obtain catalytically active GO/Au composites, Au NPs are required to immobilize solely on the graphene surface, but not

embedded within the organosliane layer. To that end, a monomolecular layer of silane on the graphene surface is critical to avoid the embedding of Au NPs. Direct evidence concerning the molecular morphology of GO-*x*N sheets comes from AFM studies. The dispersion of GO-*x*N was drop-dried on a mica substrate, and the thicknesses of the GO-*x*N are measured in the range of 2.2~2.8 nm (a typical AFM image is shown in **Figure 33** for the case of GO-2N). It is well known that GO has a thickness of 0.8 nm. The average thickness of the silane agents is in the range of 1~2 nm, which adds up to a total thickness of GO-*x*N in the range of 1.8 ~ 2.8 nm.[106] This is a compelling evidence that silane indeed forms a monomolecular layer on the graphene surface.

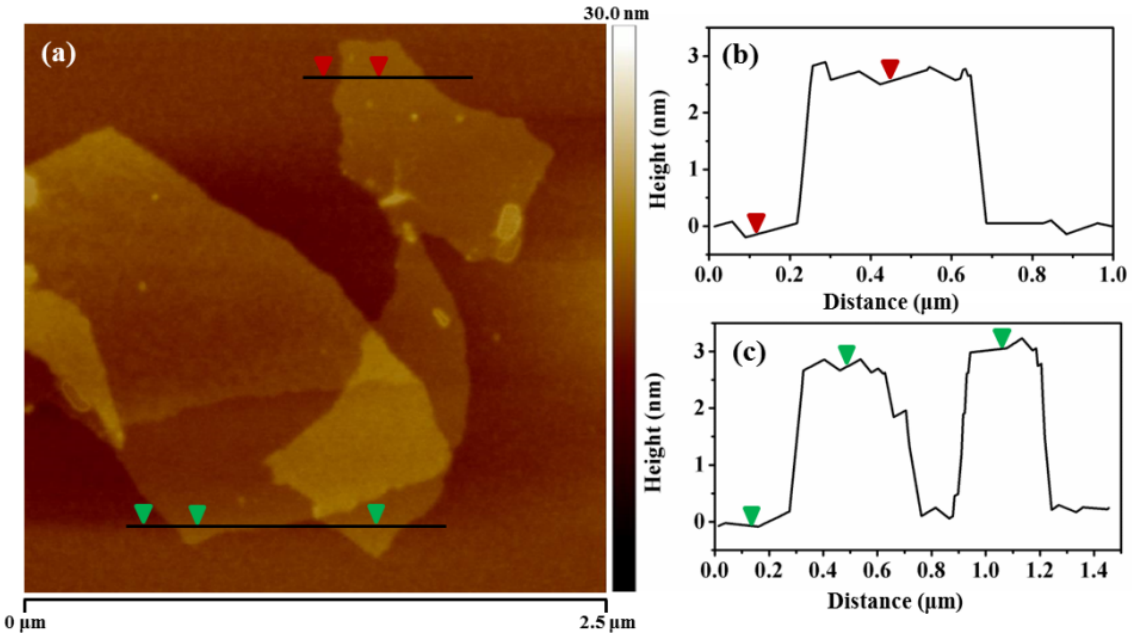

Figure 33. (a) AFM image of GO-2N coated onto a freshly cleaved mica surface showing single or multilayered sheets, (b) and (c) height profiles of GO-2N as labeled in (a).

5.3.2 Preparation of GO/Au nanocomposites

Our protocol for fabricating GO/Au nanocomposites exploits the simplicity of self-assembly of Au NPs from solution and their affinity for amine functional groups. As discussed above, silane molecules form a stable self-assembled monolayer on GO surface through covalent bond. Terminated amine groups point outwards away from the graphene surface and serve as anchoring sites for Au NPs. Immersion of the functionalized graphene into a solution of Au NPs causes Au NPs to anchor on graphene surface through Au-N covalent bond formation. The advantage of the colloidal self-assembly approach is that the covalent bond between nanoparticles with the substrate reduces the surface mobility of the nanoparticles and prevents spontaneous coalescence of nanoparticles.

The self-assembly of Au NPs on functionalized GO was achieved through immersion of GO-*x*N in pre-synthesized Au NPs aqueous solutions at 35 ^{o}C for 20 hours. After washing off excess Au NPs, the solution of GO/Au exhibited a reddish color (inset in **Figure 34**). The binding of Au NPs to organosilane-coated substrates develops in two stages: (1) reaction rate-controlled Au NPs deposition on GO-*x*N, and (2) saturation coverage of Au NPs controlled by repulsive interaction between the neighboring particles.

Pristine Au NPs with 10 nm size have a surface plasmon resonance peak around 520 nm in the visible spectrum.[111] The surface plasmon resonance peaks of the assembled GO/Au nanocomposites become much broader and have redshifts due to the strong inter-particle coupling of closely packed particles (**Figure 34**a). Au NPs are well

known for their strong interactions with visible light, *i.e.* resonant excitations of the collective oscillations of the conductive electrons within the particles.[134] The surface plasmon resonance energy of Au NPs depends on their size, shape, and surrounding environment.[135] When Au NPs are closely packed, the coupling effect between particles becomes eminent, and the surface plasmon resonance wavelength of the two coupled particles will shift to a high wavelength.[111, 112] Among these nanocomposites, GO-3N/Au has the largest redshift (18 nm), whereas GO-1N/Au has the smallest redshift (10 nm). This indicates that the inter-particle spacing between Au NPs could be altered by varying functional groups on the graphene surface.

TEM observation reveals the same trend toward the grafting density of Au NPs as confirmed from UV-Vis results. TEM images of GO-1N/Au and GO-2N/Au show relatively loose-packed NPs, but GO-3N/Au displays closely packed NPs on the graphene surface. The Au NP density on the graphene sheets was determined using ImageJ (freeware from the National Institutes of Health). The densities of Au NPs on GO-3N/Au, GO-2N/Au and GO-1N/Au are 7,200, 6,000 and 4,800 μm^{-2}, respectively. Compared with the other two silane-functionalized graphene, GO-3N has the highest Au NP grafting density.

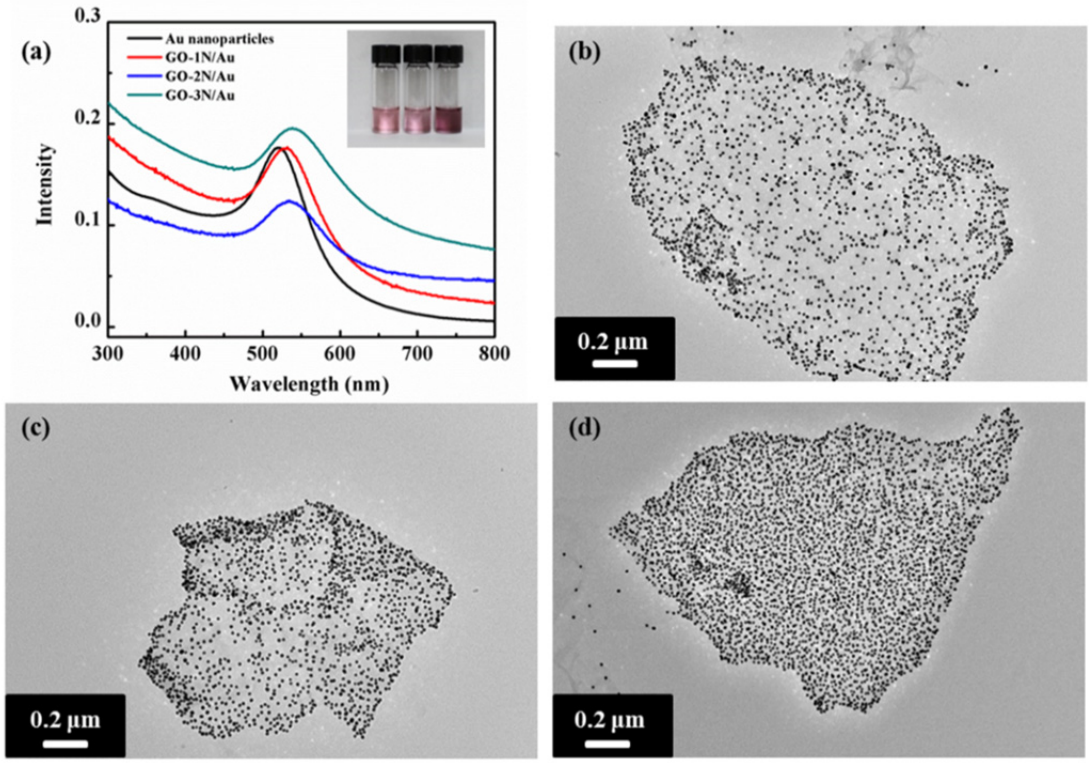

Figure 34. (a) UV-Vis spectra of Au, GO-1N/Au, GO-2N/Au, and GO-3N/Au. Inset: Photographs from left to right of dispersions of GO-1N/Au, GO-2N/Au, and GO-3N/Au. TEM images of (b) GO-1N/Au, (c) GO-2N/Au, and (d) GO-3N/Au.

As discussed above, there are two stages for Au NP binding to organosilane-coated substrates: initial Au NP deposition on GO substrates, which increases with time and late saturated Au NP coverage due to repulsive interaction among Au NPs. During the initial stage, terminated amine groups on graphene surface serve as anchoring sites for Au NPs. Immersion of the functionalized graphene into a solution of Au NPs causes Au NPs to anchor on graphene surface through Au-N covalent bond formation. In addition to the time factor, the concentration of amine groups is one factor to determine the binding rate. As confirmed by the TGA results, the amine group concentration is the highest for GO-3N, followed by GO-2N, and by GO-1N. Because of the high

concentration of amine groups, GO-3N has the highest chance to attract and graft Au NPs than GO-2N and GO-1N. This conclusion agrees with the results observed from TEM images. Immobilization of Au NPs with high density on the graphene surface can maximize the active surface area exposed to reaction media, which is crucial for a consistent, highly efficient catalyst performance.

5.3.3 Catalytic properties of GO/Au nanocomposites

The effectiveness of the catalytic activity of the GO/Au nanocomposites is validated through a typical catalytic reaction, *i.e.* the hydrogenation of 4-nitrophenol (4-NPh) to 4-aminophenol (4-APh) using $NaBH_4$ as the hydrogen source. 4-NPh is a harmful and hazardous chemical that is typically found in industrial products and agricultural waste.[136] The hydrogenation of 4-NPh to 4-APh is one of the necessary processes for manufacturing fine and industrial chemicals. However, this hydrogenation process could not be realized, unless a catalyst (*e.g.* Au NPs) is used.[54] This process involves three steps: 1) hydrogen generation from $NaBH_4$, 2) absorption of hydrogen on Au NPs, and 3) reduction of 4-NPh to 4-APh through the Au-absorbed hydrogen.[127, 137] The third step allows a real-time monitoring of the reaction process by UV-Vis spectroscopy. 4-NPh forms 4-nitrophenolate anions in alkaline reaction media with a strong absorption peak at 400 nm, and 4-APh has an absorption peak at 295 nm. When the GO/Au nanocomposite was introduced into the reaction mixture, the hydrogenation reaction proceeded simultaneously with an increase in the absorption intensity at 295 nm (indicator of the product) and a decrease at 400 nm (indicator of the reactant) (**Figure**

35a). The solution color changes from yellow to colorless when all 4-NPh is consumed (inset in **Figure 35**a).

All three GO/Au nanocomposites show high efficiency in catalyzing the hydrogenation reaction, finishing the reaction within 16 min. The reaction kinetics is studied to better understand the relationship between the grafting density of Au NPs and their catalytic performance. The pseudo-first-order reaction kinetics were applicable to analyze the reaction rate constant, considering that the concentration of $NaBH_4$ is in large excess relative to that of 4-NPh (**Figure 35**b).[54] The highest efficiency was obtained from GO-3N/Au, followed by GO-2N/Au and GO-1N/Au, having a rate constant of 0.15 min^{-1}, 0.13 min^{-1}, 0.11 min^{-1}, respectively. As expected, the catalytic efficiency becomes higher as the particle grafting density increases. The catalytic rate constant for GO/Au nanocomposites is proportional to the Au NP density. According to the particle density calculation described above, the Au NP densities of GO-2N/Au and GO-3N/Au are 1.2 and 1.5 times larger than that of GO-1N/Au. The corresponding rate constants for GO-2N/Au and GO-3N/Au are expected as 0.13 min^{-1} and 0.16 min^{-1}, which are in agreement with the experimental findings.

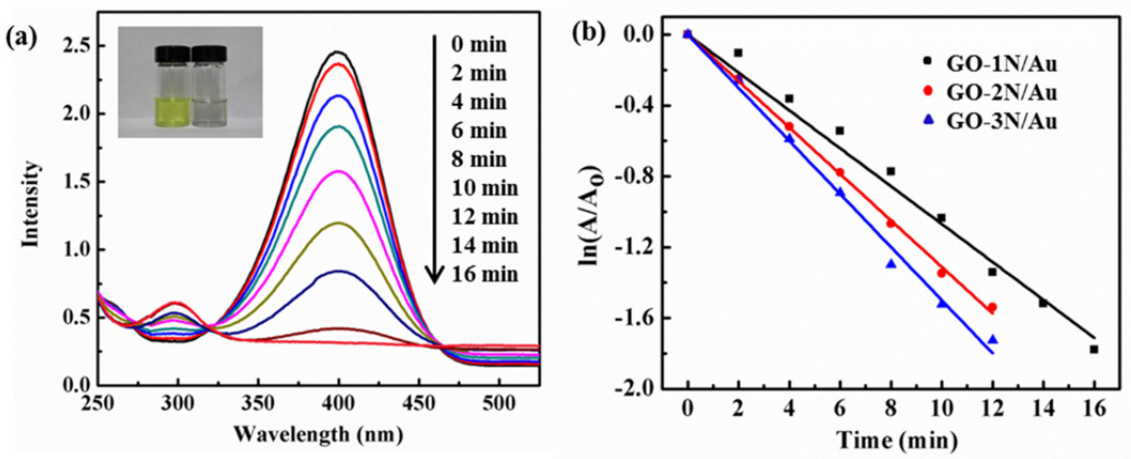

Figure 35. (a) Time-dependent UV-Vis spectra of the reaction mixture of catalytic reduction of 4-NPh with GO-1N/Au, inset: Photograph of aqueous solutions of 4-NPh before and after reduction, and (b) dependence of ln(A/Ao) on reaction time for the reactions by GO-N/Au catalysts (R^2 for linear fitting = 0.93 (GO-1N/Au), 0.99 (GO-2N/Au), 0.99 (GO-3N/Au)). All catalysts are used at the same molar ratio based on graphene and 40 equiv. of $NaBH_4$ for the reaction.

It has been demonstrated up to this point that the GO/Au nanocomposite allows tailoring the catalytic reaction rate. The section below demonstrates that these nanocomposites could be easily separated from the reaction system and reused in a new catalytic reaction. To check the reproducibility and stability of the catalyst, repeated hydrogenation reactions of 4-NPh to 4-APh were carried out using GO-3N/Au. Between each repeated reaction, the GO-3N/Au was removed from the reaction and rinsed with water. Our results show that there is no detectable loss of catalytic activity after 8 successive reactions (**Figure 36**a), which is the highest cycle number ever reported.[54, 130] The stability of the GO-3N/Au nanocomposite was confirmed by UV-Vis spectroscopy (**Figure 36**b). The absorption peak of GO-3N/Au does not shift after 8 successive reactions. Additionally, a TEM image of GO-3N/Au after successive reactions was taken. There is no discernable difference in structures before and after 8 times of reuses.

The results from UV-Vis spectra and TEM image indicate that 1) Au NPs does not change their inter-particle spacing after repeated catalytic reactions, and 2) the GO-3N/Au nanocomposite survived after catalytic cycles without showing signs of detachment or aggregation. Therefore, it is clearly demonstrated that silane-functionalized GO plays a vital role in preventing Au NPs from aggregation and maintaining full catalytic activity after successive cycles of reaction.

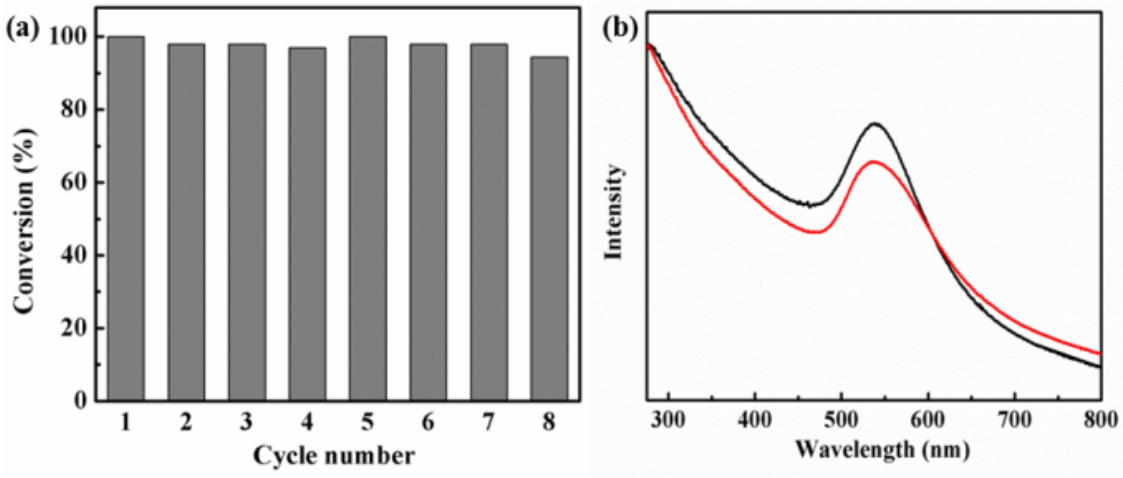

Figure 36. (a) Catalytic conversion efficiency of 4-NPh in 8 continuous reaction cycles, and (b) UV-Vis spectra of GO-3N/Au before (black line) and after 8 continuous reaction cycles (red line).

5.4 Conclusions

We have developed a method to fabricate highly active, tunable, and reusable catalysts through self-assembly of Au NPs on organosilane-functionalized GO. Silane coupling agents with different amine end groups lead to GO/Au nanocomposites with controlled Au NP grafting density, which help better understand how the Au packing density influences catalytic activity. This approach realizes tailored morphology,

grafting density, and chemical configuration, which could not be otherwise obtained by other methods. This realization is crucial toward the development and optimization of heterogeneous nanocatalysts.

CHAPTER VI

ORGANIC SOLVENT DISPERSION OF ZNO-MWCNTS AND THEIR APPLICATIONS AS HIGH PERFORMANCE PHOTOCATALYST UNDER VISIBLE LIGHT IRRADIATION

6.1 Introduction

Carbon nanotubes (CNTs) have attracted considerable attention in the fields of science and engineering due to their numerous attractive properties, such as excellent transport and tensile properties.[4, 138, 139] Recently, many efforts have been dedicated to the development of versatile chemical modification methodologies and CNT derivatives with even more attractive features.[24, 45] For example, CNTs have been used as templates or scaffolds for the assembly of metal or metal oxide nanoparticles.[24] These CNT/nanoparticle hybrids have emerged as a new class of compounds in the field of material science due to their unique electronic, optical, magnetic and catalytic properties.

Among the various semiconductor metal oxides, ZnO has attracted great attention because of its wide band gap (3.37 eV), high electron mobility, low cost, and environmental friendliness.[140] The combination of CNT and ZnO nanoparticles may lead to a successful integration of the properties of the two components in the new hybrid materials that present important features for catalysis and nanotechnology. Traditionally, ZnO-CNT hybrids can be prepared by either a thermal deposition method or a solution method depending on the zinc source used.[141-143] The thermal deposition method always involves strict conditions at a high temperature (up to 1000 ^{o}C). For example, ZnO can

be directly grown onto CNTs via a vapor-solid growth mechanism, where Zn is supplied by evaporation of a foil at 500−600 °C.[42] On the other hand, the solution method is usually preferable due to its scalability and ease of processing. Sun *et al.*[144] reported a water-in-oil microemulsion method to deposit ZnO particles on MWCNTs through decoration of MWCNT with sodium dodecyl sulfate, followed by reaction of zinc acetate with lithium hydroxide monohydrate in anhydrous ethanol.

Although many efforts have been made to develop ZnO-CNT hybrids, most of the particle sizes were well above 10 nm and up to 70 nm. Thus, challenges still exist to prepare well integrated ZnO-CNT hybrids at low temperature (<100 ^{o}C) with particle size lower than 10 nm. In the present study, two simple and straightforward methods, mixing and *in situ* methods, have been developed to prepare ZnO-MWCNT hybrids with an average particle size of 4~5 nm. During the sample preparation, we found that MWCNTs would undergo a remarkable stabilizing transition upon addition of an adequate amount of ZnO nanoparticles in methanol. To the best of our knowledge, this is the first report to demonstrate the dispersion of MWCNTs in organic solvent through the assistance of ZnO nanoparticles. In addition, the ZnO-MWCNT hybrid with well-dispersed and nanometer-sized ZnO nanoparticles shows superior performance for the photodegradation of Rhodamine B under visible light irradiation. Possible reasons for the enhancement in photocatalytic activity are discussed in this work.

6.2 Materials and methods

6.2.1 Materials

The MWCNTs (SMW^{TM} 100 nanotubes, diameter: 6 to 9 nm, length: about 5 microns, carbon content: 98%) were provided by Southwest NanoTechnologies and were used as received. Zinc acetate dihydrate, potassium hydroxide, and methanol were purchased from Sigma-Aldrich and were used as received.

6.2.2 Preparations of ZnO nanoparticles and ZnO-MWCNTs

Preparation of ZnO nanoparticles: ZnO nanoparticles were prepared by hydrolyzing zinc acetate dihydrate in methanol. This method has been previously reported elsewhere.[145] KOH (1.0 g, 17.8 mM) was first dissolved in methanol (200 mL) at 70 °C with refluxing and stirring to obtain a homogeneous solution. Subsequently, zinc acetate dihydrate (2.0 g, 8.9 mM) methanol solution (22 mL) was added directly into the basic methanol solution. This mixture was then kept at 70 °C with refluxing and stirring for 2 hours. The prepared ZnO nanoparticles were purified by the precipitation and dispersion procedure, and then were redispersed in methanol. The ZnO nanoparticles have an average diameter of 5 nm.

Preparation of ZnO-MWCNT by mixing method (M-ZnO-MWCNT): The as-received MWCNTs were used without any treatment. MWCNTs (4 mg) were added into methanol (20 mL), and various amounts of ZnO nanoparticles were added to prepare M-ZnO-MWCNT dispersions (weight ratio of ZnO to MWCNT: 0:1, 1:2, 1:1, 2:1, 4:1, 8:1, and 20:1. Finally, the mixtures were sonicated for 20 minutes to achieve a homogeneous dispersion.

Preparation of ZnO-MWCNT by in situ method (I-ZnO-MWCNT): The method to synthesize I-ZnO-MWCNT is similar to that of ZnO nanoparticles. MWCNTs (80 mg, 0.8 mg/mL) were mixed with a KOH (0.5 g, 8.9 mM) methanol solution and sonicated for 30 minutes to obtain a homogeneous solution, and then heated to 60 °C. After that, a zinc acetate dihydrate (1 g, 4.5 mM) methanol solution (11mL) was added, and the mixture was kept stirring for 2 hours at 60 °C. The I-ZnO-MWCNT was filtered through a membrane with 0.5 μm pore size to remove ungrafted ZnO nanoparticles.

6.2.3 Characterization

UV-Vis absorption spectra were acquired with a UV-Vis-NIR spectrophotometer (Shimadzu, UV-3600). X-ray photoelectron spectroscopy (XPS) data was obtained with a Kratos Axis Ultra using a non-monochromatic MgK_{α} photon source (1486 eV) for measurements. Transmission electron microscopy (TEM) images were obtained from a JEOL 2010 high-resolution microscope operated at 200 kV. Particle size distribution was determined by measuring the size of over 100 particles using the intercept method from the TEM images in the four randomly selected locations on each sample, and calculating the percent of particles with sizes in the certain range. XRD results were obtained from a Bruker D8-Focus Bragg-Brentano X-ray Powder Diffractometer. Zeta potential measurements were carried out on a Delsa™ Nano Submicron particle analyzer (Beckman Coulter, Inc.). The specimens were diluted to 0.1 mg/mL in a methanol solution for measurements. Raman spectra were obtained from a Horiba Jobin-Yvon LabRam IR system combined with an Olympus BX 41 microscope.

6.2.4 Photocatalytic activities of ZnO and ZnO-MWCNT hybrids

The photodegradation of Rhodamine B (RhB) was carried out under the irradiation of visible light. In a typical process, catalyst (1.5 mg) was suspended in RhB aqueous solution (6×10^{-5} M, 3 mL). Then the solution was exposed to the visible light irradiation produced by a 260 W Xe lamp positioned 20 cm away from the container. The photocatalytic reaction started when the lamp was turned on. During the photocatalysis, the degraded solution was analyzed by UV-Vis spectroscopy at the given time intervals. The durability of the catalyst was tested as follows: ZnO-MWCNT (10 mg) was dispersed in RhB aqueous solution ($3x10^{-5}$ M, 20 mL), and the solution was exposed to the visible light irradiation for 20 min. The catalyst underwent four consecutive cycles and was centrifuged and washed thoroughly with water after each cycle.

6.2.5 Fabrication of the electrodes for EIS measurements

For the EIS measurement, the catalyst (5.0 mg) was dispersed in 1.0 mL methanol, and the solution was then dropped onto the conducting ITO glass substrate (24 Ω/square). Impedance measurements (Solartron 1287) were measured at room temperature. The catalyst-coated ITO served as the working electrode, with a platinum plate and saturated calomel electrodes (SCEs) as the counter and reference electrodes. The supporting electrolyte was a 0.1 M KCl solution containing a 2.5 mM $K_3[Fe(CN)_6]/K_4[Fe(CN)_6]$ (1:1) mixture . The impedance spectra were recorded under an AC perturbation signal of 5 mV over the frequency range of 10^5–0.1 Hz.

6.3 Results and discussion

The procedures for the preparation of ZnO-MWCNT hybrids are illustrated in Error! Reference source not found. Two different methods are used to prepare ZnO-MWCNT hybrids: mixing and *in situ* methods. Compared with other reports, the advantages of the methods in the present work are: simple procedure, no surfactants needed, low temperature and nano-sized ZnO particles.

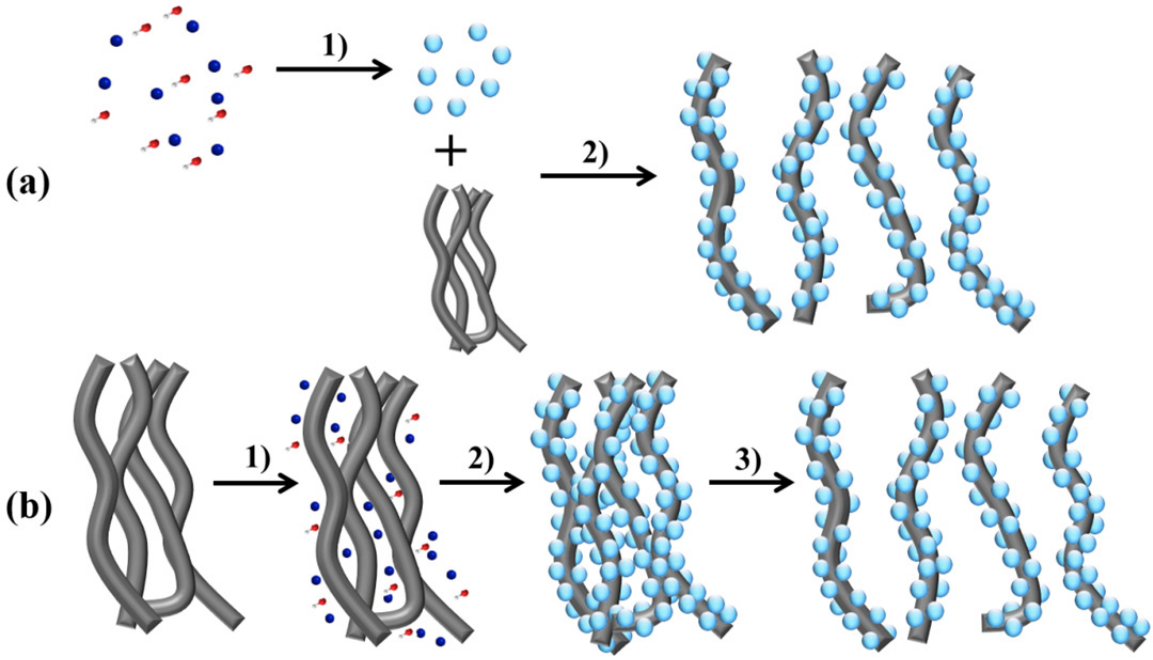

Figure 37. Schematic illustration for the preparation of (a) M-ZnO-MWCNTs and (b) I-ZnO-MWCNTs. (in (a): 1) synthesis of ZnO nanoparticles from zinc acetate and potassium hydroxide in methanol, 2) specific amount of ZnO and MWCNTs were mixed together; in (b): 1) zinc acetate and potassium hydroxide were added into aggregated MWCNTs in methanol, 2) ZnO nanoparticles were grown on the CNT surfaces after 2 hours reaction; 3) homogeneous dispersion of ZnO-MWCNTs in methanol was obtained after 20 minutes of sonication.

6.3.1 ZnO nanoparticle-assisted dispersion of MWCNTs in methanol by mixing method

Colloidal ZnO nanoparticles were pre-synthesized from zinc acetate dihydrate and potassium hydroxide in methanol.[145] The synthesized ZnO nanoparticles were purified through a precipitation-redispersion procedure to remove excess potassium ions and acetate ligands. The purified ZnO nanoparticles have an average diameter of 5 nm (**Figure 38**a). MWCNTs (**Figure 38**b) were mixed with ZnO nanoparticles in methanol, and the mixture was sonicated for 20 minutes. A photograph showing vials of MWCNTs (0.2 mg/mL) with various amounts of ZnO in methanol is shown in **Figure 39**. The amount of ZnO nanoparticles introduced is the key factor to the stabilization of MWCNTs in methanol. In the absence of ZnO nanoparticles, MWCNTs underwent a rapid flocculation due to the strong van der Waals interactions between the tubes. When the weight ratio of ZnO:MWCNT≤2:1, large agglomerates of MWCNTs would settle at the bottom of the vial, yielding a loose-packed sediment. Upon further addition of ZnO nanoparticles to ZnO:MWCNT=2:1~16:1, a dramatic change in the overall stability was observed. The samples remained stable for 3 months with only a trace amount of MWCNTs precipitation detected (not shown). As the ZnO nanoparticle concentration was further increased to ZnO:MWCNT≥20:1, the dispersed MWCNTs began to aggregate in the solution, yielding a dense sediment.

The mechanism that causes MWCNT stabilization within a certain ZnO concentration range was investigated using a zeta potential analysis. The zeta potential is a key indicator of the stability of colloidal dispersions. The magnitude of the zeta

potential indicates the degree of electrostatic repulsion between charged particles in the dispersion. From an electrostatic consideration, an absolute zeta potential value more than 30 mV generally represents a sufficient mutual repulsion that results in particle stability, without aggregation.[146] However, to assure stability with a reasonable factor of safety, the zeta potential should be increased preferably to the range of ±45 mV to ±70 mV. Zeta potential values for M-ZnO-MWCNTs at different weight ratios in methanol are given in **Table 4.** ZnO nanoparticles and MWCNTs have opposite charges and zeta potential values of +44 mV and -15 mV, respectively. Upon mixing with ZnO nanoparticles, the zeta potential values of the MWCNT dispersion change from being negative to positive, and they keep increasing markedly as the concentration of ZnO nanoparticles increases. Due to the opposite sign of charges, ZnO nanoparticles are expected to adsorb onto tube sidewalls. Thus, MWCNTs and ZnO nanoparticles move cooperatively to generate the observed charge buildup.[147]

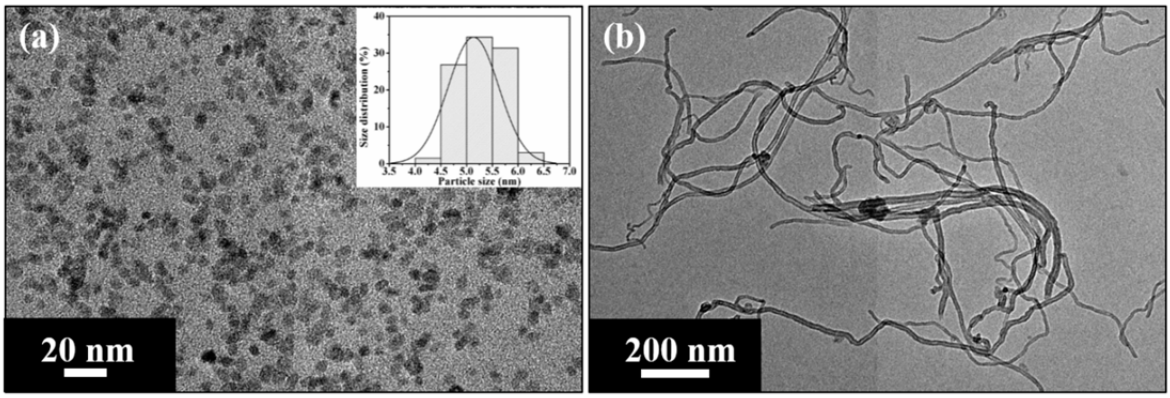

Figure 38. TEM images of (a) ZnO nanoparticles and (b) pristine MWCNTs. Inset: histograms of ZnO nanoparticle size distributions. The average particle size is 5.0±0.5 nm.

The dispersion of ZnO:MWCNTs=1:1 has a zeta potential value of +23 mV. The low zeta potential value indicates that the mixture cannot form a stable dispersion in methanol. This result is consistent with our direct observation of the dispersion as shown in **Figure 39**, where large agglomerates of MWCNTs stay at the bottom of the vial. The small amount of ZnO nanoparticles introduced cannot provide enough electrostatic repulsion between nanoparticle-adsorbed tubes to overcome the van der Waals attraction. When ZnO:MWCNTs≥2:1, zeta potential values become greater than +30 mV, which means that they all form a stable dispersion in methanol. As the concentration of ZnO nanoparticles increases, more nanoparticles are adsorbed onto the nanotube sidewalls. The zeta potential reaches a value of about +71 mV at ZnO:MWCNTs=8:1. It should be noted that when an excess amount of ZnO is introduced (ZnO:MWCNTs≥20:1), re-agglomeration of MWCNT occurs. To understand the re-agglomeration phenomenon, we approximate the sedimentation velocity of a particle from gravitational field.[148] Through calculation, the sedimentation velocity of

ZnO-MWCNT dispersion is nearly 8 times higher than that of pure MWCNT dispersion. Under these circumstances, the Coulombic repulsion between the particles could not overcome the gravitational effect induced by the large mass of ZnO attached to the MWCNTs.

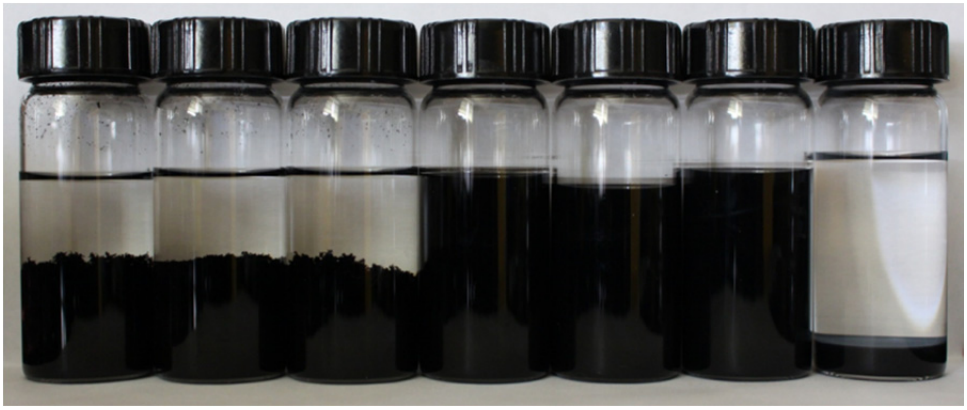

Figure 39. Photograph of MWCNTs dispersion in methanol with different concentrations of ZnO nanoparticles (MWCNTs concentration: 0.2 mg/mL) after 3 months. From left to right, the weight ratio of ZnO:MWCNT equals to 0:1, 1:2, 1:1, 2:1, 4:1, 8:1, and 20:1.

The morphology of ZnO-MWCNTs with different weight ratios was further characterized by transmission electron microscopy (TEM) (**Figure 40**). In general, ZnO nanoparticles are uniformly distributed on MWCNT surfaces. At ZnO:MWCNT=2:1, ZnO nanoparticles are randomly attached to the tube surfaces. As the ZnO nanoparticle concentration increases, the particles pack more densely on the MWCNT surfaces. Some ZnO clusters start to form on the MWCNT surfaces when ZnO:MWCNTs=8:1. It is important to note that all ZnO particles were attached to MWCNTs and no individual or aggregated ZnO nanoparticles were isolated without being attached to the MWCNT surfaces. This suggests that it is the Coulombic attraction between ZnO and MWCNTs

rather than the capillary force that causes the ZnO nanoparticles to assemble onto the MWCNT surfaces during the TEM sample preparation procedure.

Table 4. Zeta potential of ZnO-MWCNTs at different weight ratios in methanol.

Weight ratio of ZnO to MWCNTs	**M-ZnO-MWCNTs**							**I-ZnO-MWCNTs**
	0:1	1:1	2:1	4:1	8:1	20:1	1:0	2:1
Zeta potential (eV)	-15	+23	+46	+62	+71	+76	+44	+41

6.3.2 ZnO nanoparticle-assisted dispersion of MWCNTs in methanol by *in-situ* method

As illustrated in **Figure 37**, the synthesis of ZnO-MWCNTs by *in situ* method is as follows: a specified amount of pristine MWCNTs was directly mixed with zinc acetate dehydrate and potassium hydroxide in methanol, and the solution was kept at 60 °C for 2 hours with refluxing and stirring. After excess ZnO nanoparticles were removed through filtration, the I-ZnO-MWCNTs were redispersed in methanol, and the mixture was sonicated for 20 minutes to achieve a homogeneous dispersion. The steric hindrance effect and electrostatic repulsion of ZnO nanoparticles, along with sonication, helped disentangle the MWCNTs.

The morphologies of the resultant I-ZnO-MWCNTs were characterized by TEM, which provides direct evidence that ZnO nanoparticles directly graft around tube sidewalls. The TEM image of the hybrid (**Figure 41**) clearly indicates that spherical nanoparticles are closely packed on the MWCNT surface. **Figure 41**b shows the high-resolution TEM image of the I-ZnO-MWCNTs prepared for the present study. The

spacing between adjacent walls of the MWCNTs has been measured to be 0.35 nm. ZnO nanoparticles are highly crystalline and the interplanar spacing of ZnO was measured to be 0.28 nm, which corresponds well with the (100) plane of ZnO with a hexagonal structure.[149] The statistical analysis of particle size based on 100 nanoparticles from the high-resolution TEM images yields an average particle size of 4.5 ± 0.5 nm. Thermogravimetric analysis (TGA) was used to measure the relative content of ZnO and MWCNTs in the I-ZnO-MWCNT hybrid (**Figure 41**d). A total weight loss of 5 wt.% was observed for the purified colloidal ZnO nanoparticles due to acetate ions bound on the ZnO surface. For the I-ZnO-MWCNTs, two weight loss processes were observed: the first one was assigned to the loss of acetate ions, similar to the purified ZnO; the second weight loss at 400 °C was assigned to the loss of MWCNTs, and the MWCNT content was calculated to be 32 wt.%. Thus, the weight ratio of ZnO to MWCNTs is roughly 2:1.

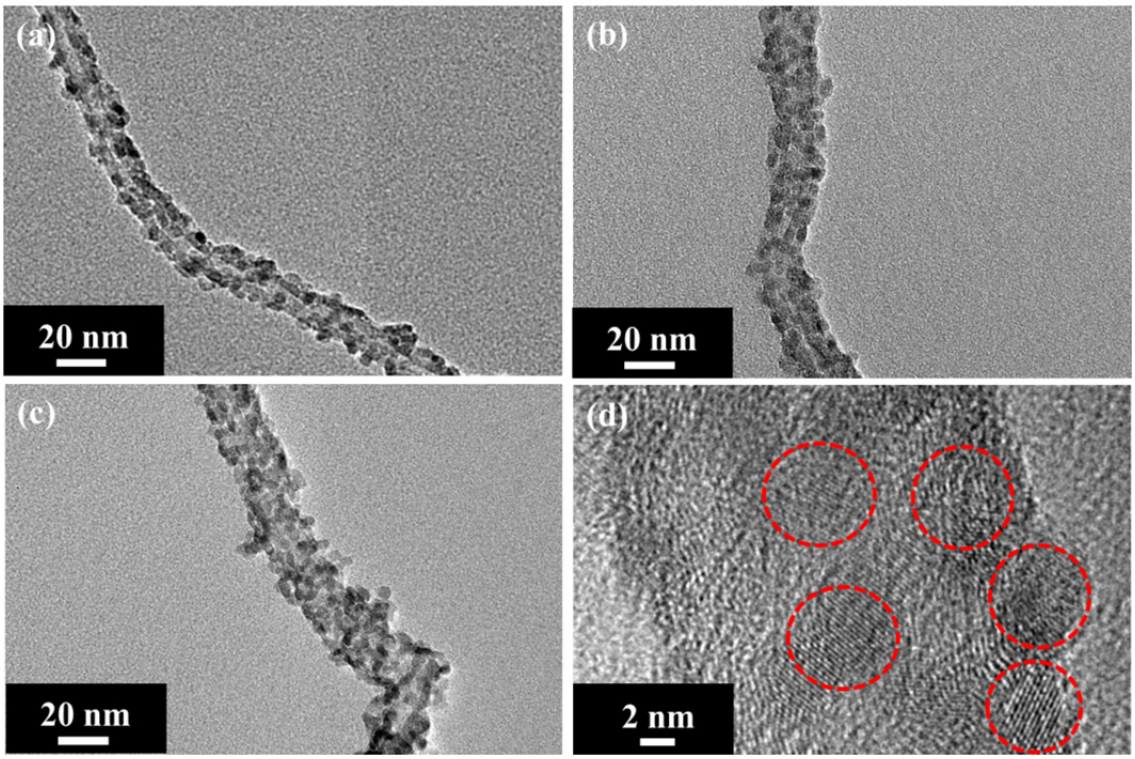

Figure 40. TEM images of M-ZnO-MWCNTs with a ZnO to MWCNTs weight ratio of (a) 2:1, (b) 4:1, (c) 8:1, and (d) a high magnification image of (b). The circles highlight the size of the ZnO nanoparticles.

The I-ZnO-MWCNTs demonstrate good solubility and stability in methanol. The solution can remain stable for several months at concentrations up to 3 mg/mL. After the deposition of ZnO nanoparticles around the tube surfaces, the surface potential of MWCNTs has been changed and the I-ZnO-MWCNTs have a zeta potential of +41 mV (**Table 4**). This indicates that the dispersion mechanism for I-ZnO-MWCNT in methanol is similar to that of M-ZnO-MWCNT (Weight ratio of ZnO to MWCNTs is 2:1.). The positively charged ZnO nanoparticles on the tube surface induce enough electrostatic repulsion between the tubes and lead to a homogeneous, stable dispersion in methanol.

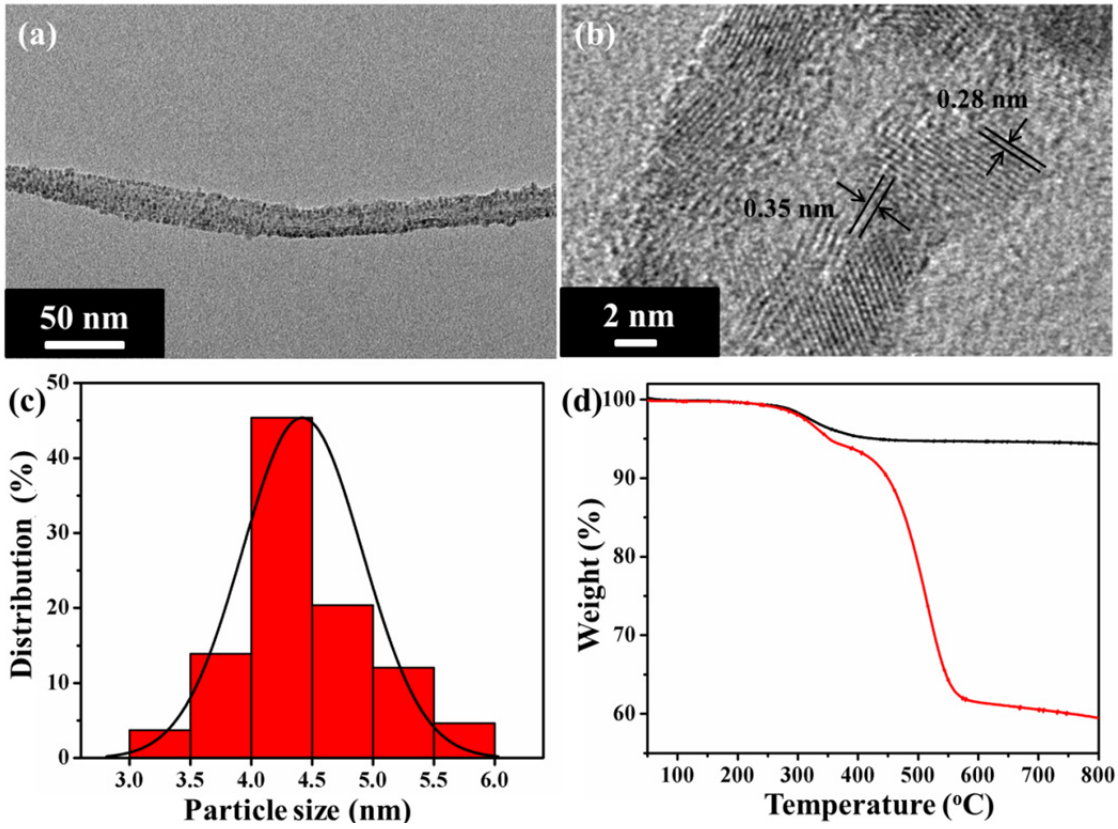

Figure 41. (a) and (b) TEM images of I-ZnO-MWCNTs in low magnification and high magnification, (c) histograms of ZnO nanoparticle size distributions (the average particle size is 4.5±0.5 nm), and (d) TGA curves of ZnO and I-ZnO-MWCNTs.

6.3.3 Characterization of ZnO-MWCNTs prepared by mixing and *in situ* methods

Figure 42a shows the UV-Vis absorption spectra of MWCNTs, ZnO and ZnO-MWCNT hybrids in methanol. MWCNTs show a large absorption range from 250-500 nm. The absorption spectrum of ZnO exhibits a well-defined absorption onset characteristic at 359 nm. The spectrum of ZnO-MWCNTs shows the absorption arising from both MWCNTs and ZnO in the hybrid. Raman spectroscopy has been carried out to verify the structural state of MWCNTs after the ZnO nanoparticle coating. The spectra are dominated by two peaks located at 1316 cm^{-1} (D band) and 1579cm^{-1} (G band). In

the high frequency spectra, a G-band represents crystalline graphitic carbon, and a D-band indicates defects, curved graphite sheets and lattice distortions in the carbon structures.[150] The intensity ratio between D band and G band (I_D/I_G ratio) is often used as a measure of the CNT quality. As shown in **Figure 42**b, the I_D/I_G ratio of ZnO-MWCNTs prepared by both methods is approximately the same as that of pristine MWCNTs (I_D/I_G ratio = 2.1). This indicates that the electronic structure of MWCNTs has been kept intact after the attachment of ZnO nanoparticles.

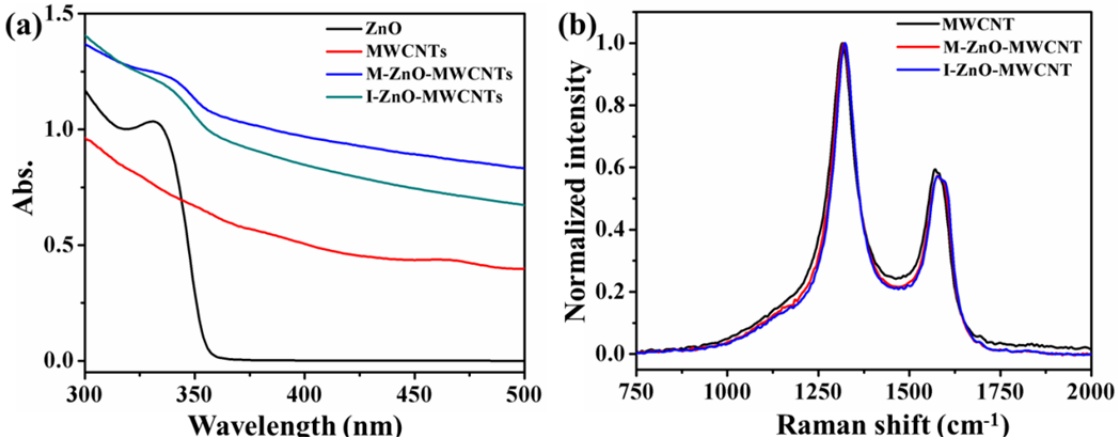

Figure 42. (a) UV-Vis absorption of ZnO, MWCNTs, M-ZnO-MWCNTs, and I-ZnO-MWCNTs (for M-ZnO-MWCNTs, the weight ratio between ZnO and MWCNTs is 2:1), and (b) Raman spectra of MWCNTs, M-ZnO-MWCNTs, and I-ZnO-MWCNTs.

The chemical composition of the ZnO-MWCNT hybrids was confirmed by X-ray photoelectron spectroscopy (XPS). **Figure 43** represents a typical XPS survey spectrum of ZnO-MWCNTs, which indicates that carbon, oxygen, and zinc are the dominant species. The high-resolution XPS spectra of Zn2p3/2 for ZnO and ZnO-MWCNTs are shown in **Figure 43**b. The spectrum for the ZnO samples reveals that the core Zn 2p3/2 peak is positioned at 1021.4 eV with high symmetry, indicating that Zn was present only

in in the Zn^{2+} state.[151] However, the Zn 2p3/2 peaks of M-ZnO-MWCNT and I-ZnO-MWCNT exhibit a shift to a higher binding energy by 0.2 eV and 0.46 eV, respectively. The shift to a higher binding energy signifies an increased oxidation of Zn, resulting from their contact with the electronegative MWCNTs.[152] This corroborates with TEM results shown in **Figure 40** and **Figure 41** in which the highly crystalline ZnO nanoparticles were observed to be firmly attached to the surface of CNTs. However, I-ZnO-MWCNT has a stronger interfacial interaction between ZnO and MWCNT than M-ZnO-MWCNT does.

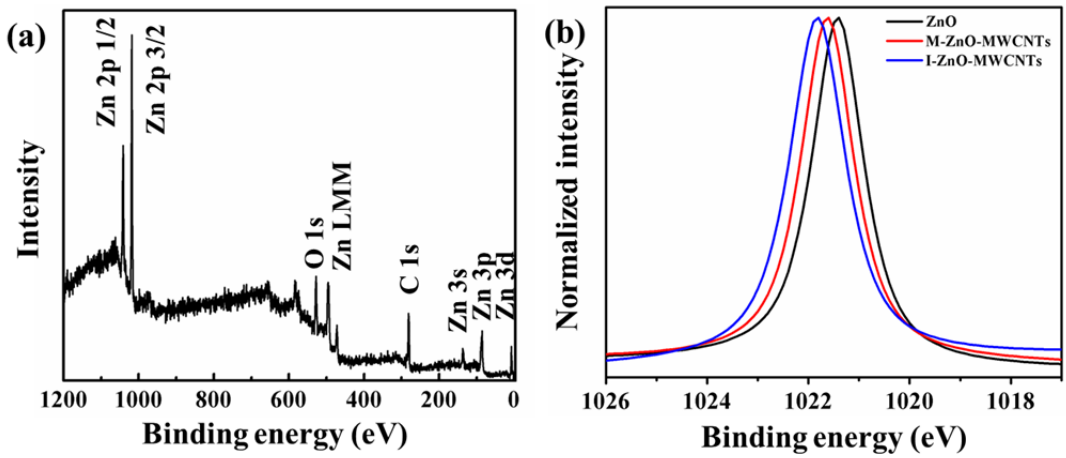

Figure 43. XPS survey spectrum of I-ZnO-MWCNTs, and (b) XPS spectra of Zn peak for ZnO, M-ZnO-MWCNTs and I-ZnO-MWCNTs.

Figure 44 shows the XRD patterns of ZnO, MWCNT and ZnO-MWCNT hybrids. M-ZnO-MWCNT and I-ZnO-MWCNT exhibit similar XRD patterns. The diffraction peaks at $2\theta = 31.7°$, 34.3°, 36.1°, 47.4°, 56.4°, 62.91°, and 67.9° correspond to the wurtzite ZnO structure of (100), (002), (101), (102), (110), (103) and (112) reflections, respectively.[145, 153] The characteristic peaks for MWCNT are also observed

in ZnO-MWCNT hybrids at the positions of 2θ = 25.9° and 43.2°, and are attributed to (002) and (100) reflections.[154]

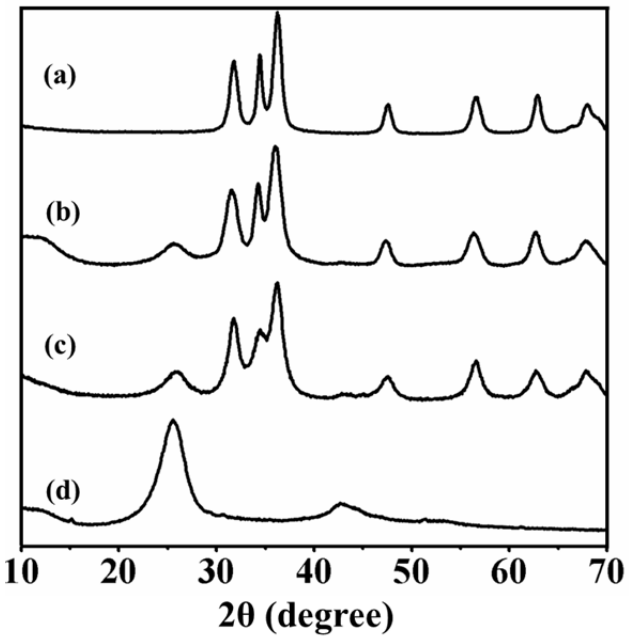

Figure 44. XRD results of (a) ZnO, (b) M-ZnO-MWCNT, (c) I-ZnO-MWCNT, and (d) MWCNT.

Up to this point, it has been proved that MWCNTs can be dispersed in methanol through the coating of ZnO nanoparticles *via* either mixing method or *in situ* method. The underlying mechanism for this dispersion process is the adsorption of ZnO nanoparticles on the MWCNT surface changes the surface nature of the tubes and induces electrostatic repulsion between them. Therefore, a method capable of effectively dispersing MWCNTs in low boiling point and low toxicity solvents without degrading their intrinsic properties is developed.

6.3.4 Photocatalytic activity of ZnO-MWCNT hybrids

Semiconductor-based photocatalysts have received extensive attention due to their capability to capture and convert solar energy to degrade environmental pollutants.[155] ZnO, as a promising semiconductor photocatalyst, still suffers from the drawbacks of photocorrosion and high recombination rate of electron-hole pairs.[140] To overcome these drawbacks and enhance the photocatalytic efficiency, hybridizing ZnO with CNTs is an effective and promising strategy because of the unique electronic properties and large surface area of the CNTs.[156, 157] The photocatalytic activities of ZnO and ZnO-MWCNT hybrids were measured by the photodegradation of rhodamine B (RhB) as a model reaction under visible light. The temporal evolution of the spectral changes during the photosensitized degradation of RhB in the presence of ZnO and ZnO-MWCNT hybrids are displayed in **Figure 45**. In general, in the presence of catalysts, visible light irradiation of the aqueous RhB solutions leads to a decrease in its absorption with time, but the absorption peak of RhB does not shift with increasing time. This indicates that the photodegradation of RhB is dominated by the degradation of the aromatic chromophore but not the de-ethylation of RhB.[155, 158]

As shown in **Figure 45**c, these catalysts present different photodegradation efficiencies. ZnO shows rather poor photocatalytic activity. Only 13% of RhB was decomposed in 24 min, and it took 300 min for the total degradation of RhB. In contrast, ZnO-MWCNT hybrids exhibit remarkable improvements in the photodegradation of RhB. M-ZnO-MWCNT and I-ZnO-MWCNT show similar degradation efficiency and could degrade approximately 100% of the dye molecules in 20 min. This result is

different from most of the reports, in which the hybrid prepared by mixing method has a much lower efficiency than that prepared by *in situ* method.[159] One possible explanation for the high efficiency of M-ZnO-MWCNTs is the efficient hybridization effect between ZnO and MWCNTs. The ZnO nanoparticles used to prepare the M-ZnO-MWCNT hybrid have an average particle size of 4~5 nm, which is smaller than the particle size in most of the reported ZnO-MWCNT hybrids.[160-162] The large surface-to-volume ratio of ZnO nanoparticles can provide a large contact surface area with MWCNTs. Moreover, due to their opposite surface charges (**Table 4**), they could form close, tight contact with each other, which can be proven by their morphology as shown in TEM characterization. Their tight physical contact leads to an efficient hybridization effect. The hybridization effect can be verified by the shift of Zn 2p3/2 peaks in the high-resolution XPS spectra of M-ZnO-MWCNTs (Error! Reference source not found.). Such a hybridization effect could retard the recombination of electron-hole pair and inhibit the photocorrosion of ZnO nanoparticles.[163]

The normalized temporal concentration changes (C/C_0) of RhB during the photodegradation were derived from its normalized absorbance (A/A_0) (at 550 nm) at a given time interval. It was clear from **Figure 45**c that the ZnO-MWCNT hybrids show significantly higher photocatalytic activity than pure ZnO. The apparent reaction constants of ZnO and ZnO-MWCNTs were calculated through pseudo first-order kinetics:[164]

$$\ln\left(\frac{c}{c_o}\right) = K_{app}t \qquad (1)$$

where C is the concentration of RhB at time t, C_o is the initial concentration, and K_{app} is the apparent reaction constant. As shown in **Table 5**, pure ZnO exhibits a K_{app} of 0.0089 min^{-1}, whereas the K_{app} for M-ZnO-MWCNT and I-ZnO-MWCNT is 0.1329 and 0.1452 min^{-1}, respectively. Their reaction constant is almost 16 times higher than that of pure ZnO.

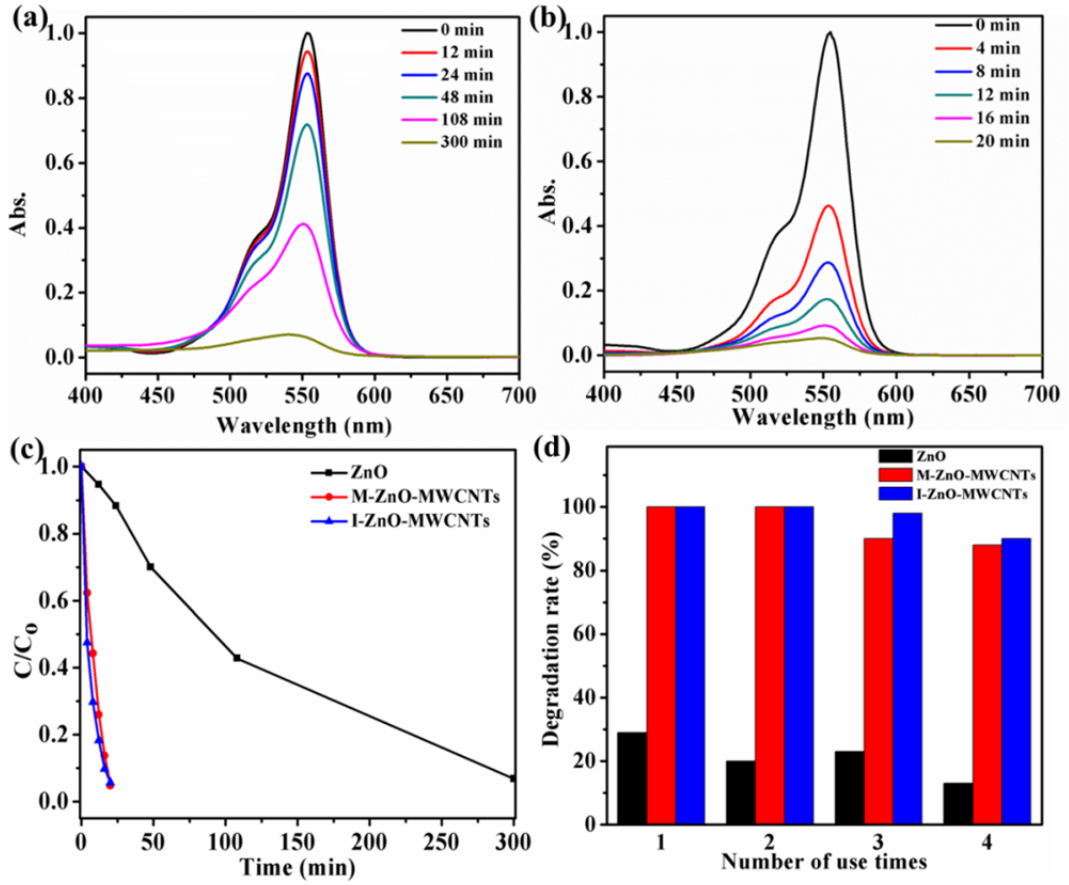

Figure 45. UV-Vis spectral changes of RhB (6×10^{-5} M) as a function of time in the presence of (a) ZnO and (b) I-ZnO-MWCNTs, (c) photodegradation of RhB under visible light in the presence of catalysts, and (d) degradation rate of RhB in the presence of catalysts as a function of use times.

Table 5. Summary of reaction rate, half-life time, surface area, and adsorption of RhB under dark condition for the photocatalysts ZnO, M-ZnO-MWCNTs and I-ZnO-MWCNTs.

Samples	K_{app} (min^{-1})	$t^{1/2}$ (min)	Adsorption of RhB (%)	BET (m^2/g)
ZnO	0.0089	77.0	5	9
M-ZnO-MWCNTs	0.1329	5.2	42	24
I-ZnO-MWCNTs	0.1452	4.7	50	26

The durability of ZnO-MWCNT hybrids for the degradation of RhB under visible light was also checked (**Figure 45**d). The photodegradation of RhB was monitored for four consecutive cycles, each for 20 min. After each cycle, the photocatalysts were washed thoroughly with water and added into fresh RhB solution for the next cycle of reaction. The experimental results indicate that the ZnO-MWCNT hybrids still retain 90% activity for degradation of RhB after 4 consecutive uses. Due to the low photocatalytic efficiency of ZnO, there is only 29% degradation of RhB during the first cycle. After 4 consecutive uses, ZnO only retains 13% activity for RhB degradation, which is more than a 50% decrease in efficiency. This indicates that the introduction of MWCNTs into ZnO not only increases the photocatalytic efficiency, but also prompts their stability during photocatalytic reaction. More importantly, it indicates that these highly active ZnO-MWCNT photocatalysts could be easily separated and recovered after usage, which would greatly promote their practical application for eliminating organic pollutants from environment.

6.3.5 Mechanism for the enhanced ZnO-MWCNT photocatalytic activity

To understand the role of MWCNTs in the photocatalytic activity of the hybrids, the dye adsorptivity, surface area, and charge carrier mobility are measured.[158, 159, 163, 165] The adsorption characteristics of RhB onto the surface of both ZnO and ZnO-MWCNT hybrids were investigated. After equilibrium in the dark condition for 20 min, only 5% of RhB was adsorbed on the ZnO nanoparticle surface, whereas ZnO-MWCNT hybrids exhibit more than 8 times higher dye adsorptivity (ca. 42% for M-ZnO-MWCNTs and 50% for I-ZnO-MWCNTs, **Table 5**). The BET surface areas of ZnO and ZnO-MWCNT hybrids were characterized by N_2 adsorption–desorption at 77 K to verify the adsorptivity differences. Pure ZnO has a BET surface area of 29 m^2/g. After the introduction of MWCNTs, the BET surface area increases to 124 and 126 m^2/g for M-ZnO-MWCNTs and I-ZnO-MWCNTs, respectively (**Table 5**). The introduction of MWCNTs not only retains the stability of the nanosized ZnO particles, but also provides a π-π platform for dye molecules.[140] The RhB molecule has an aromatic chromophore, which leads to a face-to-face adsorption on the MWCNT surface via a π-π interaction. Under irradiation, the dyes are excited and the photogenerated electrons could easily transfer to the MWCNT surface and then participate in the redox reaction with ZnO nanoparticles. Subsequently, the dye* decomposes into CO_2 and H_2O through a series of redox reactions. Therefore, the synergetic effect between adsorptivity and photoreactivity could be achieved in a single process and result in an appreciable improvement in photodegradation of RhB compared with pure ZnO.

Besides increasing the dye adsorptivity, MWCNT can also serve as an electron acceptor and conductor due to its high electrical conductivity. In this aspect, MWCNTs could suppress the charge recombination, enhance the charge separation efficiency, and prompt the photocatalytic activity. The electrochemical impedance spectroscopy (EIS) Nyquist plots of ZnO and ZnO-MWCNT electrodes were measured to verify the charge carrier mobility. With the introduction of MWCNTs, the semicircle size in the plot of ZnO-MWCNT hybrids becomes smaller than that of ZnO. The decreased semicircle size indicates an effective separation of photogenerated electron-hole pairs and fast interfacial charge transfer from the electron donor to electron acceptor.[166]

Based on the above experimental results, it can be concluded that the enhanced photocatalytic performance of ZnO-MWCNT hybrids comes from the high dye adsorptivity of MWCNTs and their excellent electron accepting and transferring abilities. On the basis of the above results, a reaction scheme was proposed to explain the enhancement of the photocatalytic properties of the ZnO-MWCNTs (**Figure 46**). Firstly, RhB molecules form a face-to-face adsorption onto the MWCNT surface via a π-π interaction; secondly, under visible light irradiation, the photogenerated electrons from dyes transfer from the surface of the MWCNTs to the nearest ZnO nanoparticles; subsequently, the injected electron reacts with the surface-adsorbed O_2 molecules to yield ROS; finally, the dye* degrades into mineralized products by these reactive species.

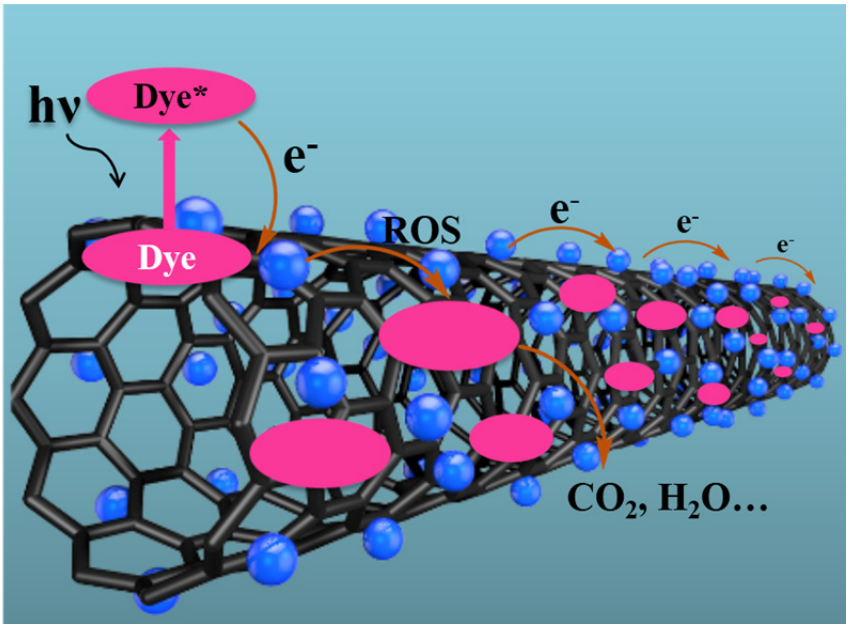

Figure 46. Proposed mechanism for the photocatalytic degradation of RhB by ZnO-GO under visible light irradiation.

6.4 Conclusions

In this work, simple and straightforward methods, mixing and *in situ* methods, have been developed to prepare ZnO-MWCNT hybrids with an average particle size of 4~5 nm. MWCNTs underwent a remarkable stabilizing transition in methanol upon coating with an adequate amount of ZnO nanoparticles. The dispersion mechanism involves the positively charged ZnO nanoparticles inducing sufficient electrostatic repulsion between the tubes to result in homogeneous ZnO-MWCNT dispersion in methanol. Like the traditional non-covalent functionalization approach, the present dispersion methods have the advantage of being nondestructive to the MWCNT structure while achieving stable dispersion. Meanwhile, these methods also open up a new avenue to disperse MWCNTs in methanol. The dispersion methods presented here broaden the traditional non-covalent functionalization approach of using organic small molecules or

polymers as surfactants by introducing an inorganic surfactant, i.e., ZnO nanoparticles, to achieve stable dispersion of MWCNTs. The resultant ZnO-MWCNT hybrids exhibit significant advancement over pure ZnO as photocatalysts in the degradation of RhB under visible light irradiation. Unlike in previous reports, ZnO-MWCNTs prepared by mixing and *in situ* methods show similar photocatalytic activities due to the effective hybridization effect between ZnO and MWCNTs. The apparent reaction constant of ZnO-MWCNT hybrids is approximately 15 times higher than that of pure ZnO, and their durability exhibit high efficiency even after 4 consecutive uses. The great dye adsorptivity, high surface area and excellent electron reception and conductor from MWCNTs induce the enhanced photocatalytic activity.

CHAPTER VII

HIGH-PERFORMANCE PHOTOCATALYST BASED ON NANOSIZED ZNO-GRAPHENE OXIDE HYBRID FOR REMOVAL OF ENVIRONMENTAL POLLUTANTS

7.1 Introduction

Photocatalytic degradation of organic pollutants by semiconducting metal oxides (especially TiO_2 and ZnO) has received increasing attention during the past decade as a promising technology for pollution abatement.[159, 167, 168] Both ultraviolet (UV) and visible light irradiation can activate photocatalysis.[155] The UV light irradiation mechanism involves the excitation of the semiconductor with a concomitant generation of a variety of reactive oxidation species (ROS, such as $\cdot O_2^-$, HOO· and ·OH). Subsequently, photo-oxidation of the organic pollutants by these species can take place, and the pollutants can be degraded into harmless mineralized products or water and CO_2. In the case of visible light, the mechanism involves the excitation of the pollutants instead of the semiconductor, followed by electron transfer from the excited pollutants to the conduction band of the semiconductors. The injected electron reacts with the surface-adsorbed O_2 molecules to yield ROS. Then, these reactive species degrade the organic pollutant into mineralized products. Photocatalytic degradation of the organic pollutant induced by visible light is more economic than that by UV light, because visible light makes up a larger portion of sunlight.[155] However, synthesis of highly active, effective visible light photocatalysts remains scarce.

An ideal visible light active photocatalyst needs high electron conduction from the organic pollutant to the semiconductor and a slow electron-hole pair recombination. Several attempts have been made to enhance the charge transportation and separation, including conjugation of the semiconductor with electron scavenging agents, like heterogeneous atoms/ions and electron-accepting materials.[140, 160, 169-171] For the latter, graphene has been recognized as one of the most promising materials for supporting photocatalytic semiconductors because of its unique electronic properties and large surface area.[159, 170] It has been demonstrated that graphene surfaces decorated with various kinds of nanoparticles, such as Au, Pt, and TiO_2, display high activity for catalytic applications.[51, 56, 158, 170] These advanced functions can be attributed to the huge surface area and the excellent electron conduction properties of graphene. Therefore, the combined usage of graphene and semiconductors offers promising potential for effective photodegradation of organic pollutants into environmentally benign species by visible light.

Among the various semiconductor photocatalysts, ZnO has attracted great attention because of its wide band gap (3.37 eV), high electron mobility, low cost, and environmental friendliness.[140] Recently, progress has been made to prepare ZnO-graphene hybrids. Li et al. reported a chemical deposition method to prepare ZnO-graphene hybrids, and the as-prepared ZnO nanoparticles have diameters ranging from 10–20 nm.[160] A hydrothermal approach was also reported to fabricate ZnO nanorod-graphene hybrids by Chen and his coworkers.[162] The length and diameter of blank ZnO nanorods are ca. 50–200 nm and 15–30 nm, respectively. Li et al. reported a facile

strategy to synthesize ZnO-graphene in water consisting of flower-like ZnO nanoparticles with diameters of about 1μm.[161] Although these ZnO-graphene hybrids have shown outstanding performance as photocatalysts, the particle sizes for ZnO in these reports are still too large. Further reduction in ZnO sizes is likely to improve the photocatalytic activity of the catalysts.[172]

There are two main attributes related to the quantized ZnO nanoparticles: quantum confinement effect and large surface-to-volume ratio.[173] For the quantum confinement effect, the band gap of a semiconductor increases and the band edges shift to yield larger redox potentials as the particle diameter falls below a critical radius of approximately 7 nm for ZnO.[173, 174] The increased driving force in size-quantized systems is expected to increase the rate constant of charge transfer.[175] Secondly, the large surface-to-volume ratio of quantized particles would provide a large overall contact surface area with graphene and lead to an efficient hybridization with graphene. Such a hybridization effect would retard the recombination of electron-hole pairs and inhibit photocorrosion of ZnO nanoparticles, which should lead to an enhanced photoactivity.[163] Therefore, it is important to reduce the ZnO particle sizes down below 7 nm to exert quantum confinement effect to achieve an optimal synergetic effect from both ZnO and graphene.

In this work, we report a facile sol-gel method to prepare well-dispersed and nanometer-sized ZnO nanoparticles with an average diameter of 4.5±0.5 nm on graphene oxide (GO) sheets. This sol-gel method provides an efficient and economic approach toward achieving sufficient interfacial contact between ZnO and GO. During the

reaction, GO serves as a 2D template for the anchoring, nucleation, and growth of soluble ZnO precursors into ZnO nanoparticles. The ZnO-GO hybrid shows superior performance for the photodegradation of Rhodamine B under visible light irradiation. Possible mechanisms for the observed enhancement in photocatalytic activity are discussed.

7.2 Materials and methods

7.2.1 Materials

Graphite (SP-1 graphite, average particle sizes of 45 μm) was obtained from Bay Carbon Inc, USA. Zinc acetate dihydrate, potassium hydroxide, rhodamine B, sulfuric acid, sodium nitrite, potassium permanganate, and methanol were purchased from Sigma-Aldrich and were used as received.

7.2.2 Synthesis of ZnO nanoparticles and ZnO-GO hybrids

ZnO nanoparticles were prepared by hydrolyzing zinc acetate dihydrate in methanol. This method has been previously reported.[145] KOH (1.0 g, 17.8 mM) was first dissolved in 200 mL methanol at 70 °C with refluxing and stirring to obtain a homogeneous solution. Subsequently, zinc acetate dihydrate (2.0 g, 8.9 mM) methanol solution (22 mL) was added directly into the basic methanol solution. This mixture was then kept at 70 °C with refluxing and stirring for 2 hours. The prepared ZnO nanoparticles were purified by the precipitation and dispersion procedure twice.

7.2.3 Synthesis of ZnO-GO hybrids

GO was prepared by the Hummers' method. Graphite powder (0.5 g) was firstly treated with a solution containing concentrated H_2SO_4 (50 mL) and $NaNO_3$ (0.5 g)

below 5 °C. $KMnO_4$ (3 g) was added gradually, and the mixture was stirred continuously for 2 h. The mixture was then kept at 35 ^oC for another 2 h. The mixture was diluted with deionized (DI) water (23 mL) and stirred for 15 min. Additional DI water (71 mL) and 30% H_2O_2 (10 mL) were added to the mixture, which changed the mixture color to brilliant yellow. Finally, the mixture was washed with water several times and HCl once to remove metallic ions.

The method to synthesize ZnO-GO hybrid is similar to that of ZnO nanoparticles. GO (80mg, 0.8 mg/mL) was mixed with a KOH (0.5 g, 8.9 mM) methanol solution and sonicated for 30 minutes to obtain a homogeneous solution, and then heated to 60 °C. After that, a zinc acetate dihydrate (1 g, 4.5 mM) methanol solution (11mL) was added, and the mixture was kept stirring for 2 hours at 60 °C. The ZnO-GO hybrids were filtered through a membrane with 0.5 μm pore size to remove ungrafted ZnO nanoparticles.

7.2.4 Characterization

Transmission electron microscopy (TEM) images were obtained from a JEOL 2010 high-resolution microscope operated at 200 kV. X-ray photoelectron spectroscopy (XPS) data was obtained with a Kratos Axis Ultra using a non-monochromatic MgK_α photon source (1486 eV) for measurements. X-ray diffraction (XRD) patterns of ZnO and ZnO-MWCNTs were acquired using a Bruker D8 Advanced Powder X-ray Diffractometer with CuK_α incident radiation (k = 1.5418 Å). Thermal gravimetric analysis (TGA) of ZnO-MWCNT hybrids was performed with ~8 mg of solid powder. The test was run from 30 °C to 900 °C with a ramp rate of 20 °C/min. in air. UV-Vis

absorption spectra were acquired with a UV-Vis-NIR spectrophotometer (Shimadzu, UV-3600). The Brunauer–Emmett–Teller (BET) surface area measurements were performed on a Beckman Coulter SA 3100 surface area and pore size analyzer at 77 °K with prior degassing under vacuum at 80 °C for 2h.

7.2.5 Photocatalytic activities of ZnO and ZnO-GO

The photodegradation of Rhodamine B (RhB) was carried out under visible light irradiation. In a typical process, catalyst (5 mg) was suspended in RhB aqueous solution (3×10^{-5} M, 3 mL). Then, the solution was exposed to the visible light irradiation produced by a 260 W Xe lamp positioned 20 cm away from the container. The degraded solution was analyzed by UV-Vis spectroscopy at prescribed time intervals. The long-term effectiveness of the catalyst was tested as follows: ZnO-GO (8 mg) was dispersed in RhB aqueous solution ($3x10^{-5}$ M, 5 mL), and the solution was exposed to the visible light irradiation for 20 min. The catalyst underwent four consecutive cycles and was centrifuged and washed thoroughly with water after each cycle.

7.2.6 Fabrication of the electrodes for electrochemical impedance spectra measurements

For the EIS measurement, the catalyst (5.0 mg) was dispersed in 1.0 mL methanol, and the solution was then dropped on the conducting ITO glass substrate (24 Ω/square). Impedance measurements (Solartron 1287) were carried out at room temperature. The catalyst-coated ITO served as the working electrode, with a platinum plate and saturated calomel electrodes (SCEs) as the counter and reference electrodes.

The supporting electrolyte was a 2.5 mM $K_3[Fe(CN)_6]/K_4[Fe(CN)_6]$ (1:1) mixture as redox probe in a 0.1 M KCl solution. The impedance spectra were recorded under an AC perturbation signal of 5 mV over the frequency range of 10^5–0.1 Hz.

7.3 Results and discussion

7.3.1 Characterization of ZnO-GO hybrids

The procedure for the synthesis of ZnO-GO in methanol[145] is illustrated in **Figure 47**. In a typical procedure, a specified amount of GO was directly mixed with zinc acetate dehydrate and potassium hydroxide in methanol, and the solution was kept at 70 °C for 2 hours with refluxing and stirring. During the reaction, the nucleation of ZnO on the GO surface is governed by the presence of oxygen functional groups on GO, which generate electrostatic attraction to zinc ions. Afterwards, the addition of hydroxide ions promotes the subsequent growth of ZnO on the GO surface.

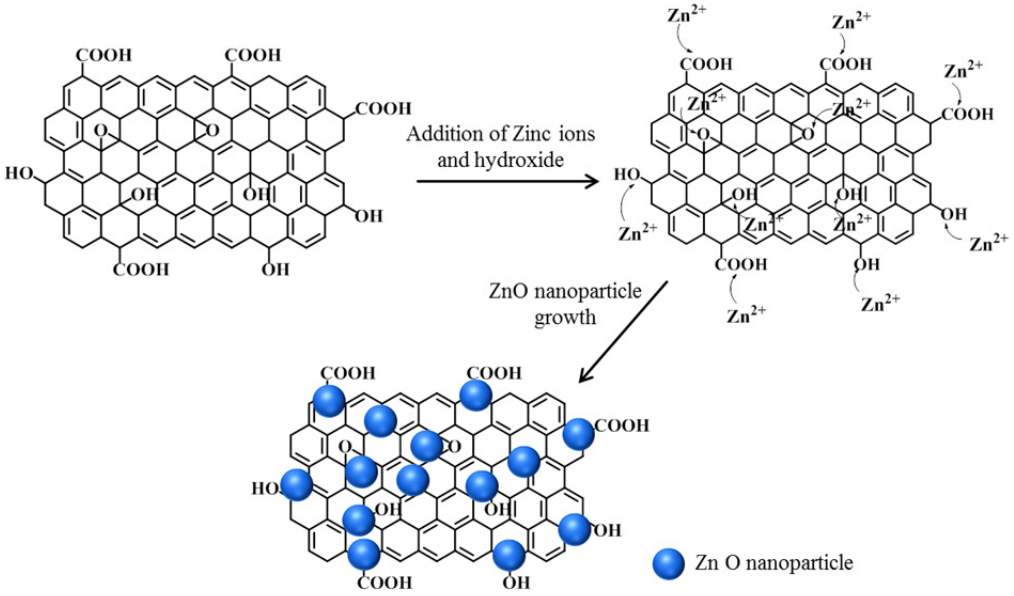

Figure 47. Illustration for preparation of ZnO-GO hybrid.

The morphologies of GO and the resultant ZnO-GO were characterized by TEM. As shown in **Figure 48**, a typical 2D GO sheet by itself shows a wrinkle structure. After the growth of ZnO nanoparticles on the GO surface, the GO does not change its morphology. The TEM images of the ZnO-GO hybrid (**Figure 48**b and c) clearly indicate that spherical ZnO nanoparticles are anchored and well distributed on the GO surface. From a statistical analysis of particle size based on 100 nanoparticles, the ZnO nanoparticles have an average particle size of 4.5 ± 0.5 nm (**Figure 48**d).

The chemical species of the ZnO-GO was studied by XPS. As shown in **Figure 49**a, the Zn peaks are dominant. However, C and O peaks also appear. The peaks located at 284 and 531 eV are attributed to C 1s and O 1s. The remaining peaks at higher binding energies (1045 and 1022 eV) are assigned to Zn 2p1/2 and 2p3/2, respectively.[160] The XRD patterns of GO, ZnO, and ZnO-GO are shown in **Figure 49**b. ZnO and ZnO-GO both present diffraction peaks at 2θ = 31.7°, 34.3°, 36.1°, 47.4°, 56.4°, 62.91°, and 67.9°, corresponding to the wurtzite ZnO structure of (100), (002), (101), (102), (110), (103) and (112) reflections, respectively.[145] GO displays a sharp peak at 2θ = 10.2°, with a d-spacing of 0.87 nm. The crystalline peak of graphite appears at 26.2°, which is the characteristic peak of hexagonal graphite with a d-spacing of around 0.34 nm.[162] The expansion in the interlayer spacing of GO is an indication of the absorbed water and oxygen functionalities among the GO interlayers. However, no characteristic peak is observed on the XRD pattern of ZnO-GO in the corresponding regions. This may be due to low graphene content or the presence of anchored ZnO nanoparticles, which disrupted the GO sheets from forming stacks.

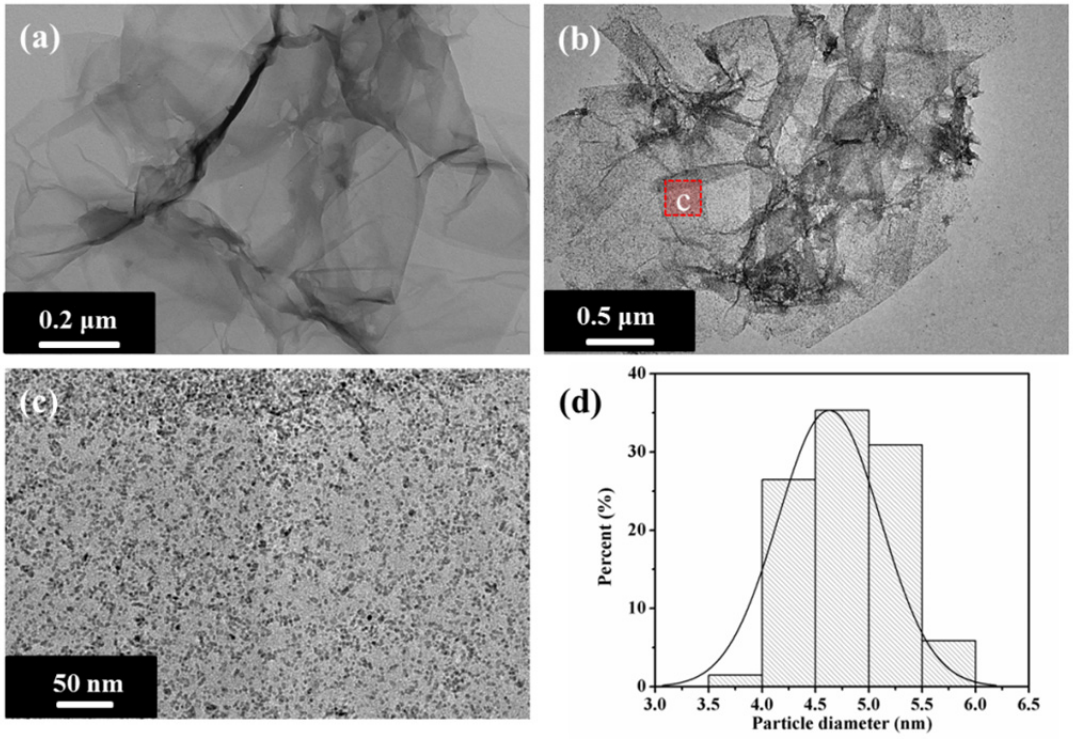

Figure 48. TEM images of (a) GO, (b) and (c) ZnO-GO in low and high magnification, and (d) ZnO size distribution in ZnO-GO. ((c) is the high magnification image of the square in (b)).

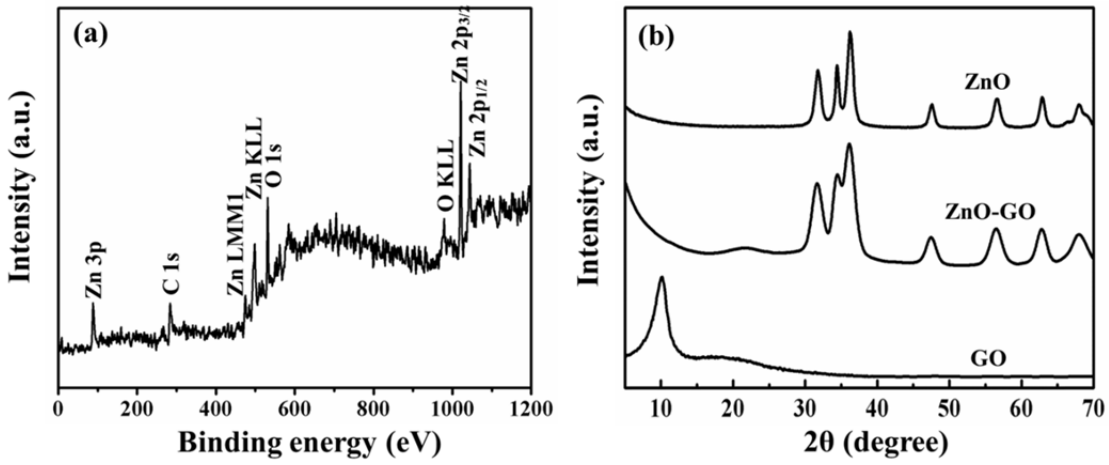

Figure 49. (a) XPS survey spectrum of ZnO-GO, and (b) XRD patterns of ZnO, ZnO-GO and GO.

The chemical content of the ZnO-GO is calculated from the TGA results (**Figure 50**). Two thermal degradation processes are shown in the TGA curve of ZnO. The degradation that happened at a temperature below 100 ^{o}C corresponds to the absorbed methanol in ZnO. Another weight loss (~5 wt.%) was observed in the temperature range of 250-350 ^{o}C. This loss is due to acetate ligands bound to the surface defects of the nanoparticle.[145] The TGA spectrum of ZnO-GO shows multiple weight losses in the temperature range of 30 to 400 ^{o}C. The weight loss from 30 to 150 ^{o}C is due to the absorbed water among the GO interlayers. It is well known that the oxygen groups on the GO surface could form hydrogen bonding with water and can easily trap water at the interlayers.[176] The decomposition of the oxygen groups on GO occurs at 150-250 ^{o}C. The decomposition of acetate ligands from ZnO nanoparticle also appears in the TGA curve of ZnO-GO at the same temperature range. The weight loss above 350 ^{o}C is attributed to the carbon decomposition of graphene. Based on the above finding, the content of GO in ZnO-GO could be calculated from these TGA curves to be roughly 10 wt.%.

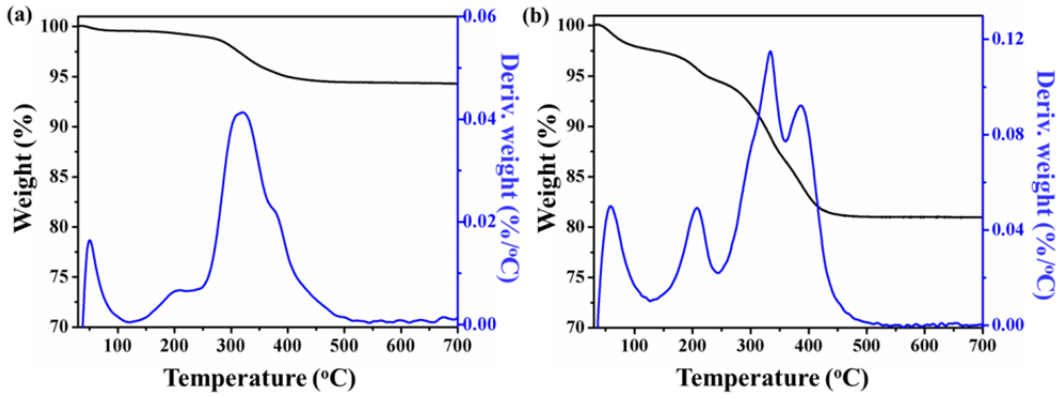

Figure 50. TGA curves and the corresponding derivatives of (a) ZnO and (b) ZnO-GO.

7.3.2 Photocatalytic characterization of ZnO-GO

The photocatalytic activities of ZnO and ZnO-GO were determined by photodegradation of rhodamine B (RhB) as a model reaction under visible light. The temporal evolution of the spectral changes during the photosensitized degradation of RhB in the presence of ZnO and ZnO-GO is shown in **Figure 51**. In general, in the presence of ZnO and ZnO-GO catalysts, visible light irradiation of the aqueous RhB solution leads to a decrease in its UV-Vis absorption with time. However, these two catalysts give different photodegradation efficiencies. ZnO shows a rather poor photocatalytic activity. Only 28% of RhB was decomposed in 16 min, and it took 100 min for the total degradation of RhB. In contrast, ZnO-GO photocatalyst exhibits remarkable improvements in the photodegradation of RhB, with 100% of the dye molecules degraded in 16 min. Note that there is no obvious peak wavelength shift for both ZnO and ZnO-GO systems with increasing time. This indicates that the photodegradation of RhB is dominated by the degradation of the aromatic chromophore but not the de-ethylation of RhB.[155, 158] As mentioned above, the dye is excited under visible light irradiation, and the generated electrons through this process would react with the surface-adsorbed O_2 molecules on the semiconductor to yield reactive oxidation species. Subsequently, the chromophoric structure of RhB was attacked by these oxidation species and degraded into water, CO_2 and other mineralized products.

The normalized temporal concentration changes (C/C_0) of RhB during the photodegradation were derived from its normalized absorbance (A/A_0) (at 550 nm) at a given time interval. It is clear from **Figure 51**c that the ZnO-GO shows significantly

higher photocatalytic activity than ZnO alone. The apparent reaction constants of ZnO and ZnO-GO were calculated through pseudo first-order kinetics:[164]

$$\ln\left(\frac{c}{c_o}\right) = K_{app}t \qquad (2)$$

where C is the concentration of RhB at time t, C_o is the initial concentration, and K_{app} is the apparent reaction constant. As shown in **Table 6**, pure ZnO nanoparticles exhibit a K_{app} of 0.026 min^{-1}, whereas the K_{app} of ZnO-GO reaches into 0.202 min^{-1}, which is almost 8 times higher than that of pure ZnO.

The long-term effectiveness of ZnO-GO for the degradation of RhB under visible light was also investigated (**Figure 51**d). The photodegradation of RhB was monitored for four consecutive cycles, each for 20 min. After each cycle, the photocatalysts were recovered through centrifugal separation, washed thoroughly with water and added into fresh RhB solution for the next cycle of reaction. The experimental results indicate that the ZnO-GO still retains 70% activity for degradation of RhB after 4 consecutive uses. Due to the low photocatalytic efficiency of ZnO, there is only 29% degradation of RhB during the first cycle. After 4 consecutive uses, ZnO only retains 13% activity. This indicates that the incorporation of GO in the catalyst not only increases the photocatalytic efficiency but also improves their stability during the photocatalytic reaction. Most importantly, it indicates that these highly active ZnO-GO photocatalysts can be easily separated and recovered by sedimentation, making them attractive in the practical application of removing organic pollutants from the environment.

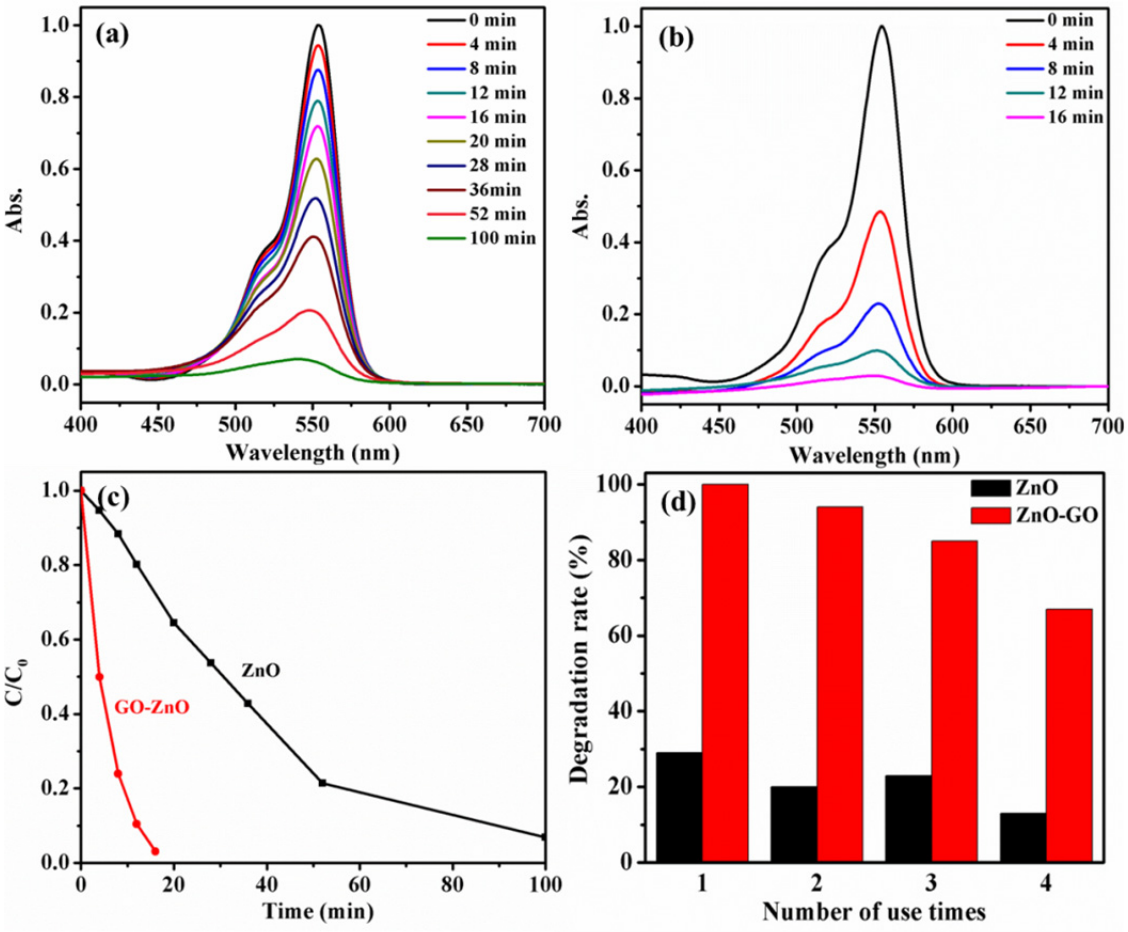

Figure 51. UV-Vis spectral changes of RhB (3×10^{-5} M) as a function of time in the presence of (a) ZnO and (b) ZnO-GO, (c) photodegradation of RhB under visible light, and (d) degradation rate of RhB in the presence of catalysts as a function of use times.

Table 6. Summary of reaction rate, half-life time, surface area, and adsorption of RhB under dark condition of the photocatalysts ZnO and ZnO-GO for comparison.

Samples	K_{app} (min^{-1})	$t_{1/2}$ (min)	Surface area (m^2/g)	Adsorption of dye (%)
ZnO	0.026	25	29	5
ZnO-GO	0.202	3	181	31

7.3.3 Mechanism for enhanced ZnO-GO photocatalytic activity

The photocatalytic activity of the ZnO-GO hybrids is intrinsically governed by the ZnO particle size, the adsorption of dyes, and charge carrier mobility.[158, 159, 163, 165] From the TEM results, ZnO nanoparticles on the GO surface have an average particle size of 4.5 ± 0.5 nm, which is smaller than the particle size in most reports.[160-162] Increased photocatalytic efficiency for ZnO is expected. Owing to the quantum confinement effect, the band gap of ZnO increases and the band edges shift to yield larger redox potentials.[175] The increased redox potential in size-quantized systems is expected to increase the rate constant of charge transfer. Furthermore, the large surface-to-volume ratio can provide ample contact surface area of ZnO with GO and lead to efficient hybridization. The hybridization effect can be verified by the high-resolution XPS spectra of Zn2p3/2 for ZnO and ZnO-GO (**Figure 52**a). The spectrum for the ZnO sample reveals that the core Zn 2p3/2 peak is positioned at 1020.4 eV with high symmetry, indicating that Zn was present only in the Zn^{2+} state.[151] However, the Zn 2p3/2 peak of ZnO-GO exhibits a shift to a higher binding energy by 2.4 eV. The shift to higher binding energy signifies an increased oxidation of Zn, resulting from its contact with the electronegative GO.[152] This indicates that the electronegative GO surfaces create a stronger dipole moment with ZnO nanoparticles. Such a hybridization effect can retard the recombination of electron-hole pairs and inhibit the photocorrosion of ZnO nanoparticles.[163] Therefore, the synergetic effect of quantum confinement and large surface-to-volume ratio from quantized ZnO particles contributes to the enhanced photodegredation of RhB.

Another factor for the enhanced photocatalytic activity of ZnO-GO is the enhanced adsorption of dyes by GO. The adsorption characteristics of RhB onto the surface of both ZnO and ZnO-GO were investigated. The concentrations of RhB after dark adsorption were obtained from UV-Vis absorption measurements. After equilibrium in the dark for 20 min, only 5% of RhB was adsorbed on the ZnO nanoparticle surface, whereas a large amount of dye molecules (ca. 31%) was adsorbed on the surface of the ZnO-GO (**Table 6**). To verify the adsorptivity differences, the BET surface areas of ZnO and ZnO-GO were characterized by N_2 adsorption–desorption at 77 K. After the introduction of GO, the BET surface area of ZnO-GO greatly increases from 29 m^2/g of pure ZnO to 181 m^2/g, which is six times higher than that of the pure ZnO (**Table 6**). From these experimental results, it can be deduced that the high adsorptivity of RhB on ZnO-GO originates from the 2D planar structure of GO. The introduction of GO not only retains the individual dispersion of the nanosized ZnO particles but also provides a π-π platform for adsorbing dye molecules.[140] The RhB molecule has an aromatic chromophore, which leads to a face-to-face adsorption on the GO surface via π-π interaction. Under light irradiation, the dyes are excited and the photogenerated electrons could easily transfer to the GO surface and then participate in the redox reaction with ZnO nanoparticles. Subsequently, the excited dyes decompose into CO_2 and H_2O through a series of redox reactions. Therefore, the synergetic effect between adsorptivity and photoreactivity is achieved in a simple process, resulting in an appreciable improvement in photodegradation of RhB compared with pure ZnO alone.

In addition to enhancing adsorptivity, GO also serves as an electron receptor and conductor due to its two-dimensional conjugation structure. In this aspect, GO helps suppress charge recombination, enhance charge separation efficiency, and improve the photocatalytic activity. The electrochemical impedance spectroscopy (EIS) Nyquist plots of ZnO and ZnO-GO electrodes were measured to verify the charge carrier mobility (**Figure 52**b). With the introduction of 10wt. % of GO, the semicircle size in the plot of ZnO-GO becomes much smaller than that of ZnO, almost one fourth of the size of ZnO plot. The decreased semicircle size indicates an effective separation of photogenerated electron-hole pairs and faster interfacial charge transfer from the electron donor to electron receptor.[166]

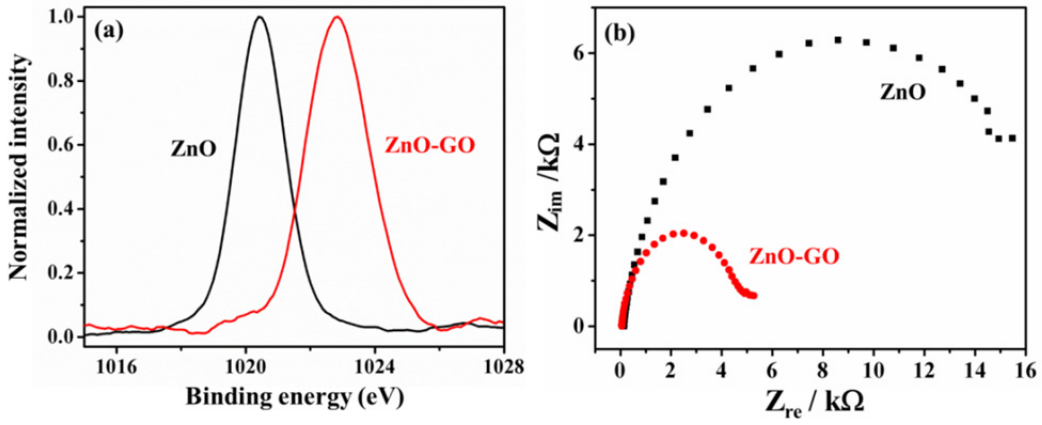

Figure 52. (a) XPS spectra of Zn 2p3/2 peak in ZnO and ZnO-GO, (b) EIS changes of ZnO and ZnO-GO electrodes.

From the above-mentioned experimental findings, it can be concluded that the significant enhancement in the photocatalytic activity of ZnO-GO comes from the following factors: nano-sized ZnO particles, high dye adsorptivity of GO, and excellent

electron conduction of GO. A schematic highlighting the mechanisms responsible for the observed enhancement in photocatalytic properties of the ZnO-GO is given in **Figure 53**. Firstly, RhB molecules form a face-to-face adsorption on the GO surface via π-π interaction. Then, under visible light irradiation, the photogenerated electrons from dyes move freely onto the surface of GO and transfer to the nearest ZnO nanoparticles. Subsequently, the injected electron reacts with the surface-adsorbed O_2 molecules to yield ROS. Finally, the dyes degrade into mineralized products by these reactive species. The hybridization of nano-sized ZnO with GO has been proven to be an effective and promising strategy to promote the photocatalytic performance of ZnO. This method opens up a new avenue to capture and convert solar energy to resolve the widespread environmental issue of organic pollutants.

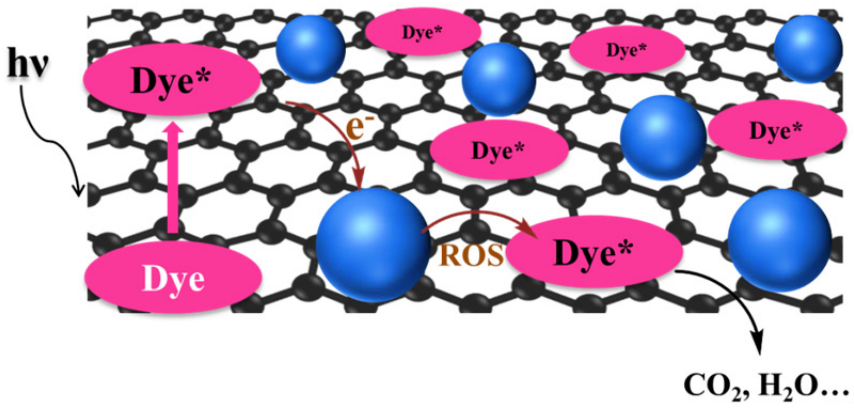

Figure 53. Proposed mechanism for the photocatalytic degradation of RhB by ZnO-GO under visible light irradiation. (Dye* means excited dye.)

7.4 Conclusions

ZnO-GO hybrid containing well-dispersed ZnO nanoparticles with an average diameter of 4.5±0.5 nm has been successfully prepared *via* a one-step sol-gel method.

The hybrid possesses nano-sized ZnO particles, great dye adsorptivity, and excellent electron accepting and transferring abilities from GO. On the basis of these advantages, the ZnO-GO hybrid exhibits significantly improved effectiveness over pure ZnO in the photodegradation of Rhodamine B under visible light irradiation. The enhanced photocatalytic performance of the ZnO-GO suggests that it may find potential applications in resolving environmental pollutant issues.

CHAPTER VIII

CONCLUSIONS AND FUTURE DIRECTIONS

8.1 Conclusions

Carbon nanotubes (CNTs) and graphene, as two dominant emerging carbon-based materials, have been regarded as important components for making various functional composite materials to advance nanotechnology. The attention on these materials originates from their excellent mechanical, thermal, and electrical properties. However, the lack of solubility and the difficult manipulation in solvents have significantly limited the use of these materials. To solve these problems, surface functionalization becomes crucial to increase the solubility, enable manipulation in solvents, and integrate these materials into nanodevices.

Conventional methods have faced challenges in controlling the functionalization of CNTs or graphene, which is critical to realize composites with tailored structures and unprecedented optical, electrical and catalytic properties. Further development in this field requires fundamental understanding of the steps involved in the surface functionalization, namely 1) reaction mechanism, and 2) controlled kinetics to yield tailored structures. The overall objective of my dissertation is to develop new approaches to functionalizing CNTs and graphene, study the functionalization mechanism and kinetics, and realize tailored structures and unprecedented properties in composites.

The surface functionalization of CNTs and graphene can be approached *via* two methods: (a) covalent attachment of chemical groups through reactions on the

conjugated skeleton of these materials, and (b) noncovalent functionalization of various functional molecules on the surface of these materials.

For the covalent method, I have designed new approaches that only involve the defect sites of CNTs or graphene to minimize the damage to their surface structure. MWCNTs could be functionalized by octadecylamine at various weight ratios, leading to new nanocomposites. These nanocomposites possess controllable surface wettability and high electrical conductivity. Graphene, without defect sites, is not favorable for further functionalization. In contrast, graphene oxide with various oxygen-containing groups, can offer an alternative. My results have shown that these oxygen-containing groups can be used to manipulate their reaction with silane coupling agents. These different functional groups enable controlling the grafting density of Au NPs and tailoring their catalytic applications. For the first time, the reaction mechanism between graphene oxide and silane agents is studied, and will expand the knowledge of the chemical nature of the graphene oxide. The novel approaches for covalent functionalization of CNTs and graphene on their defect sites will stand as a new alternative to manipulate their structure and properties without damage to their surface structure. The combination of GO and Au nanoparticle makes this hybrid material applicable for the applications to surface-enhanced Raman Scattering and catalytics.

For the noncovalent approach, the second component is physically absorbed on CNTs or graphene surface *via* van der Waals forces, π-π interactions, or electrostatic interaction. Due to the electronegative nature of CNTs and graphene oxide, ZnO nanoparticles with positive charges could be easily anchored on the surface of these two

materials. My research overcomes the traditional challenge to prepare well integrated ZnO-carbon composites at low temperature (<100 ^{o}C) with particle size lower than 10 nm. The creative combination of CNTs or graphene and the second component leads to broader catalytic application in the composites than the corresponding components, which makes them a new class of functional materials to advance nanotechnology.

8.2 Future directions

It has been demonstrated that the introduction of the CNT or GO has enabled the ZnO nanoparticle to become an efficient photocatalyst for the degradation of organic pollutants. Their capacities for dye adsorption and electron transport are the reasons for the enhanced performance. However, the amount of CNT or GO introduced into the final composites is very critical to the photocatalytic performance. It has been reported that the introduction of a high amount of CNT or GO will generate a shielding effect, which would minimize the active sites from the ZnO surface and also rapidly decrease the light penetrability through the reaction solution.[162] Therefore, it is very important to understand the critical concentration of CNT or GO introduced into the composites to benefit the potential photocatalytic application. Different amounts of MWCNTs could be added into ZnO nanoparticles through a mixing method to get the final ZnO-MWCNT hybrids with different ZnO and MWCNT weight ratios. Their photocatalytic behavior can be measured and compared through real-time detection of the photodegradation of the RhB.

Chemical exfoliation of graphite, as a wet chemistry method, is not only scalable to offer large-scale and direct exfoliation of graphene, but also versatile and easy to

obtain various derivatives of graphene.[19] This approach usually involves oxidation of graphite powder into GO in the presence of strong oxidants and acids. One drawback of GO is that the sp^2 bonding networks of graphene have been severely damaged during the oxidation process. After the oxidation process, GO has become electrically insulating, and its thermal and mechanical properties are also compromised. With these difficulties in mind, it is desirable to develop new methods to get exfoliated and dispersed unfunctionalized graphene. It has been reported that graphene could be exfoliated from graphite via sonication in the presence of stabilizer, such as sodium cholate,[177] pyrenesulfonic acid sodium salt,[178] perylenebisimide-based bolaamphiphile,[179] and so on. These stabilizers interact noncovalently with pristine graphene through π-π interaction and sterically or electrostatically prevent graphene sheets from restacking. However, to obtain dispersions with higher graphene concentrations, larger concentrations of stabilizers are required; this results in a low ratio of graphene to stabilizers. The excess stabilizer in the dispersion may hinder the use of the dispersion in composites, films, and electronic devices and adversely affect the enhancement in mechanical and electrical properties of the final products. To resolve these issues, new stabilizer, ZrP nanoplatelets, could be introduced. As reported in our group's previous work, ZrP can be used to exfoliate bundled SWCNTs into single tubes and disperse them into water. Similar mechanisms could also be applied to graphite.

REFERENCES

1. A. Krüger, *Carbon Materials and Nanotechnology*, Wiley-VCH:Weinheim, Germany,, 2010.
2. A. Thess, R. Lee, P. Nikolaev, H. J. Dai, P. Petit, J. Robert, C. H. Xu, Y. H. Lee, S. G. Kim, A. G. Rinzler, D. T. Colbert, G. E. Scuseria, D. Tomanek, J. E. Fischer and R. E. Smalley, *Science*, 1996, **273**, 483-487.
3. S. Stankovich, D. A. Dikin, G. H. B. Dommett, K. M. Kohlhaas, E. J. Zimney, E. A. Stach, R. D. Piner, S. T. Nguyen and R. S. Ruoff, *Nature*, 2006, **442**, 282-286.
4. M. F. Yu, O. Lourie, M. J. Dyer, K. Moloni, T. F. Kelly and R. S. Ruoff, *Science*, 2000, **287**, 637-640.
5. T. Ando, *Npg Asia Materials*, 2009, **1**, 17-21.
6. A. K. Geim and K. S. Novoselov, *Nature Materials*, 2007, **6**, 183-191.
7. K. S. Kim, Y. Zhao, H. Jang, S. Y. Lee, J. M. Kim, K. S. Kim, J.-H. Ahn, P. Kim, J.-Y. Choi and B. H. Hong, *Nature*, 2009, **457**, 706-710.
8. D. Tasis, N. Tagmatarchis, A. Bianco and M. Prato, *Chemical Reviews*, 2006, **106**, 1105-1136.
9. D. Li, M. B. Mueller, S. Gilje, R. B. Kaner and G. G. Wallace, *Nature Nanotechnology*, 2008, **3**, 101-105.
10. S. Iijima, *Nature*, 1991, **354**, 56-58.
11. J. Prasek, J. Drbohlavova, J. Chomoucka, J. Hubalek, O. Jasek, V. Adam and R. Kizek, *Journal of Materials Chemistry*, 2011, **21**, 15872-15884.

12. J. Zhu, M. Yudasaka, M. F. Zhang and S. Iijima, *Journal of Physical Chemistry B*, 2004, **108**, 11317-11320.

13. R. D. Saito, G.; Dresselhaus, and M. S., *Physical Properties of Carbon Nanotubes*, Imperial College Press: London, 1998.

14. K. Balasubramanian and M. Burghard, *Small*, 2005, **1**, 180-192.

15. C. Cha, S. R. Shin, N. Annabi, M. R. Dokmeci and A. Khademhosseini, *ACS Nano*, 2013, **7**, 2891-2897.

16. K. S. Novoselov, A. K. Geim, S. V. Morozov, D. Jiang, Y. Zhang, S. V. Dubonos, I. V. Grigorieva and A. A. Firsov, *Science*, 2004, **306**, 666-669.

17. J. Zhu, M. Chen, Q. He, L. Shao, S. Wei and Z. Guo, *RSC Advances*, 2013, **3**, 22790-22824.

18. H. Bai, C. Li and G. Q. Shi, *Advanced Materials*, 2011, **23**, 1089-1115.

19. S. Park and R. S. Ruoff, *Nature Nanotechnology*, 2009, **4**, 217-224.

20. D. R. Dreyer, S. Park, C. W. Bielawski and R. S. Ruoff, *Chemical Society Reviews*, 2010, **39**, 228-240.

21. W. S. Hummers and R. E. Offeman, *Journal of the American Chemical Society*, 1958, **80**, 1339-1339.

22. A. Lerf, H. Y. He, M. Forster and J. Klinowski, *Journal of Physical Chemistry B*, 1998, **102**, 4477-4482.

23. D. R. Dreyer, A. D. Todd and C. W. Bielawski, *Chemical Society Reviews*, 2014, **43**, 5288-5301.

24. A. Hirsch, *Angewandte Chemie-International Edition*, 2002, **41**, 1853-1859.

25. B. Gebhardt, Z. Syrgiannis, C. Backes, R. Graupner, F. Hauke and A. Hirsch, *Journal of the American Chemical Society*, 2011, **133**, 7985-7995.

26. C. A. Dyke and J. M. Tour, *Nano Letters*, 2003, **3**, 1215-1218.

27. J. R. Lomeda, C. D. Doyle, D. V. Kosynkin, W.-F. Hwang and J. M. Tour, *Journal of the American Chemical Society*, 2008, **130**, 16201-16206.

28. J. C. Charlier, *Accounts of Chemical Research*, 2002, **35**, 1063-1069.

29. E. V. Basiuk, M. Monroy-Pelaez, I. Puente-Lee and V. A. Basiuk, *Nano Letters*, 2004, **4**, 863-866.

30. H. Yao, C.-C. Chu, H.-J. Sue and R. Nishimura, *Carbon*, 2013, **53**, 366-373.

31. V. Ivanov, A. Fonseca, J. B. Nagy, A. Lucas, P. Lambin, D. Bernaerts and X. B. Zhang, *Carbon*, 1995, **33**, 1727-1738.

32. J. Liu, A. G. Rinzler, H. J. Dai, J. H. Hafner, R. K. Bradley, P. J. Boul, A. Lu, T. Iverson, K. Shelimov, C. B. Huffman, F. Rodriguez-Macias, Y. S. Shon, T. R. Lee, D. T. Colbert and R. E. Smalley, *Science*, 1998, **280**, 1253-1256.

33. J. Chen, M. A. Hamon, H. Hu, Y. S. Chen, A. M. Rao, P. C. Eklund and R. C. Haddon, *Science*, 1998, **282**, 95-98.

34. S. Stankovich, R. D. Piner, S. T. Nguyen and R. S. Ruoff, *Carbon*, 2006, **44**, 3342-3347.

35. M. J. O'Connell, S. M. Bachilo, C. B. Huffman, V. C. Moore, M. S. Strano, E. H. Haroz, K. L. Rialon, P. J. Boul, W. H. Noon, C. Kittrell, J. P. Ma, R. H. Hauge, R. B. Weisman and R. E. Smalley, *Science*, 2002, **297**, 593-596.

36. V. C. Moore, M. S. Strano, E. H. Haroz, R. H. Hauge, R. E. Smalley, J. Schmidt and Y. Talmon, *Nano Letters*, 2003, **3**, 1379-1382.

37. M. Shim, N. W. S. Kam, R. J. Chen, Y. M. Li and H. J. Dai, *Nano Letters*, 2002, **2**, 285-288.

38. H. J. Barraza, F. Pompeo, E. A. O'Rear and D. E. Resasco, *Nano Letters*, 2002, **2**, 797-802.

39. M. J. O'Connell, P. Boul, L. M. Ericson, C. Huffman, Y. H. Wang, E. Haroz, C. Kuper, J. Tour, K. D. Ausman and R. E. Smalley, *Chemical Physics Letters*, 2001, **342**, 265-271.

40. J. Liu, S. Fu, B. Yuan, Y. Li and Z. Deng, *Journal of the American Chemical Society*, 2010, **132**, 7279-7281.

41. R. Chen, S. R. Das, C. Jeong, M. R. Khan, D. B. Janes and M. A. Alam, *Advanced Functional Materials*, 2013, **23**, 5150-5158.

42. J. G. Ok, J. Y. Lee, H. W. Baac, S. H. Tawfick, L. J. Guo and A. J. Hart, *ACS Applied Materials & Interfaces*, 2014, **6**, 874-881.

43. S. Q. Ren, M. Bernardi, R. R. Lunt, V. Bulovic, J. C. Grossman and S. Gradecak, *Nano Letters*, 2011, **11**, 5316-5321.

44. Z. C. Wu, Z. H. Chen, X. Du, J. M. Logan, J. Sippel, M. Nikolou, K. Kamaras, J. R. Reynolds, D. B. Tanner, A. F. Hebard and A. G. Rinzler, *Science*, 2004, **305**, 1273-1276.

45. V. Georgakilas, D. Gournis, V. Tzitzios, L. Pasquato, D. M. Guldi and M. Prato, *Journal of Materials Chemistry*, 2007, **17**, 2679-2694.

46. G. G. Wildgoose, C. E. Banks and R. G. Compton, *Small*, 2006, **2**, 182-193.

47. H. Yao, T.-C. Huang and H.-J. Sue, *RSC Advances*, 2014, **4**, 61823-61830.

48. M. C. Daniel and D. Astruc, *Chemical Reviews*, 2004, **104**, 293-346.

49. R. A. Sperling, P. Rivera gil, F. Zhang, M. Zanella and W. J. Parak, *Chemical Society Reviews*, 2008, **37**, 1896-1908.

50. A. Corma and H. Garcia, *Chemical Society Reviews*, 2008, **37**, 2096-2126.

51. H. Yao, L. Jin, H.-J. Sue, Y. Sumi and R. Nishimura, *Journal of Materials Chemistry A*, 2013, **1**, 10783-10789.

52. B. Hvolbaek, T. V. W. Janssens, B. S. Clausen, H. Falsig, C. H. Christensen and J. K. Norskov, *Nano Today*, 2007, **2**, 14-18.

53. R. Long, K. Mao, X. Ye, W. Yan, Y. Huang, J. Wang, Y. Fu, X. Wang, X. Wu, Y. Xie and Y. Xiong, *Journal of the American Chemical Society*, 2013, **135**, 3200-3207.

54. J. Zhou, D. Bo, F. Zheng, S. Jibin, W. Chenxu, P. B. Messersmith and D. Hongwei, *Advanced Materials*, 2014, **26**, 701-705.

55. M. Zhou, A. Zhang, Z. Dai, Y. P. Feng and C. Zhang, *Journal of Physical Chemistry C*, 2010, **114**, 16541-16546.

56. H. Yin, H. Tang, D. Wang, Y. Gao and Z. Tang, *ACS Nano*, 2012, **6**, 8288-8297.

57. J. Wei, Y. Jia, Q. Shu, Z. Gu, K. Wang, D. Zhuang, G. Zhang, Z. Wang, J. Luo, A. Cao and D. Wu, *Nano Letters*, 2007, **7**, 2317-2321.

58. Y.-K. Kim and D.-H. Min, *Langmuir*, 2009, **25**, 11302-11306.

59. T. L. Sun, H. A. Liu, W. L. Song, X. Wang, L. Jiang, L. Li and D. B. Zhu, *Angewandte Chemie-International Edition*, 2004, **43**, 4663-4666.

60. K. K. S. Lau, J. Bico, K. B. K. Teo, M. Chhowalla, G. A. J. Amaratunga, W. I. Milne, G. H. McKinley and K. K. Gleason, *Nano Letters*, 2003, **3**, 1701-1705.

61. H. J. Li, X. B. Wang, Y. L. Song, Y. Q. Liu, Q. S. Li, L. Jiang and D. B. Zhu, *Angewandte Chemie-International Edition*, 2001, **40**, 1743-1746.

62. C. Luo, X. Zuo, L. Wang, E. Wang, S. Song, J. Wang, J. Wang, C. Fan and Y. Cao, *Nano Letters*, 2008, **8**, 4454-4458.

63. L.-Y. Meng and S.-J. Park, *Journal of Colloid and Interface Science*, 2010, **342**, 559-563.

64. J. Yang, Z. Zhang, X. Men, X. Xu and X. Zhu, *Journal of Colloid and Interface Science*, 2010, **346**, 241-247.

65. D. Xu, H. Liu, L. Yang and Z. Wang, *Carbon*, 2006, **44**, 3226-3231.

66. C.-F. Wang, W.-Y. Chen, H.-Z. Cheng and S.-L. Fu, *Journal of Physical Chemistry C*, 2010, **114**, 15607-15611.

67. A. Hirsch, Q. Y. Li and F. Wudl, *Angewandte Chemie-International Edition*, 1991, **30**, 1309-1310.

68. E. V. Basiuk, O. Ochoa-Olmos, F. F. Contreras-Torres, V. Meza-Laguna, E. Alvarez-Zauco, I. Puente-Lee and V. A. Basiuk, *Journal of Nanoscience and Nanotechnology*, 2011, **11**, 5546-5554.

69. Z. Lin, Y. Liu and C.-P. Wong, *Langmuir*, 2010, **26**, 16110-16114.

70. J. L. Stevens, A. Y. Huang, H. Q. Peng, L. W. Chiang, V. N. Khabashesku and J. L. Margrave, *Nano Letters*, 2003, **3**, 331-336.

71. F. Y. Xie, W. G. Xie, L. Gong, W. H. Zhang, S. H. Chen, Q. Z. Zhang and J. Chen, *Surface and Interface Analysis*, 2010, **42**, 1514-1518.

72. E. Bekyarova, M. E. Itkis, P. Ramesh, C. Berger, M. Sprinkle, W. A. de Heer and R. C. Haddon, *Journal of the American Chemical Society*, 2009, **131**, 1336-1337.

73. J. T. Han, S. Y. Kim, J. S. Woo and G.-W. Lee, *Advanced Materials*, 2008, **20**, 3724-3727.

74. R. N. Wenzel, *Industrial and Engineering Chemistry*, 1936, **28**, 988-994.

75. A. B. D. Cassie and S. Baxter, *Transactions of the Faraday Society*, 1944, **40**, 0546-0550.

76. S. Wang and L. Jiang, *Advanced Materials*, 2007, **19**, 3423-3424.

77. T. W. Ebbesen, H. J. Lezec, H. Hiura, J. W. Bennett, H. F. Ghaemi and T. Thio, *Nature*, 1996, **382**, 54-56.

78. D. Wang, P. Song, C. Liu, W. Wu and S. Fan, *Nanotechnology*, 2008, **19**, 075609 075601-075606

79. B. J. Hinds, N. Chopra, T. Rantell, R. Andrews, V. Gavalas and L. G. Bachas, *Science*, 2004, **303**, 62-65.

80. M. S. Fuhrer, J. Nygard, L. Shih, M. Forero, Y. G. Yoon, M. S. C. Mazzoni, H. J. Choi, J. Ihm, S. G. Louie, A. Zettl and P. L. McEuen, *Science*, 2000, **288**, 494-497.

81. P. J. Boul, J. Liu, E. T. Mickelson, C. B. Huffman, L. M. Ericson, I. W. Chiang, K. A. Smith, D. T. Colbert, R. H. Hauge, J. L. Margrave and R. E. Smalley, *Chemical Physics Letters*, 1999, **310**, 367-372.

82. G. Girishkumar, K. Vinodgopal and P. V. Kamat, *Journal of Physical Chemistry B*, 2004, **108**, 19960-19966.

83. A. K. K. Kyaw, H. Tantang, T. Wu, L. Ke, C. Peh, Z. H. Huang, X. T. Zeng, H. V. Demir, Q. Zhang and X. W. Sun, *Applied Physics Letters*, 2011, **99**, 021901 021901-021903.

84. M. Fleischmann, P. J. Hendra and A. J. McQuillan, *Chemical Physics Letters*, 1974, **26**, 163-166.

85. M. G. Albrecht and J. A. Creighton, *Journal of the American Chemical Society*, 1977, **99**, 5215-5217.

86. D. L. Jeanmaire and R. P. Vanduyne, *Journal of Electroanalytical Chemistry*, 1977, **84**, 1-20.

87. R. G. Freeman, K. C. Grabar, K. J. Allison, R. M. Bright, J. A. Davis, A. P. Guthrie, M. B. Hommer, M. A. Jackson, P. C. Smith, D. G. Walter and M. J. Natan, *Science*, 1995, **267**, 1629-1632.

88. W. G. Xu, X. Ling, J. Q. Xiao, M. S. Dresselhaus, J. Kong, H. X. Xu, Z. F. Liu and J. Zhang, *Proceedings of the National Academy of Sciences of the United States of America*, 2012, **109**, 9281-9286.

89. D. K. Lim, K. S. Jeon, H. M. Kim, J. M. Nam and Y. D. Suh, *Nature Materials*, 2010, **9**, 60-67.

90. K. C. Grabar, R. G. Freeman, M. B. Hommer and M. J. Natan, *Analytical Chemistry*, 1995, **67**, 735-743.

91. W. G. Xu, N. N. Mao and J. Zhang, *Small*, 2013, **9**, 1206-1224.

92. G. Goncalves, P. Marques, C. M. Granadeiro, H. I. S. Nogueira, M. K. Singh and J. Gracio, *Chemistry of Materials*, 2009, **21**, 4796-4802.

93. J. M. Zhu, Y. H. Shen, A. J. Xie, L. G. Qiu, Q. Zhang and S. Y. Zhang, *Journal of Physical Chemistry C*, 2007, **111**, 7629-7633.

94. J. B. Liu, S. H. Fu, B. Yuan, Y. L. Li and Z. X. Deng, *Journal of the American Chemical Society*, 2010, **132**, 7279-7281.

95. J. Sagiv, *Journal of the American Chemical Society*, 1980, **102**, 92-98.

96. S. Stankovich, D. A. Dikin, R. D. Piner, K. A. Kohlhaas, A. Kleinhammes, Y. Jia, Y. Wu, S. T. Nguyen and R. S. Ruoff, *Carbon*, 2007, **45**, 1558-1565.

97. D. V. Leff, L. Brandt and J. R. Heath, *Langmuir*, 1996, **12**, 4723-4730.

98. X. H. Ji, X. N. Song, J. Li, Y. B. Bai, W. S. Yang and X. G. Peng, *Journal of the American Chemical Society*, 2007, **129**, 13939-13948.

99. K. H. Liao, A. Mittal, S. Bose, C. Leighton, K. A. Mkhoyan and C. W. Macosko, *ACS Nano*, 2011, **5**, 1253-1258.

100. H. F. Yang, F. H. Li, C. S. Shan, D. X. Han, Q. X. Zhang, L. Niu and A. Ivaska, *Journal of Materials Chemistry*, 2009, **19**, 4632-4638.

101. A. R. Silva, V. Budarin, J. H. Clark, C. Freire and B. de Castro, *Carbon*, 2007, **45**, 1951-1964.

102. P. C. Ma, J. K. Kim and B. Z. Tang, *Carbon*, 2006, **44**, 3232-3238.

103. Y. Matsuo, Y. Nishino, T. Fukutsuka and Y. Sugie, *Carbon*, 2007, **45**, 1384-1390.

104. L. Hu, C.-A. Wang and Y. Huang, *Journal of the European Ceramic Society*, 2011, **31**, 2915-2922.

105. D. Li, M. B. Muller, S. Gilje, R. B. Kaner and G. G. Wallace, *Nature Nanotechnology*, 2008, **3**, 101-105.

106. E. Metwalli, D. Haines, O. Becker, S. Conzone and C. G. Pantano, *Journal of Colloid and Interface Science*, 2006, **298**, 825-831.

107. K. C. Grabar, P. C. Smith, M. D. Musick, J. A. Davis, D. G. Walter, M. A. Jackson, A. P. Guthrie and M. J. Natan, *Journal of the American Chemical Society*, 1996, **118**, 1148-1153.

108. T. Sainsbury, T. Ikuno, D. Okawa, D. Pacile, J. M. J. Frechet and A. Zettl, *Journal of Physical Chemistry C*, 2007, **111**, 12992-12999.

109. S. K. Ghosh and T. Pal, *Chemical Reviews*, 2007, **107**, 4797-4862.

110. K. L. Kelly, E. Coronado, L. L. Zhao and G. C. Schatz, *Journal of Physical Chemistry B*, 2003, **107**, 668-677.

111. Q. H. Wei, K. H. Su, S. Durant and X. Zhang, *Nano Letters*, 2004, **4**, 1067-1071.

112. K. H. Su, Q. H. Wei, X. Zhang, J. J. Mock, D. R. Smith and S. Schultz, *Nano Letters*, 2003, **3**, 1087-1090.

113. A. Otto, I. Mrozek, H. Grabhorn and W. Akemann, *Journal of Physics-Condensed Matter*, 1992, **4**, 1143-1212.

114. X. D. Jiang and A. Campion, *Chemical Physics Letters*, 1987, **140**, 95-100.

115. P. Hildebrandt and M. Stockburger, *Journal of Physical Chemistry*, 1984, **88**, 5935-5944.

116. T. Ji, L. Li, M. Wang, Z. Yang and X. Lu, *RSC Advances*, 2014, **4**, 29591-29594.

117. C. T. Campbell, J. C. Sharp, Y. X. Yao, E. M. Karp and T. L. Silbaugh, *Faraday Discussions*, 2011, **152**, 227-239.

118. M. Turner, V. B. Golovko, O. P. Vaughan, P. Abdulkin, A. Berenguer-Murcia, M. S. Tikhov, B. F. Johnson and R. M. Lambert, *Nature*, 2008, **454**, 981-983.

119. H. J. Yin, H. J. Tang, D. Wang, Y. Gao and Z. Y. Tang, *ACS Nano*, 2012, **6**, 8288-8297.

120. D. Astruc, F. Lu and J. R. Aranzaes, *Angewandte Chemie-International Edition*, 2005, **44**, 7852-7872.

121. J. Hu, Y. Dong, X. Chen, H. Zhang, J. Zheng, Q. Wang and X. Chen, *Chemical Engineering Journal*, 2014, **236**, 1-8.

122. E. Lam, S. Hrapovic, E. Majid, J. H. Chong and J. H. T. Luong, *Nanoscale*, 2012, **4**, 997-1002.

123. Y. Wang, G. Wei, W. Zhang, X. Jiang, P. Zheng, L. Shi and A. Dong, *Journal of Molecular Catalysis A: Chemical*, 2007, **266**, 233-238.

124. W. Hong, H. Bai, Y. Xu, Z. Yao, Z. Gu and G. Shi, *Journal of Physical Chemistry C*, 2010, **114**, 1822-1826.

125. D. R. Dreyer, A. D. Todd and C. W. Bielawski, *Chemical Society Reviews*, 2014, **43**, 5288-5301.

126. Y. Zhu, S. Murali, W. Cai, X. Li, J. W. Suk, J. R. Potts and R. S. Ruoff, *Advanced Materials*, 2010, **22**, 3906-3924.

127. K. Nguyen Tri, S. W. Kim, D.-H. Yoo, E. J. Kim and S. H. Hahn, *Applied Catalysis A-General*, 2014, **469**, 159-164.

128. J. Li, C.-Y. Liu and Y. Liu, *Journal of Materials Chemistry*, 2012, **22**, 8426-8430.

129. X. Xie, J. Long, J. Xu, L. Chen, Y. Wang, Z. Zhang and X. Wang, *RSC Advances*, 2012, **2**, 12438-12446.

130. W. Liu, D. Sun, J. Fu, R. Yuan and Z. Li, *RSC Advances*, 2014, **4**, 11003-11011.

131. M. Mahyari, A. Shaabani and Y. Bide, *RSC Advances*, 2013, **3**, 22509-22517.

132. R. Muszynski, B. Seger and P. V. Kamat, *Journal of Physical Chemistry C*, 2008, **112**, 5263-5266.

133. X. Ji, X. Song, J. Li, Y. Bai, W. Yang and X. Peng, *Journal of the American Chemical Society*, 2007, **129**, 13939-13948.

134. U. Kreibig and M. Vollme, *Optical Properties of Metal Clusters*, Berlin ; New York : Springer, 1995.

135. L. L. Zhao, K. L. Kelly and G. C. Schatz, *Journal of Physical Chemistry B*, 2003, **107**, 7343-7350.

136. Y. Choi, H. S. Bae, E. Seo, S. Jang, K. H. Park and B.-S. Kim, *Journal of Materials Chemistry*, 2011, **21**, 15431-15436.

137. T. Fujitani, I. Nakamura, T. Akita, M. Okumura and M. Haruta, *Angewandte Chemie-International Edition*, 2009, **48**, 9515-9518.

138. S. Hong and S. Myung, *Nature Nanotechnology*, 2007, **2**, 207-208.

139. I. Takesue, J. Haruyama, N. Kobayashi, S. Chiashi, S. Maruyama, T. Sugai and H. Shinohara, *Physical Review Letters*, 2006, **96**, 057001 057001-057004.

140. C. Han, M.-Q. Yang, B. Weng and Y.-J. Xu, *Physical Chemistry Chemical Physics*, 2014, **16**, 16891-16903.

141. J. Khanderi, R. C. Hoffmann, A. Gurlo and J. J. Schneider, *Journal of Materials Chemistry*, 2009, **19**, 5039-5046.

142. A. Chrissanthopoulos, S. Baskoutas, N. Bouropoulos, V. Dracopoulos, D. Tasis and S. N. Yannopoulos, *Thin Solid Films*, 2007, **515**, 8524-8528.

143. Y. Zhu, H. I. Elim, Y. L. Foo, T. Yu, Y. Liu, W. Ji, J. Lee, Z. Shen, A. T. S. Wee, J. T. L. Thong and C. H. Sow, *Advanced Materials*, 2006, **18**, 587-592.

144. J. Sun, L. Gao and M. Iwasa, *Chemical Communications*, 2004, **7**, 832-833.

145. D. Sun, M. Wong, L. Sun, Y. Li, N. Miyatake and H.-J. Sue, *Journal of Sol-Gel Science and Technology*, 2007, **43**, 237-243.

146. T. M. Riddick, *Control of Colloid Stability through Zeta Potential; with A Closing Chapter on Its Relationship to Cardiovascular Disease*, Livingston Publishing Company, Wynnewood, Pennsylvania, 1968.

147. V. Tohver, J. E. Smay, A. Braem, P. V. Braun and J. A. Lewis, *Proceedings of the National Academy of Sciences of the United States of America*, 2001, **98**, 8950-8954.

148. T. Cosgrove, *Colloid Science Principles, Methods and Applications*, Blackwell Publishing Ltd, 2005.

149. Z. Tan and D. H. C. Chua, *Journal of the Electrochemical Society*, 2011, **158**, K112-K116.

150. E. Murugan and G. Vimala, *Journal of Colloid and Interface Science*, 2013, **396**, 101-111.

151. J. Liu, X. Li and L. Dai, *Advanced Materials*, 2006, **18**, 1740-1744.

152. F.-L. Kuo, Y. Li, M. Solomon, J. Du and N. D. Shepherd, *Journal of Physics D-Applied Physics*, 2012, **45**, 065301 065301-065307.

153. M. J. Akhtar, M. Ahamed, S. Kumar, M. A. M. Khan, J. Ahmad and S. A. Alrokayan, *International Journal of Nanomedicine*, 2012, **7**, 845-857.

154. Y. Xie, S. H. Heo, S. H. Yoo, G. Ali and S. O. Cho, *Nanoscale Research Letters*, 2010, **5**, 603-607.

155. T. X. Wu, G. M. Liu, J. C. Zhao, H. Hidaka and N. Serpone, *Journal of Physical Chemistry B*, 1998, **102**, 5845-5851.

156. F. Vietmeyer, B. Seger and P. V. Kamat, *Advanced Materials*, 2007, **19**, 2935-2940.

157. T. A. Saleh, M. A. Gondal, Q. A. Drmosh, Z. H. Yamani and A. Al-yamani, *Chemical Engineering Journal*, 2011, **166**, 407-412.

158. E. Gao, W. Wang, M. Shang and J. Xu, *Physical Chemistry Chemical Physics*, 2011, **13**, 2887-2893.

159. H. Zhang, X. Lv, Y. Li, Y. Wang and J. Li, *ACS Nano*, 2010, **4**, 380-386.

160. B. Li and H. Cao, *Journal of Materials Chemistry*, 2011, **21**, 3346-3349.

161. B. Li, T. Liu, Y. Wang and Z. Wang, *Journal of Colloid and Interface Science*, 2012, **377**, 114-121.

162. Z. Chen, N. Zhang and Y.-J. Xu, *Crystengcomm*, 2013, **15**, 3022-3030.

163. Y. Zhang, Z. Chen, S. Liu and Y.-J. Xu, *Applied Catalysis B-Environmental*, 2013, **140**, 598-607.

164. J. Mu, C. Shao, Z. Guo, Z. Zhang, M. Zhang, P. Zhang, B. Chen and Y. Liu, *ACS Applied Materials & Interfaces*, 2011, **3**, 590-596.

165. Y. Zhang, N. Zhang, Z.-R. Tang and Y.-J. Xu, *ACS Nano*, 2012, **6**, 9777-9789.

166. L.-W. Zhang, H.-B. Fu and Y.-F. Zhu, *Advanced Functional Materials*, 2008, **18**, 2180-2189.

167. J. Du, X. Lai, N. Yang, J. Zhai, D. Kisailus, F. Su, D. Wang and L. Jiang, *ACS Nano*, 2011, **5**, 590-596.

168. X. Li, Q. Wang, Y. Zhao, W. Wu, J. Chen and H. Meng, *Journal of Colloid and Interface Science*, 2013, **411**, 69-75.

169. I. Bannat, K. Wessels, T. Oekermann, J. Rathousky, D. Bahnemann and M. Wark, *Chemistry of Materials*, 2009, **21**, 1645-1653.

170. Y. Liang, H. Wang, H. S. Casalongue, Z. Chen and H. Dai, *Nano Research*, 2010, **3**, 701-705.

171. J. C. Yu, G. S. Li, X. C. Wang, X. L. Hu, C. W. Leung and Z. D. Zhang, *Chemical Communications*, 2006, **25**, 2717-2719.

172. Q.-P. Luo, X.-Y. Yu, B.-X. Lei, H.-Y. Chen, D.-B. Kuang and C.-Y. Su, *Journal of Physical Chemistry C*, 2012, **116**, 8111-8117.

173. A. L. Schoenhalz, J. T. Arantes, A. Fazzio and G. M. Dalpian, *Journal of Physical Chemistry C*, 2010, **114**, 18293-18297.

174. D. Sun, H.-J. Sue and N. Miyatake, *Journal of Physical Chemistry C*, 2008, **112**, 16002-16010.

175. M. R. Hoffmann, S. T. Martin, W. Y. Choi and D. W. Bahnemann, *Chemical Reviews*, 1995, **95**, 69-96.

176. S. Some, Y. Kim, Y. Yoon, H. Yoo, S. Lee, Y. Park and H. Lee, *Scientific Reports*, 2013, **3**, 01929 01921-01925.

177. M. Lotya, P. J. King, U. Khan, S. De and J. N. Coleman, *ACS Nano*, 2010, **4**, 3155-3162.

178. D. Parviz, S. Das, H. S. T. Ahmed, F. Irin, S. Bhattacharia and M. J. Green, *ACS Nano*, 2012, **6**, 8857-8867.

179. J. M. Englert, J. Roehrl, C. D. Schmidt, R. Graupner, M. Hundhausen, F. Hauke and A. Hirsch, *Advanced Materials*, 2009, **21**, 4265-4269.